DESIGN OF SWIRL RECOVERY VANES FOR WING-MOUNTED TRACTOR PROPELLER PROPULSION SYSTEM

MSC THESIS

XINYUAN LIU

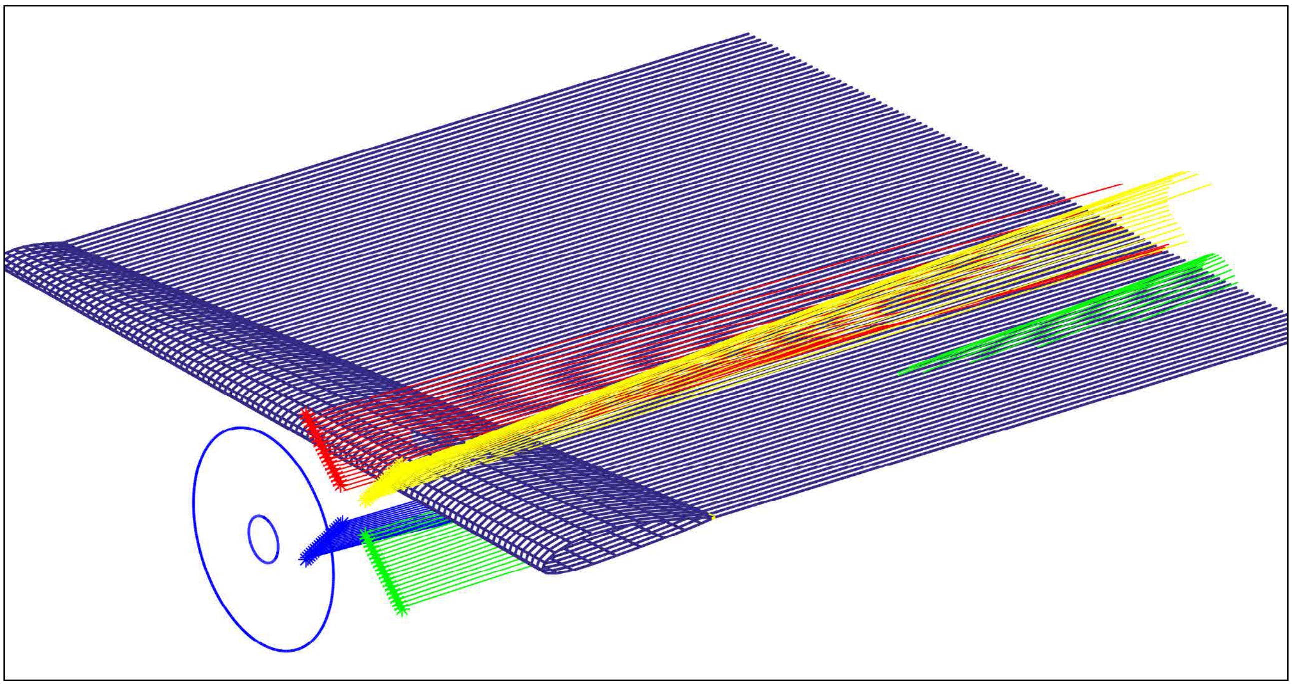

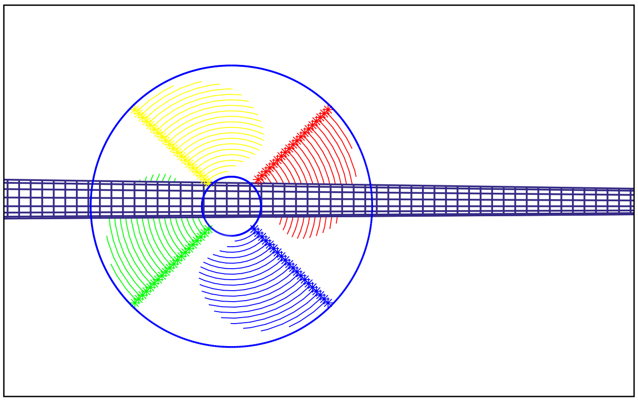

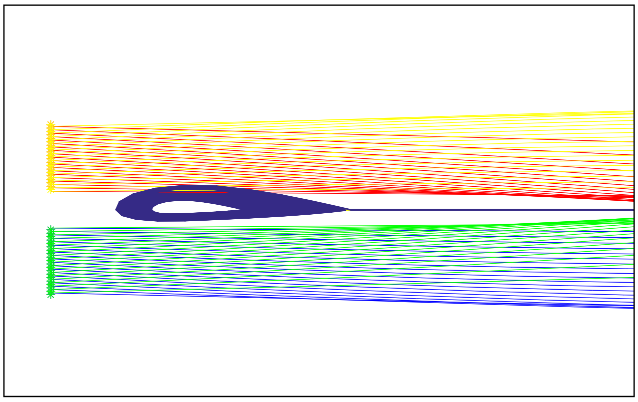

TU Delft
Delft
University of
Technology

Challenge the future

Faculty of Aerospace Engineering

Design of Swirl Recovery Vanes for Wing-Mounted Tractor Propeller Propulsion System

Thesis report

by

Xinyuan Liu

in partial fulfillment of the requirements for the degree of

Master of Science
in Aerospace Engineering

to be defended publicly on Friday June 22, 2018 at 9:30 AM.

Student number:	4472799	
Project duration:	March, 2017 – June, 2018	
Thesis committee:	ir. Q. (Qingxi) Li	TU Delft, Daily supervisor
	Prof.dr.ing. G. (Georg) Eitelberg	TU Delft, Supervisor
	Prof.dr.ir. L.L.M. (Leo) Veldhuis	TU Delft, Chair
	Dr. R.P. (Richard) Dwight	TU Delft

Delft University of Technology

ABSTRACT

Increasing pressure of reducing fuel consumption has led to renewed interests in propeller propulsion devices for their high propulsive efficiency. In a propeller propulsion system, the torque applied to the propeller results in angular momentum in propeller slipstream. This angular momentum is not only a form of energy loss that does not contribute to the propulsive performance, but also disturb the wing lift and drag distributions leading to deviated wing performance compared to a clean wing case. A series of design solutions have been introduced for dealing with this term, and current thesis mainly focus on the concept of Swirl Recovery Vane (SRV). SRVs are a set of stationary vanes mounted at downstream of the propeller, aiming at recovering the swirl in the propeller slipstream, which may produce extra thrust without extra power consuming. Previous research mainly focus on design of SRVs for an isolated propeller case. Considering a wing-mounted tractor propeller configuration, with benefit already gained in terms of wing induced drag reduction by wing swirl recovery, the swirl residual in propeller slipstream gives opportunities of introducing SRVs for extra thrust production, such that the system performance can be further improved. Due to the lack of such research, current project is about design of Swirl Recovery Vanes for a maximized system propulsive performance for Wing-Mounted Tractor Propeller Propulsion System at cruise condition. A wing design case is also performed for the same propeller slipstream without installed SRV, by comparison of performance gain of these two cases, the conclusion can be drawn that whether it's beneficial to introduce SRVs in a typical wing-mounted tractor propeller configuration.

A Surrogate-Based Multi-Fidelity optimization framework is developed for the design purpose. The strategy is to replace the direct optimization of expensive high-fidelity analysis by an iterative re-optimization of a corrected low-fidelity model. The low-fidelity method includes a slipstream model in which the velocities are obtained from RANS simulation of an isolated propeller, a lifting line based SRV design module and a surface singularity method based wing analysis and design module. The high-fidelity method is the Euler equation-based simulation. Furthermore, an alignment procedure between low- and high-fidelity results is established based on the shape-preserving response prediction(SPRP) algorithm, which assumes the variation of high-fidelity results can be predicted by the low-fidelity results.

Two main optimization tasks are performed to reach the final objective. The wing twist optimization for minimum induced drag under propeller slipstream indicates that the C_{Di} can reduced up to 5.93%. A series of one-blade SRV design cases are performed at different streamwise and azimuthal positions relative to wing. Results indicate that an upstream installed vane causes an un-expected induced drag increase of a downstream wing through its wake and tip vorticies development. This can be avoided when the vane is moved to downstream of wing. The optimum system performance is obtained when the vane is located at down-going blade side(DBS). By extra thrust produced by vane, a system induced drag reduction of 6.08% drag counts is achieved, which is almost equal to that obtained by wing twist design. Further conclusion is drawn that SRV should be installed as close to wing trailing edge as possible to obtain an maximized system performance in terms of system induced drag reduction.

CONTENTS

LIST OF FIGURES

LIST OF TABLES

NOMENCLATURE

ABBREVIATIONS

ADT	Actuator Disk Theory
BEM	Blade Element Method
CFD	Computational Fluid Dynamics
DBS	Down-going Blade Side
LL	Lifting Line method
PIV	Particle Image Velocimetry
SBO	Surrogate Based Optimization
$SPRP$	Shape-Preserving Response Prediction
SRV	Swirl Recovery Vane
SST	Shear Stress Transport
UBS	Up-going Blade Side

LATIN SYMBOLS

a	Doublet influence coefficients matrix
b	Source influence coefficients matrix
b	Wing span
c	Wing chord
C_D	Drag coefficient
C_{Di}	Induced drag coefficient
C_{di}	Induced drag coefficient distribution
$C_{Di,wing}$	Induced drag due to wing lift induced downwash
$C_{di,wing}$	Induced drag distribution due to wing lift induced downwash
$C_{Di,\Gamma}$	Induced drag due to wing circulation
$C_{di,\Gamma}$	Induced drag distribution due to wing circulation
$C_{Di,prop}$	Induced drag due to propeller induced swirl on wing
$C_{di,prop}$	Induced drag distribution due to propeller induced swirl on wing
$C_{Di,SRV}$	Induced drag due to SRV induced swirl on wing
$C_{di,SRV}$	Induced drag distribution due to SRV induced swirl on wing
$C_{Di,total}$	Total Induced drag
C_L	Lift coefficient
C_l	Lift coefficient distribution
$C_{L,SRV}$	SRV lift coefficient
$C_{L,wing}$	Wing lift coefficient
C_P	Propeller power coefficient
C_p	Pressure coefficient
C_Q	Propeller touque coefficient
C_{RHS}	Right hand side vector
C_T	Propeller thrust coefficient

$C_{T,SRV}$	SRV thrust coefficient
D	Propeller diameter
Di	Induced drag
$E_{viscous}$	Viscous loss in propeller slipstream
F_t	Stator section thrust
F_n	Stator section normal force
J	Propeller advance ratio
L	Lift
L/Di	Lift to Induced drag ratio
L/Di	Lift to Thrust ratio
m_{MTO}	Maximum take-off weight
$\dot{m}$	Mass flow rate
N	Vane number count
$\vec{N}$	Wing surface normal vector
n	Propeller rotational speed
$\vec{n}$	Panel normal vector
Obj	Design objective
P	Propeller power input
Q	Torque
q	Dynamic pressure
R	Propeller radius
S_w	Wing reference area
S_i	Local panel area
s_i	Normalized semi-width of vortex pair
T	Thrust
V_∞	Freestream velocity
V_1	Accelerated velocity in ADT
V_a	Axial velocity in slipstream
V_t	Tangential velocity in slipstream
V_r	Radial velocity in slipstream
V_{CR}	Aircraft cruise speed
$V_{wing,i}$	Wing self induced velocity
$V_{prop,i}$	Propeller induced velocity
$V_{SRV,i}$	SRV induced velocity
X	Design variable

GREEK SYMBOLS

α	Angle of attack
β_v	Helix pitch angle
β_i	Blade inflow angle
θ	Blade pitch angle
θ_s	Swirl angle
η_p	Propulsive efficiency
ρ	Density
Γ	Circulation(strength of vortex)
Γ_P	Circulation distribution obtained from Panel model
Γ_E	Circulation distribution obtained from Euler model

Γ_S	Circulation distribution obtained from Surrogate model
Ω	Angular speed
σ	Strength of source
μ	Strength of doublet
ϕ	Vane azimuthal position
ϕ	Perturbation potential

1

INTRODUCTION

1.1. BACKGROUND

Topics related to fuel efficient propulsion systems have always been attractive to researchers, especially when increasing pressure is recently formed to reduce the fuel consumption and emissions of civil transport aircraft. This has led to renewed interests in propeller propulsion devices due to their high propulsive efficiency.[3]. Research related to propellers have been driven by maximizing the propulsive efficiency. This can be achieved by reducing the loss terms in the propeller system. Among the primary loss terms, the swirl loss is the mainly focus of this study. In addition to the axial momentum change that imparted by the propeller to produce thrust, a part of the shaft power is going into the angular momentum of the fluid which doesn't result in any useful propulsive forces. However, this loss term can be reduced by introducing extra components in propeller slipstream to remove or recover the rotational motion. By doing this, extra performance gain can be potentially obtained for propeller propulsion system. In order to achieve this, a series of design solutions that varies in complexity have been introduced in previous studies, which will be discussed next

1.1.1. RESEARCH ON SWIRL RECOVERY

Several concepts have been introduced to recover swirl in the propeller slipstream. One option is the Contra-Rotating Open Rotor concept (CROR), as is depicted in Fig. 1.1. It employs two row of blades where the swirl induced by the first row of blade can be recovered by the second row of blades, thus the propulsive efficiency of the system can be improved compared to the single rotation propeller configuration[3]. In an experiment of full-scale aircraft equipped with CROR performed by Strack[15], an 8% of fuel saving and a 2.5% reduction of direct operating cost were estimated for the CROR engine compared to equivalent technology level turbofan engines. However, the drawbacks exhibited by this system is also apparent: it features high weight due to the complex gear system required for obtaining the contra rotation of two rotors. Additional interaction noise is generated by the contra-rotating stage and the structural layout is complicated which causes maintenance problem[16]. In this respect, a substitute design solution of less complexity would be more attractive to researchers and markets.

Figure 1.1: Concept counter-rotating turboprop engine on test stand. [1]

SWIRL RECOVERY BY VANES

Compared to CROR, a simpler design solution is to have a row of stator vanes instead of rotating blades behind the first rotor, as is depicted in Fig. 1.2. As is similar to the working principle of second rotor in CROR, the stators can also recover swirl and produce thrust. It was named Swirl Recovery Vane (SRV) by NASA in the late 1980s as a part of the Advanced Turboprop Project[1]. In this project, both experimental and numerical studies were performed on SRVs: an experiment on SRVs was performed by Gazzaniga [17], where results showed that the vanes contributed 2% of extra propulsive efficiency without consuming energy at the cruise condition of Mach 0.8. Compared to the experimental result, 5% was predicted from numerical analyses by use of Euler method carried out by Miller[18] and Yamamoto[19]. However, no subsequent research has been performed on SRVs until recently, an experimental study concerning the effects of SRVs on single-rotation propeller was performed by Sinnige et al.[3], PIV technique was utilized to show detailed features of the flow field induced by the propeller and SRV. This model is depicted in1.3. Conclusion was drawn that the upstream effect of SRVs on time-averaged propeller performance was negligible. A Computational Fluid Dynamics (CFD) based SRV design for an isolated propeller was performed by Wang [20]. This study obtained a thrust increase of 5.76% due to SRVs at design point (advance ratio J of 1). However, it's less efficient to use CFD for optimization purposes due to its high computational cost. Recently, a numerical and experimental study was performed by Li[6] where a lifting line based tool was utilized to perform SRV design for an isolated propeller, results indicated that SRVs can produce 3.4% of propeller thrust at high thrust condition (advance ratio J of 0.6), while 2.6% was measured in the experiment. A similar numerical study was carried out by Stokkermans et al.[5], of which the results showed the propeller propulsive efficiency increased by 0.50% at the cruise condition, while gains in the high-thrust condition was considerably larger (3.49%). It can be concluded that, according to numerical results of a propeller-SRV configuration, the efficiency gain due to SRV is around 3%-5% at high thrust condition, whereas a lower value of 0.5%-3% can be obtained at cruise condition, whereas the experimental results show lower values correspondingly.

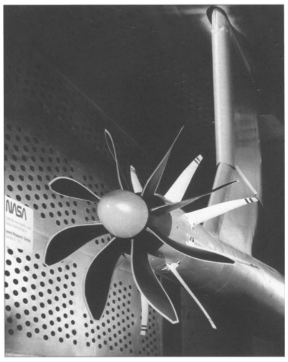

Figure 1.2: Integrated propeller (black) and swirl recovery vanes (white) model used in a wind tunnel test at NASA Lewis Research Center[2]

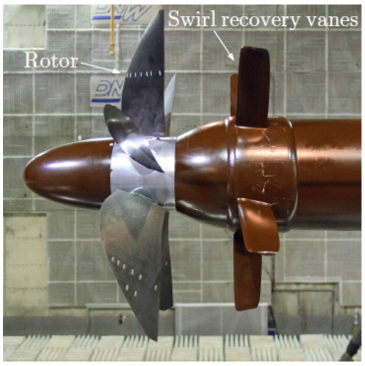

Figure 1.3: APIAN propeller model with downstream mounted swirl recovery vanes.[3]

SWIRL RECOVERY BY WING

Previous studies [4, 7, 21] have found that for a wing-mounted tractor propeller configuration, the downstream wing can also work as a swirl recovery vane. As is different from a typical SRV where an extra thrust is generated, the performance gain by a downstream integrated wing is a reduction of wing induced drag. From a system level, the reduction of drag is equivalent to an increase of thrust. In this respect both the wing and SRVs are investigated as an improvement of system thrust and propulsive efficiency. The first investigation on propeller wing aerodynamic interaction was performed by Witkowski[7] where experimental and computational results revealed that the effective propulsive efficiency of the system increased up to 3-5% from interference effects. Furthermore, as proved by many studies [4, 14, 22] that the wing design itself can be optimized to increase the performance gain. Typically the wing circulation distribution was optimized for minimum induced drag under the constraint of constant lift. In a preliminary study by Kroo [21], a well integrated wing is capable of restoring much of the loss associated with the slipstream swirl, and the overall propulsive efficiency increased up to 6%, which even exceeded that of the CROR. Another conclusion was drawn that the optimum circulation distribution for minimum induced drag is non-elliptical. Research performed by Veidhuis [4] showed that a wing with an inboard up rotating propeller experienced the lower induced drag compared to outboard rotating propeller. In the same study by Veidhuis [4], the F50 wing model was optimized for minimum drag, results showed the wing induced drag decreased by 4% at cruise condition. In the study performed by Epema et al[22], by optimization of the wing twist for minimum induced drag, the induced drag decreased by 7 drag counts, corresponding to 6.7% induced drag reduction. It can be concluded that propeller wing interaction effects can lead to induced drag reduction of up to 4%-7% at cruise condition.

OPPORTUNITY AND CHALLENGES OF SRV FOR WING-MOUNTED TRACTOR PROPELLER

Since both SRVs and Wing can recover swirl and improve the system propulsive efficiency, questions are raised that whether it's necessary to implement SRVs in a wing-mounted propeller configuration. It is noted that most of the SRV related works have been focused on the application of SRVs for isolated propeller, whereas first attempt to introduce SRVs in a wing-mounted tractor propeller configuration was performed by Stokkermans et al. [5]. In this study, SRVs designed for isolated propeller were simulated in a wing-mounted tractor propeller by use of RANS simulation. Results indicated that the SRVs designed for isolated propeller show little performance benefit when working at a wing-mounted tractor propeller case. In detail, the performance of a 5-blade SRV was degraded when installed at the wing upstream due to flow separation caused by wing induced upwash. By manually adjust the SRV pitch angle, potential benefit was already gained in terms of either improvement of wing performance or system propulsive efficiency. This indicated that careful optimization of SRVs taking the wing into account would most likely result in a maximized performance benefit.

Then second question is raised that whether wing needs to be re-optimized when SRV is installed. When

SRV is installed in between a propeller and a dowstream wing, it will tilt the swirl in propeller slipstream, as a result the wing inflow angle of attack will be locally changed. It is realized the a wing-upstream installed vane works in the same way as the wing twist variation since the change of twist is actually change of incidence angle. Moreover, the optimization of wing geometry always feature some drawbacks: First, optimization of wing chord distribution always leads to unrealistic local chord length, which can be either infinitely long or short. Also, the optimization of wing twist usually lead to highly twisted wing geometry in the slipstream region, causing difficulties for manufacturing. It is realized that, with only SRV design in a wing-mounted tractor propeller configuration, a series of benefit can potentially be gained: First, the vanes can produce extra thrust and second the vanes can potentially lead to wing performance improvement by tilting the inflow condition, and third, the wing geometry can be kept as non-changed which avoids the structural penalty due to the wing geometry variation.

1.2. RESEARCH OBJECTIVE

Though the swirl recovery from SRV and wing are investigated separately, there is still lack of research on SRV design for wing-mounted tractor propeller configuration, and no comparison is made of swirl recovery by SRV and wing. The research objective of current study is thus formated as follows:

- To investigate an optimum SRV design that provides a maximized system propulsive performance for a wing-mounted tractor propeller configuration in cruise condition.

Since no conclusion has been drawn on whether it's beneficial to introduce SRVs in a typical wing-mounted tractor propeller configuration, thereby an extra research objective will to be raised here, which is described in a series of research questions:

- What's the maximum system performance of a wing-mounted tractor propeller case if the wing is optimized with the presence of propeller slipstream?
- What's the maximum system performance of a Propeller-SRV-wing case if the wing geometry is fixed while only SRV is optimized?
- Whether it's beneficial to implement SRVs in a wing mounted propeller configuration?

In order to answer these questions, two main tasks are performed in this study:

- Perform wing optimization for minimum induced drag in a wing-mounted tractor propeller configuration.
- Perform SRVs design for maximized integrated propulsive performance of a wing-mounted tractor propeller configuration.

These two design cases are different in terms of optimization effort and performance gain: task 1 is performed to answer the first research question and task 2 aims at answering questions 2. By comparing the results of these two tasks the last question can be answered.

It is noted that design of any components in this system should aims at the performance of the entire system, including the performance of propeller, SRVs and wing. Since the integration of SRV before a wing will lead to performance deviation of both components, the analysis tool should be able to accurately predict wing ans SRV performance including their interference effects. Considering the absence of this tool, the development of following items is required:

- Simulation of isolated propeller to obtain slipstream data
- A SRV analysis and design module
- A Wing analysis and design module

1.3. OUTLINE

The outline of the project follows the steps to reach the final objective. Chapter 2 will discuss the aerodynamic interference encountered in this study, including the interference effects in a typical wing-mounted tractor propeller arrangements and how does the installed SRV affect such an interaction effects. Chapter 3 will present the methodologies to be applied in this study. First an introduction to implementation of low fidelity analysis module, including how to set up propeller slipstream, how to set up SRV and wing analysis module and how to adapt it for their interaction effects. Then the optimization algorithm and framework will be introduced. Chapter 4 and 5 will focus on the design tasks, while Chapter 4 will introduce the wing optimization case and Chapter 5 will focus on SRV design case. Finally, the conclusions and recommendations are stated in Chapter 6, and the research questions will be answered.

2

PROPELLER, SRV AND WING AERODYNAMICS

This chapter mainly focus on a qualitative characterization of the aerodynamic interaction effects contains in a wing mounted tractor propeller configuration without and with SRV installed case. As is already discussed, the aerodynamic interactions potentially lead to performance deviation of all the components, thereby it's necessary to understand the mechanism of how aerodynamic interaction affect the system performance.

First a study of isolated propeller is presented in Sec. 2.1, with focus on the characterization of propeller performance and its slipstream. Then the interaction effects in a propeller-SRV configuration is investigated in Sec. 2.2, including an introduction to the working principle of SRVs and the effects of SRVs on propeller slipstream development. Finally, Sec. 2.3 will investigate a propeller-SRV-wing arrangement, with focus on the interaction effects between SRV and wing.

2.1. ISOLATED PROPELLER AERODYNAMICS

This section introduces the basic theories about propellers. First the terminology describing propeller performance is presented, follow by an investigation to the relations between propulsive efficiency and swirl loss, the objective is to get an idea of the potential maximum performance gain by swirl recovery. Then the characterization of propeller slipstream will be discussed, with focus on the velocity distribution in the slipstream.

2.1.1. GENERAL TERMINOLOGY

The non-dimensional parameters describing propeller performance is presented in table 2.1. Non-dimensional parameters is typically used to describe complex systems as they can clearly demonstrate the dependency of various propeller parameters.

Advance ratio	$J = \frac{V_\infty}{n\ D}$
Thrust coefficient	$C_T = \frac{T}{\rho\ n^2\ D^4}$
Power coefficient	$C_P = \frac{P_t}{\rho\ n^3\ D^5}$
Propulsive efficiency	$\eta_p = \frac{C_T\ J}{C_P}$

Table 2.1: Propeller performance non-dimensional coefficients[14]

In this table, the advance ratio J represents the ratio between advancing speed of the propeller and tangential velocity at blade tip, which is often used to state the working condition of a propeller. Particularly, the propulsive efficiency is defined as the ratio between the propulsive power and shaft power. The shaft power is defined as $P = Q\,\Omega$, where Q is the propeller torque and Ω is the rotational speed. This is the power input to propeller. And the T multiplied by V_∞ is the propulsive power, which can be seen as the rate of useful power contributed by propeller.

2.1.2. PROPELLER EFFICIENCY AND SWIRL LOSS

This section will investigate the relation between propulsive efficiency and swirl loss. Different approaches have been developed to model isolated propeller aerodynamics and performance. The Actuator Disk Theory(ADT) is often used for preliminary analysis since it is the very basic theory that only considers axial momentum. As is stated in this method, the inflow velocity which is assumed as V_∞ is being accelerated when passing the propeller disk, reaching V_1 when being completely accelerated. The mass flow rate is constant in this process, which is defined as $\dot{m}$. Then the thrust generated by propeller can be calculated from equation:

$$T = \dot{m}(V_1 - V_\infty) \tag{2.1}$$

and the power input to the flow by propeller can be defined as:

$$P = \frac{1}{2}\dot{m}(V_1^2 - V_\infty^2) \tag{2.2}$$

The propulsive efficiency is thereby calculated as:

$$\eta_p = \frac{T\ V_\infty}{P} = \frac{\dot{m}(V_1 - V_\infty)}{\frac{1}{2}\dot{m}(V_1^2 - V_\infty^2)} = 1 + \frac{2}{\frac{V_1}{V_\infty}} \tag{2.3}$$

Compared to ADT model which only considers axial momentum, the Blade Element Method(BEM) model incorporates both axial and swirl velocities. The efficiency defined in BEM is depicted as:

$$\eta_p = \frac{T\ V_\infty}{P} = \frac{T\ V_\infty}{Q\omega} \tag{2.4}$$

where Q is the torque generated by propeller and ω is the propeller angular speed. Compared to classic ADT, the advantage of BEM lies in it's capability to give more accurate prediction of T and P. In this method, the calculated power input by the propeller P equals to the energy change of the flow when passing the propeller:

$$P = Q\omega = \frac{1}{2}\dot{m}(V_1^2 + V_t^2 - V_\infty^2) + E_{viscous} \tag{2.5}$$

where the $\frac{1}{2}\dot{m}V_t^2$ is the rotational kinetic energy that imparted by the propeller, which is actually the swirl loss. And the $E_{viscous}$ is actually the viscous loss in the flow due to propeller, which can also be modeled in the BEM method by use of 2D airfoil analysis as an option. It's realized that by comparing the propeller efficiency obtained from ADT and BEM, the swirl loss can be quantified in terms of propeller efficiency reduction.

A preliminary study performed by Veldhuis [23] applied the described methods, and the results is delivered in Table 2.2. Theη_{ADT} is obtained by the classic ADT model, calculated by Eq. 2.3. It's noted that two different BEM models are used, where the $BEM-original$ considers both swirl loss and viscous loss as already discussed and $BEM-noswirl$ only contains viscous loss and neglects swirl loss. Thereby the propulsive efficiency obtained from these two models can be described as:

$$\eta_{BEM-original} = \frac{T\,V_\infty}{\frac{1}{2}\dot{m}(V_1^2+V_t^2-V_\infty^2)+E_{viscous}} \tag{2.6}$$

$$\eta_{BEM-noswirl} = \frac{T\,V_\infty}{\frac{1}{2}\dot{m}(V_1^2-V_\infty^2)+E_{viscous}} \tag{2.7}$$

When looking the calculated η, it's observed the two BEM results are smaller than the ADT results, which is because the ADT model neglects all the loss term. Therefore, in order to quantify the swirl loss, it's more reasonable to compare results from two BEM models. Results indicate that, by neglecting the swirl loss, the propulsive efficiency increases by 3% for the low thrust case, which increases up to 9.6% for the high thrust condition. This is theoretically the maximum efficiency increase resulted from swirl recovery. This study gives a basic idea of how much efficiency gain can be potentially achieved by swirl recovery design.

C_T	0.300	0.560
η_{ADT}	0.859	0.782
$\eta_{BEM-original}$	0.742	0.658
$\eta_{BEM-noswirl}$	0.809	0.721

Table 2.2: The propulsive efficiency calculated from different numerical model at different thrust coefficients. $C_T = 0.3$ is for cruise(low thrust) and $C_T = 0.56$ is for climb(high thrust).

2.1.3. PROPELLER SLIPSTREAM CHARACTERIZATION

Propeller interacts with the rest components through its slipstream, thus a description of propeller slipstream flow is necessarily performed. In reality, the slipstream of an isolated propeller features unsteadiness, which is mainly caused by sweeping of rotor wake and tip vortices. The unsteadiness will further affect downstream components in multiple ways: First, it will cause varying distribution of velocity and dynamic pressure in the slipstream, leading to time-dependent performance variation. Second, it will cause enhanced turbulent intensity, which might lead to earlier boundary layer transition. However, a strict treatment of this unsteady problem is rather complex and laborious. Cho and Cho[24] applied a time-averaged analysis of wing performance under propeller effects where the induced velocities in the propeller plane and slipstream were averaged along circumference. As proved by studies[7, 24] that results obtained by use of time-averaged analysis is sufficient for wing performance prediction. In this respect, current study applies time-averaged analysis for prediction of SRV and wing performance under propeller effects and neglect unsteady effects contains in the system.

As pointed out by Veldhuis[4], among all the flow quantities in the slipstream, the velocity distribution and its development is most crucial for wing performance prediction under propeller effects. Thereby the following items will be discussed here:

- Axial velocity
- Tangential velocity

The work performed by Veldhuis[4] helps a lot with description of the mentioned flow quantities.

2.1.4. AXIAL VELOCITY

The velocity in the slipstream can be decomposed as (V_a, V_t, V_r) in a cylindrical coordinate system. In case the axis of propeller thrust is directed in streamwise direction, the V_a component becomes axial velocity component. A typical distribution of this component in axial and radial direction is given in Fig.2.1 and 2.2, respectively.

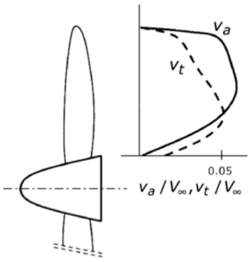

Figure 2.1: Axial velocity averaged over circumference at spanwise direction[4]

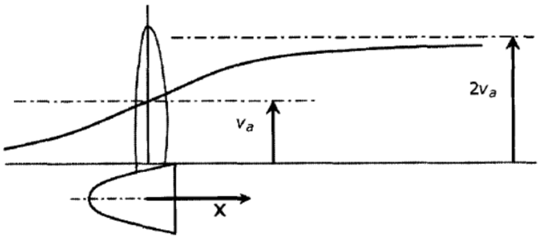

Figure 2.2: Axial velocity averaged over survey plane at streamwise direction[4]

The strong gradient in radial direction is caused by the non-uniform propeller blade loading. The increase of axial velocity in streamwise direction already begins at upstream of propeller plane, which lasts until downstream. This can be explained based on Bernoulli theory that the pressure jump in the propeller plane leads to the axial flow acceleration.

Together with the acceleration of axial velocity is the contraction of slipstream. This can be explained by the law of Conservation of Mass: In order to preserve the mass flow as the velocity increase through the propeller disk, the diameter of the slipstream is somewhat smaller than that at the propeller disk[4].

2.1.5. SWIRL VELOCITY

The propeller torque imparts an angular momentum to the flow passing propeller, which is commonly regarded as swirl [5]. The generation of this term can be explained based on the vortex theory, which will be presented here: Firstly, as Wald [25] and Veldhuis [4] noticed, the velocity distribution at each blade uniquely depend on the freestream flow and trailing vorticies. When looking a downstream plane, the bound vorticity introduces a swirl following the propeller rotation direction, which is assumed to be ω'. On the other hand, a negative swirl $-\omega'$ is presented in front of the propeller. This is physically impossible since the circle at propeller upstream doesn't enclose any vortex line. In order to compensate this component, it must be assumed that the trailing vortex system induces a swirl which is opposite to the one induced by the bound vortex system (thus inducing an angular velocity $+\omega'$) in the upstream domain of propeller, as described in upper part of Fig. 2.3. By adding the effect of both systems, we see that the tangential velocity component is zero everywhere in front of the propeller, and its value is ω in the propeller plane and becomes 2ω far behind the propeller(as described in lower part of Fig. 2.3). An example of tangential velocity profile is presented in Fig. 2.2, as can be seen that radial distribution of tangential velocity differs from the axial velocity, which might due to the loading character of the blades.

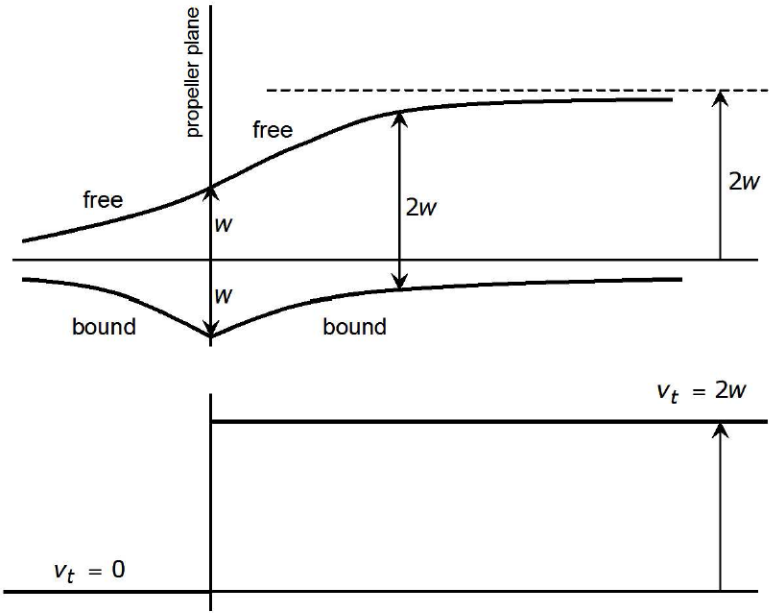

Figure 2.3: Bound and free vorticity induced tangential velocity in slipstream (upper figure) and the superimposed component (lower figure).[4]

Here the swirl angle is introduced that commonly used to show the velocity property in the slipstream, which is defined as follows:

$$\theta_s = \tan^{-1}\left(\frac{v_t}{V_\infty + v_a}\right) \tag{2.8}$$

It is clear that this value depends on both axial and tangential velocity component in slipstream. As is already discussed that the axial component varies in axial direction while the swirl velocity stays constant, this will result in a variant swirl angle distribution in axial direction. In this respect the swirl angle is dependent on the distance towards propeller plane. As a result, the axial position needs to be taken into account for design of wing and SRVs in the propeller downstream.

Since the swirl is originated from the propeller loading, it's impossible to totally remove this term by propeller itself. The design of propeller can help to reduce this term but the capability is limited. This enlightens current study that to install extra components, for example a stator vane or wing, in the propeller downstream where extra performance can be potentially gain by swirl recovery. It can be expected that a severe interference effects will presented in such an arrangement, which further requires the estimation of performance of each components. This will be discussed in the next section.

2.2. INTERFERENCE EFFECTS IN AN INTEGRATED PROPELLER-SRV CONFIGURATION

In order to understand the complicated interaction effects in a propeller-SRV-wing configuration, a good starting point is to investigate a basic propeller-SRV arrangements. According to studies [3, 5, 26], the upstream effect of SRVs on the propeller performance is negligible, as a result the interaction effects is simplified as velocity in slipstream is tiled by SRV. A section of the SRV blade is presented in Fig. 2.4 for understanding the working principle of SRV:

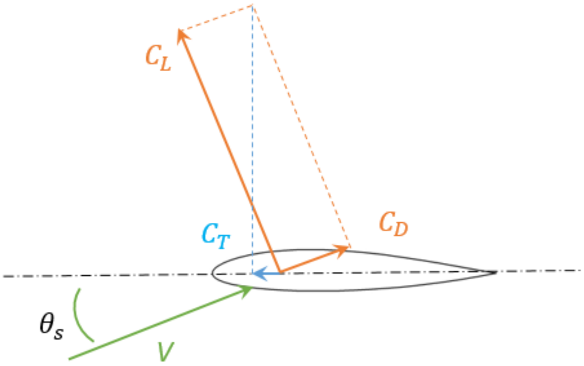

Figure 2.4: Velocity and force diagram of one vane section under zero pitch with a velocity V with swirl angle θ_s.

As already discussed in Sec. 2.1, propeller induces an axial velocity V_a and tangential velocity V_t in slipstream. This flow quantity will generate a resultant aerodynamic force when on SRV section immersed in the slipstream, this force can be further decomposed in perpendicular and parallel direction with respect to the incoming velocity, being the lift (C_L) and drag (C_D), respectively. Another decomposition is in the axial and tangential direction, being the thrust (C_T) and torque (C_Q). In this case, only the thrust term is considered which can be calculated from:

$$dC_T = dC_L sin(\theta_s) - dC_D cos(\theta_s) \tag{2.9}$$

where θ_s is the swirl angle in the slipstream. The relation between lift and velocity is stated in Kutta Joukowski theorem: The resultant aerodynamic force in an incompressible, inviscid, irrotational flow in an unbounded fluid is of magnitude $\rho V \Gamma$ per unit width and acts in a direction normal to the inflow[11]. The circulation Γ, which is related to rotating flow induced by the lift producing airfoil, is pointing clockwise in this case. Thereby a downwash is presented at the downstream position. It's easy to prove that the SRV induced velocity is opposite to the propeller induced tangential velocity. By superimposing this two velocity components it's realized that the propeller induced swirl is recovered by SRV. This effect is also supported in experiment performed by Li [6]. The flow domain obtained in the experiment is presented in Fig. 2.5 below:

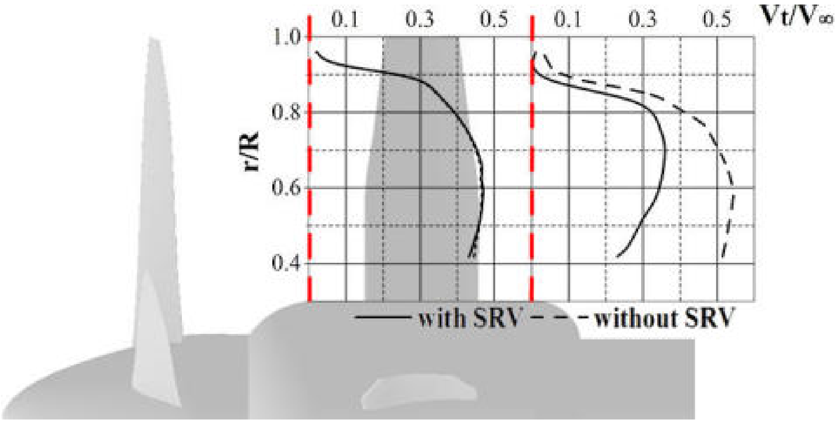

Figure 2.5: Quantified swirl change by installed SRVs from PIV measurements[6].

Comparison is made of the swirl velocity in two survey planes with and without SRV by use of PIV measurements. The experiment was performed at a high thrust condition of a 6-blade propeller, with 4 SRVs designed for uniform inflow installed at a downstream position. As is observed that no difference is caused by SRVs at the upstream plane. This also supports the conclusion that SRVs has negligible effects on the performance of an upstream propeller. When looking at the velocity comparison at SRV downstream, it's recognized the swirl is reduced due to SRV, and the amount of the swirl recovery increases towards the nacelle.

It can be expected that with increasing number of vanes, the swirl residual will be further reduced. Moreover, no significant difference is observed for axial velocity change. Study performed by Stokkermans et al.[5] found a small reduction of axial velocity in downstream of the SRV at cruise condition due to an increase of the slipstream boundary. Both studies have proved swirl recovery caused by SRVs. As a conclusion, the interaction effects in a propeller-SRV arrangement is simplified as the swirl in propeller slipstream is recovered by downstream mounted SRVs and a closely coupled propeller and SRV configuration features higher thrust with lower swirl. The next step is to introduce the SRV in a propeller-wing configuration. It can be expected that due to wing induced upwash, conclusion drawn on swirl recovery effects by SRV may not hold any more.

2.3. INTERFERENCE EFFECTS IN AN INTEGRATED PROPELLER-SRV-WING CONFIGURATION

The introduction of wing trailing a propeller basically introduce an upwash at its upstream position, which will change the inflow condition of both propeller and SRVs, and the SRVs will also tilt the inflow condition of wing leading to deviation of wing performance. Consider the difficulty in addressing this interaction effects, this section will first refer to the classical propeller-wing interaction problem, and further discussion will be on how introduction of SRVs affect the system performance.

2.3.1. EFFECTS OF PROPELLER AND SRV ON WING

The most direct effects of propeller on wing is the changes of local angle of attack of the wing part washed over by the slipstream [22]. The flow inside the slipstream is characterized by an increase of the axial velocity and tangential velocity. These additional velocities will mainly affect wing lift, induced drag distribution. Firstly, the slipstream effects on the wing lift distribution is presented. The axial and tangential velocity effects will be illustrated separately for better understanding.

WING LIFT CHANGES

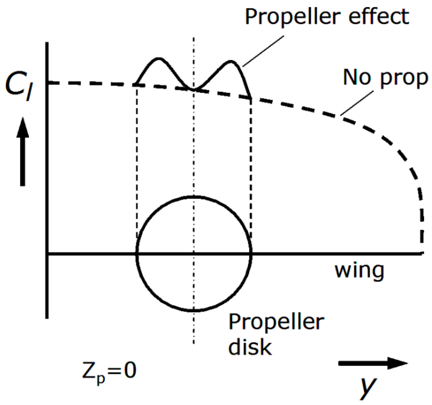

Figure 2.6: Changes in wing local C_l due to the axial velocity increase in the slipstream[4]

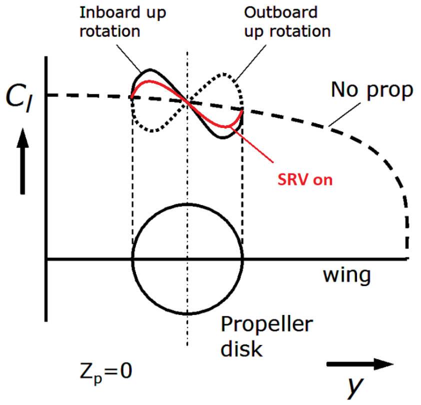

Figure 2.7: Changes in wing local C_l due to the swirl velocity in the slipstream[4]

Fig. 2.6 illustrates the changes in local lift coefficient resulted from the axial velocity increase over the slipstream region. As the flow is accelerated due to the rotating propellers, the dynamic pressure over the wing is increased, resulting in an increase in local lift. As a result, the shape of lift distribution follows the non-uniform axial velocity profile along the propeller blade as mentioned in Subsection 2.1.4. A maximum lift is found at the same radius for both the up-going and down-going blade locations.

Fig. 2.7 presents the effect of propeller swirl on wing lift distribution. As is opposite to the axial flow effects, the part of wing that follows up-going blade experiences an increased lift, whereas the down-going blade side features reduced lift. This is due to the reason that the upwash causes an increase of the angle of attack, while the downwash causes a lower angle of attack, and the lift will be deviated corresponding.

As for the SRV effects on wing lift distribution, due to the swirl recovery effects as discussed in Sec. 2.2, the wing lift distribution resulted from the propeller swirl would be less significant, as roughly depicted in the sketch 2.7. In another words, the installed SRV simply damp the lift deviation caused by the propeller. It should be noted that the wing effects on SRV is neglected here, and it's assumed SRVs only lead to change of swirl velocity and the axial velocity is not affected. It gives a basic idea of how wing lift change is related to the velocity variation in the slipstream.

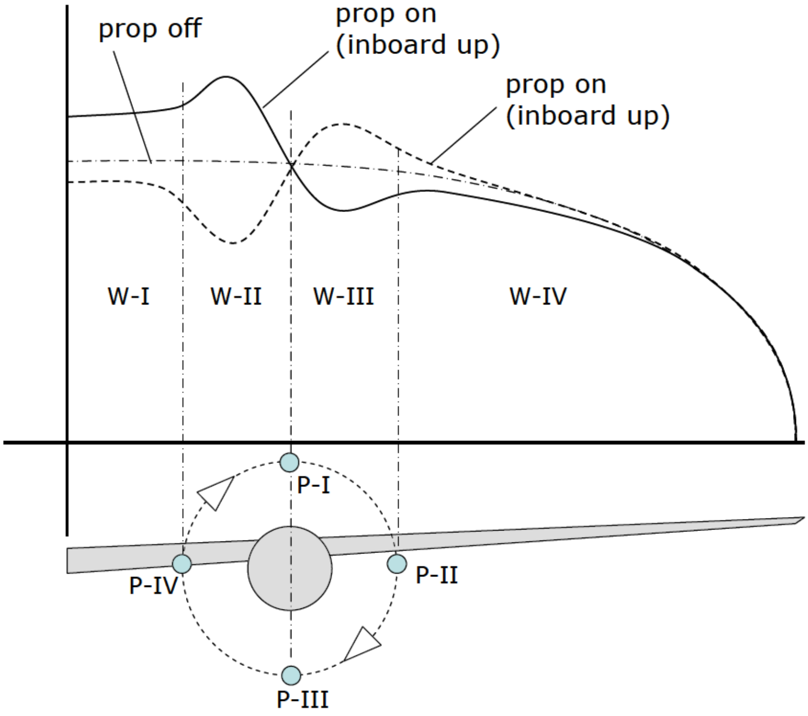

Figure 2.8: Changes in wing lift distributions due to the combined effect of the axial and the tangential velocity component in the slipstream[4].

A more realistic lift distribution due to propeller effects is given by Veldhuis[4]. As can be seen in Fig. 2.8 that the lift distribution is deviated both within and outside slipstream due to installed propeller. The change in slipstream region is just discussed, which can be seen as the effect caused by superimposed axial and tangential velocity. According to Veldhuis [4], the lift changes outside of propeller slipstream is caused by the distorted vorticity sheet. Another explanation if given by Epema et al.[22]: The lift increase at the boundary between $W-I$ and $W-II$ sheds a trailing vorticies, which induces an upwash in $W-I$ increasing the local angle of attack and the lift. Similarly, the generated trailing vortex between $W-III$ and $W-IV$ induces a downwash at $W-IV$, leading to a lower lift at that region.

WING INDUCED DRAG CHANGES

In additional to lift deviation, the wing drag distribution is also distorted by propeller. Due to the fact that the swirl induced by propeller works in the same way as wing induced 'downwash', it mainly lead to deviation of wing induced drag. A study of this effects is performed by Veldhuis [4], where comparison is made between induced drag distribution and 'downwash' distribution behind the wing for an inboard-up rotating propeller. The simulation result is depicted in Fig. 2.10, where downwash induced by wing and propeller is separately presented for clear illustration. It should be noted that a positive V_n means a downwash pointing downwards. It can be seen that wing induced downwash is locally enhanced at the up-going blade side, which is caused by the local lift increase. When the swirl in slipstream is superimposed, the resultant flow becomes upwash. This upwash results in a more forward rotated lift vector on the local airfoil section, as depicted in Fig. 2.11, which would cause a negative induced drag term. This can also be explained based on Kutta-J theory, according to $L = \rho V \Gamma$, the cross product of an upwash velocity vector V and a inward pointed Γ is a forward pointed lift, which is actually a negative drag. In this respect the local induced drag is reduced due to propeller induced upwash. As for the induced drag increase at down-going blade side, which can be explained by the same reason, with only difference that propeller induces a 'downwash'.

It can be summarized that, at the wing downstream position, wing always induces a velocity which is opposite to swirl induced by propeller, such that wing is working as a swirl recovery vane. Then next question is raised that how the wing induced drag is reduced by propeller induced swirl. As explained by Veldhuis [4] that, due to the gradient in wing lift distribution, the positive and negative drag contributions at UBS and DBS are of unequal magnitude. In case the forward rotated force is larger than the backward rotated force, a wing drag reduction can be obtained. It's expected that the wing induced drag reduction can be maximized by wing circulation optimization.

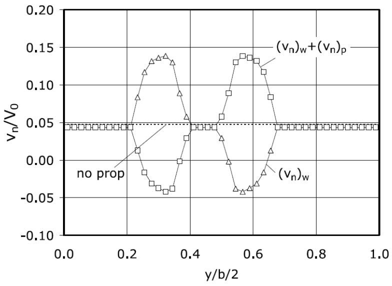

Figure 2.9: The downwash distribution behind the wing (effect of wing (w) and the propeller(p) swirl velocity) [4].

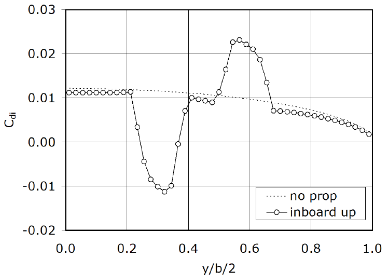

Figure 2.10: Comparison of the spanwise distribution of the induced drag coefficient[4].

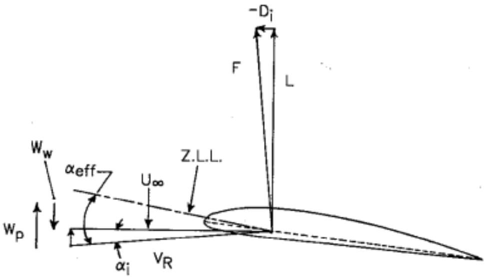

Figure 2.11: Wing section in propeller upwash[7].

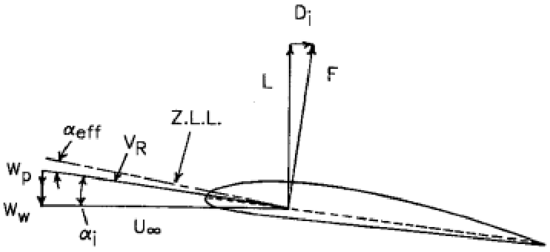

Figure 2.12: Wing section in propeller downwash[7].

2.3.2. EFFECTS OF WING ON PROPELLER AND SRV

Up to now, only propeller and SRVs effects on wing performance is investigated, assuming that the wing has no effects on the performance of propeller and SRVs. This section will investigate the upstream effects of wing on propeller and SRV separately.

EFFECTS OF WING ON PROPELLER

Wing induced velocity at propeller mainly lead to a variable inflow condition for individual blade in one revolution. This effect is similar to the situation where propeller is inclined with respect to incoming flow [4]. In order to understand such effects, observation is made of the wing induced velocity at the propeller plane, as is presented in Fig. 2.13. The velocity data is obtained from a wing surface singularity model and the wing source (σ) and doublet (Γ) induced velocity is separately plotted (at first row and second row, respectively) in order to provide a clear illustration. Focus should be on the axial and tangential velocity (depicted in subfigures at first and second column, respectively) as they mainly determine the blade inflow angle. As can be seen from the first subfigure of third row that the axial velocity V_a is enhanced at the upper plane and decreased at the lower side, which is mainly caused by the Γ induced velocity. When looking at the tangential velocity V_t contour, the doublet mainly lead to an upwash at up-going blade side and a downwash at the down-going blade side. With superimposed source induced velocity, the non-uniformity is slightly tilted in propeller rotation direction. The next step is to investigate how this circumferential non-uniformity affect the propeller performance.

A detailed explanation of this effect is given by Veldhuis [4], who investigates the local inflow angle of one blade in different azimuthal positions in a wing-mounted tractor propeller configuration. The conclusion will be introduced here.

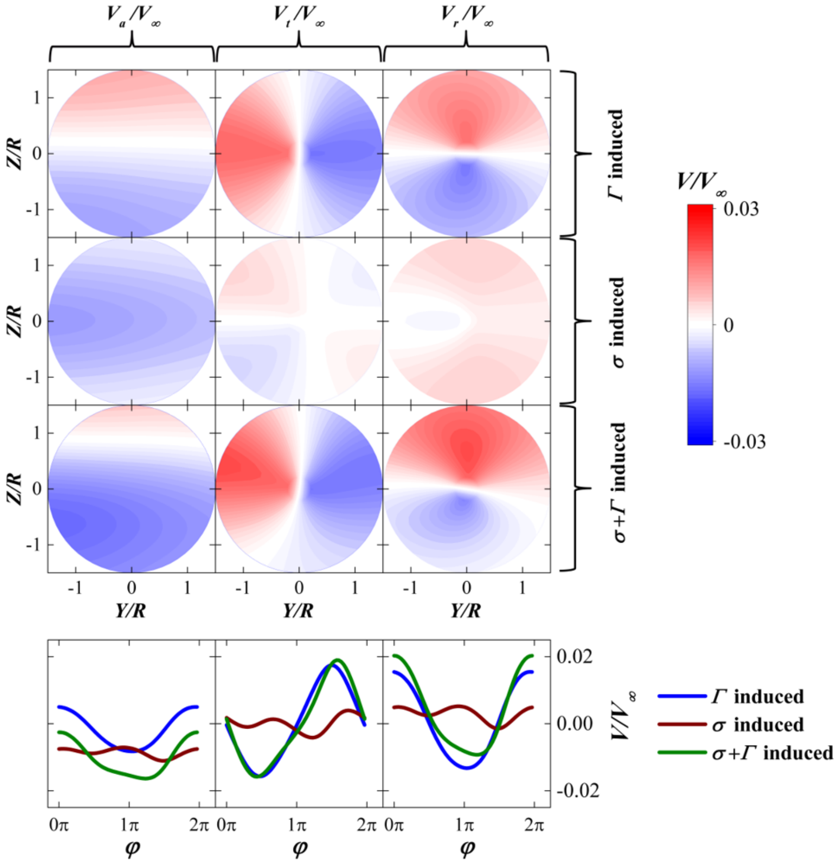

Figure 2.13: Wing induced velocity in propeller plane from panel result

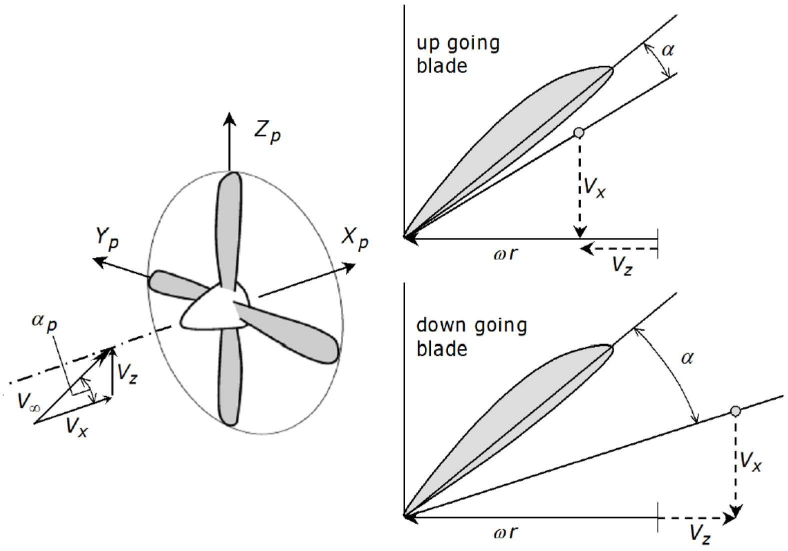

Figure 2.14: Blade angle of attack variation due to propeller pitch angle α_p.[4]

The investigation will be performed by use of the propeller-wing configuration presented in Fig. 2.8, in which the propeller blade is defined at four positions $P-I$, $P-II$, $P-III$, $P-IV$ where $P-IV$ and $P-II$ follows up-going blade and down-going blade while $P-I$ and $P-III$ is high blade and low blade position, respectively. Difference between the local inflow angle of $P-IV$ and $P-II$ is caused by the wing induced tangential velocity as presented in Fig. 2.13. The $P-IV$ experiences a lower angle of attack because part of the tangential velocityωr of blade is counteracted by the wing upwash velocity. This leads to a reduction of propeller loading. While the $P-II$ experiences an enhanced tangential velocity thereby an increased blade loading is obtained. The $P-I$ features decreased angle of attack because of axial velocity enhanced by the wing induced axial velocity at wing upper surface side, and a corresponding reduction of the blade loading happens. In the similar way, the $P-III$ experiences an increased blade loading due to the decreased axial velocity caused by the wing.

EFFECTS OF WING ON SRV

The varying blade loading of propeller and the wing induced velocity together enhance the non-uniformity of slipstream. This will lead to highly deviated inflow angle for SRVs installed in between propeller and wing. In order to see this non-uniformity, first the wing induced velocity distribution by use of the same wing surface singularity model is presented.

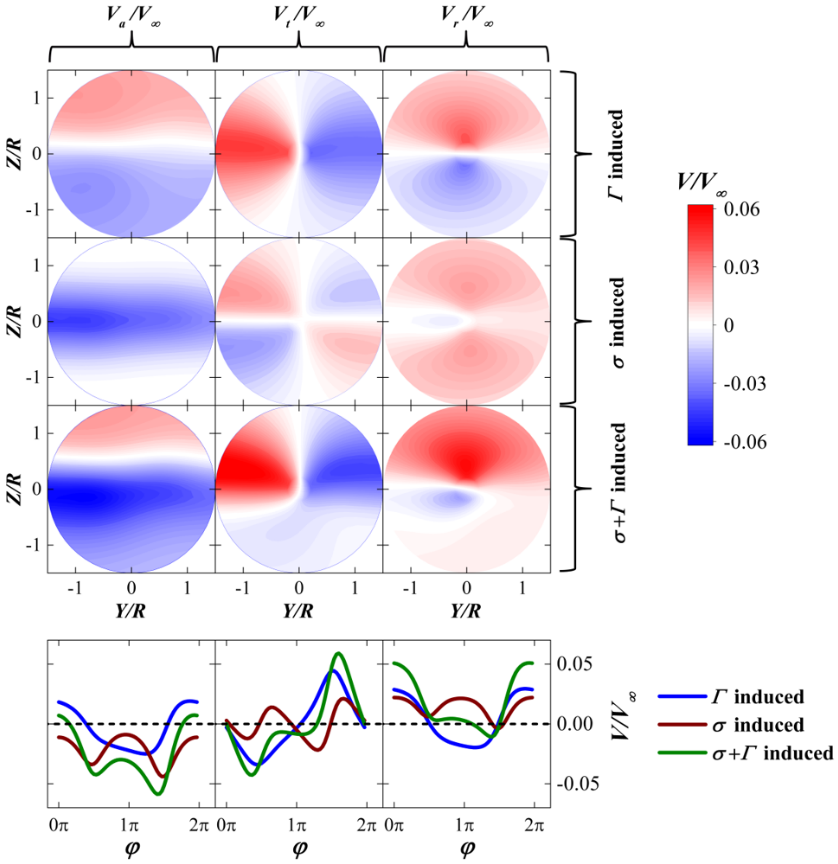

Figure 2.15: Wing induced velocity in SRV plane from panel result

As can be seen in Fig. 2.15, wing induced velocity distribution in the SRV plane features almost the same pattern as the propeller plane depicted in Fig. 2.13 with only an enhanced magnification. This does make sense as the SRV is located closer to wing, thereby it experiences an enhanced velocity induced by the wing. However, difference is observed in the tangential velocity distribution, where the swirl seems to be removed at the part under the wing, whereas the swirl is enhanced at the upper part. This can be explained by looking at the subdivided velocities induced by source and doublet, respectively. At the lower part of plane, doublet induced swirl counteract that induced by source, whereas these two terms are accumulated at upper part of plane. It is expected that the SRV should be positioned at the region features highest swirl to produce maximized thrust. As a matter of fact, in addition to the non-uniformity caused by wing induced velocity, the varying blade loading of propeller already leads to a non-uniform slipstream which initiates from the propeller plane and develops along downstream. However, this uniformity is diminished by a time-averaged result and it's also hard to address by use of potential flow analysis.

It can be concluded that in a wing-mounted tractor propeller arrangement, the wing mainly cause a non-uniform velocity distribution along circumference at its upstream position. Thereby the azimuthal position (ϕ_i) of the vanes should be properly selected to make full use of the swirl energy. It is expected that the SRVs with non-uniform azimuthal spacing tend to provide highest thrust. It's noted that, by introducing such SRVs system, the loading of each vane is no longer identical and the total force of the entire SRV system is no longer symmetrical, and a lateral force and lift force would be produced. This should be considered when accessing the system performance.

In additional to the mentioned effects, in fact the wing also causes a deformation of the propeller slipstream, which mainly include a slipstream contraction and lateral deformation. This will further lead to changes in inflow condition and so as to the loading of wing. These effects is hard to model in the potential flow method. As already discussed in Chapter 1 that the wing performance obtained using Euler simulation will be applied to correct the corresponding results from potential flow method. In this way the difficulty in modeling the slipstream deformation in the potential flow code will be avoided, while the wing performance deviation caused by the slipstream deformation can still be considered.

2.3.3. DISCUSSION

Several conclusions can be drawn form a preliminary analysis:

- In a wing-mounted tractor propeller arrangement, the wing mainly cause a non-uniform velocity distribution along circumference at it’s upstream position.
- The non-uniformity caused by variable propeller loading can be neglected in a time-averaged analysis of SRV performance.
- The azimuthal position (ϕ_i) of the vanes should be properly selected to make full use of the swirl energy in the slipstream that distorted by wing.
- The wing performance deviation is mainly caused by the propeller and SRV induced swirl and slipstream deformation, while the former effects can be addressed in potential flow theory and the later one will be corrected by use of Euler simulation result.

This chapter only focuses on a qualitative analysis of the interaction effects, in order to obtain a quantitative results, the analysis tools need to be implemented to predict the individual performance accounting for their interaction effects. The related work will be introduced in the next chapter.

3

METHODOLOGY

This chapter mainly focus on the construction of analysis tool for the design optimization problem at issue. In order to perform a surrogate-based multi-fidelity optimization, a physical-based surrogate model needs to be constructed that correlates low-fidelity model with high-fidelity analysis. In order to make sure the design is reasonable, a baseline configuration is selected and a design condition is properly calculated. Then the focus will be on the construction of low-fidelity analysis module, followed by an introduction to the high-fidelity analysis method. Finally the construction of surrogate model and multi-fidelity optimization framework will be presented.

3.1. CONFIGURATION AND CONDITIONS

In order to carry out a reasonable design of both wing and SRV, an aircraft model is selected and described as below.

3.1.1. CONFIGURATION

The propeller in use is a 6-blade propeller [27], which is used in a regional turboprop aircraft. As can be seen in Fig. 3.1 that it features radius of $0.2032[m]$ and hub radius of $0.0442[m]$. Its blade pitch was set as $50[°]$ at 70% of the blade span. The geometry is depicted in Fig. 3.1.

As for the baseline wing model in use, a scaled Fokker F50 wing was chosen. The wing is scaled to such that the ratio of propeller diameter to wing span is kept the same with the original aircraft. The properties is presented in Table 3.1.

The propeller is located $2R$ in front of the wing quarter-chord-line, $2R$ outboard of the wing root. The fuselage, wing sweep and wing dihedral are neglected for simplification.

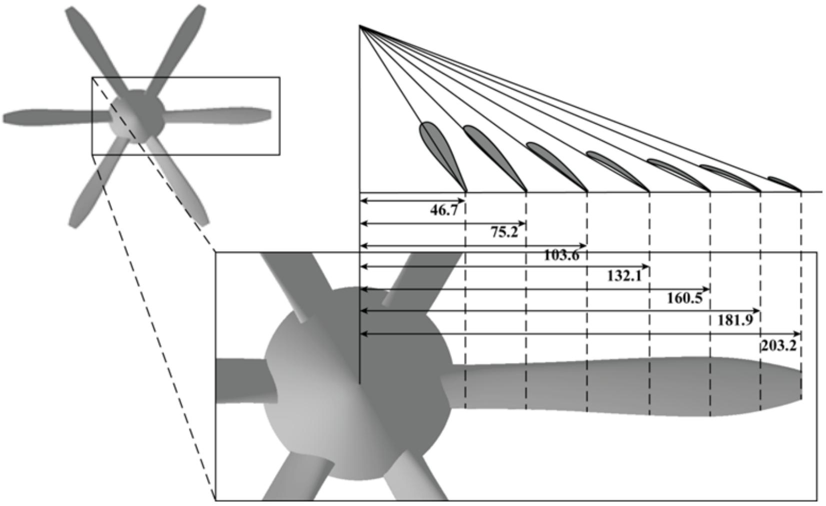

Figure 3.1: Propeller model[6]

Variable	Value
Span, b	3.331 m
Root chord length, c_r	0.3842 m
Taper ratio	0.396
Area	0.8933 m^2
Quarter chord sweep	0 °
Dihedral	0 °
Twist	0 °
Root airfoil	NACA 64_2-415
Tip airfoil	NACA 64_2-415

Table 3.1: Wing geometry properties

3.1.2. CONDITIONS

The next step is to set a reasonable cruise condition for analysis. The main objective is to properly select a wing lift coefficient C_L and propeller thrust coefficient C_T for the mentioned configuration to make sure the design is realistic.

The design condition is set as the cruise condition of ART-72 aircraft, which corresponds to height of 5000 $[m]$ and Mach number of 0.44. The dimensions of this aircraft is depicted in Fig. 3.3. Since the propeller and wing used in current study are different from the original design of ATR-72, their performance(C_T and C_L) have to be re-calculated. The calculation is based on an aircraft re-sizing method developed by Nita [8]. This method was initially developed for design of jet-powered aircraft and Nita [8] has adapted it for design of a propeller-driven aircrafts.

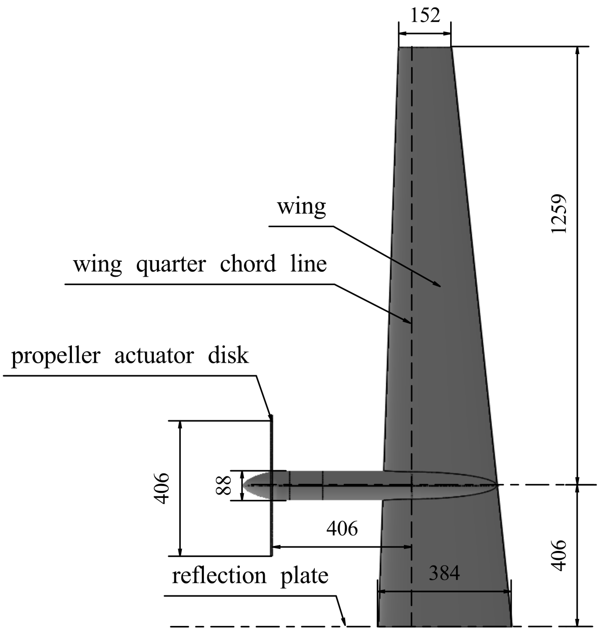

Figure 3.2: Sketch of propeller-wing configuration (dimensions in millimeters) [9]

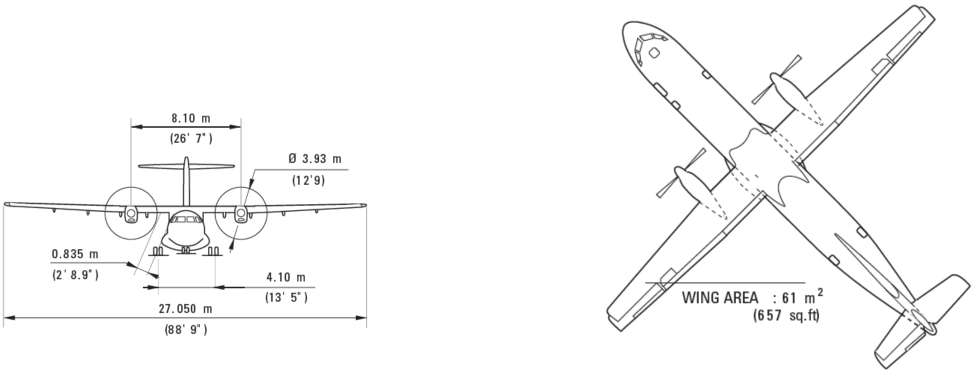

(a) Front view

(b) Top view

Figure 3.3: Standard Configuration of ATR 72-500.[8]

The major performance parameters to be determined are the C_T for propeller and C_L for wing. Since at the cruise condition the aircraft is in equilibrium, thus two equations can be used: Lift = Weight and Drag = Thrust. Both parameters are a function of altitude and are calculated separately. [8]

From the equation of lift equal to weight, we can obtain the analytic expression of the wing loading:

$$\frac{m_{MTO}}{S_W} = \frac{C_L \cdot q}{g} = \frac{C_L \cdot M^2}{g} \cdot \frac{q}{M^2} \tag{3.1}$$

For the cruise flight, we use the mass from take-off in order to have a safety margin when sizing the aircraft. From literature [8] it is know m_{MTO} is around 22000 $[kg]$, and the original wing reference area S_w is 61 $[m^2]$, which can be found at Fig.3.3. The dynamic pressure can be calculated from $q = \frac{1}{2}\rho V_{CR}^2$, where ρ is 0.7364 obtained from a Standard Atmosphere data [28] at the cruise altitude of 5000 $[m]$. The cruise speed V_{CR} is assumed to be 140 $[m/s]$, then C_L is the only unknown in Eq. 3.1, calculated to be around 0.5.

For the calculation of propeller thrust coefficient C_T, first the total thrust should be calculated. For this purpose, the relationship of Drag = Thrust is used. As the total lift has been determined, the total drag of entire aircraft can be obtained by use of lift to drag ratio $E = L/D$. For the cruise flight we assume aircraft was flying with maximum lift to drag ratio $E_{max} = L/D_{max}$ [8]. The E_{max} can be obtained from statistics. According to Fig. 3.4, for the ATR 72 turboprop, L/D_{max} has the value of 17.

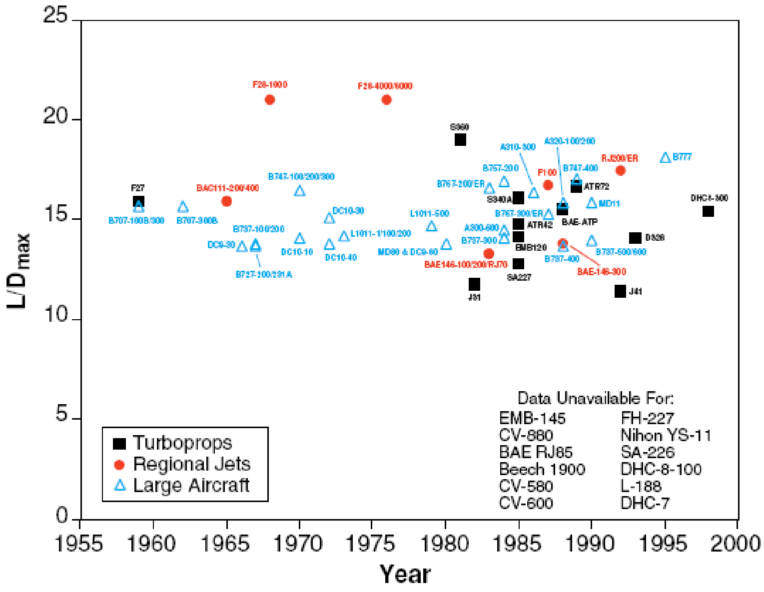

Figure 3.4: Lift to drag ratio for different aircrafts[8]

Then total drag D can be calculated from equation $D = (L/E)_{max}$. As already discussed, the drag term is balanced by the thrust produced by all set of propellers $D = \sum_{i=1}^{N} T_i$. In this configuration the number of propellers $N = 2$, thus the individual thrust produced by one propeller is $T = \frac{1}{2} * D$. The propeller thrust coefficient C_T is defined by the equation in Table 2.1, since the diameter D has been determined, leading to the only unknown of rotational speed n. The problem is to determine the propeller rotational speed n or advance ratio J where the required thrust can be achieved, while maintaining a high propulsive efficiency. This work was performed by Li [9], in this study an advance ratio J of 2.4 was selected and thrust coefficient was computed to be $C_T = 0.22$. As a conclusion, the cruise condition for current propeller-wing configuration is calculated to be $C_L = 0.5$ for wing and $C_T = 0.22$ for propeller.

3.2. LOW-FIDELITY ANALYSIS MODULE

This section will introduce low-fidelity analysis module for a propeller-SRV-wing configuration. In order to have a fast estimation of system performance, it assumes the performance and the velocity distributions in propeller slipstream is constant. This method has been used in study [29] for analysis of a typical propeller-wing interaction effects. Three modules were established corresponding to three components involved:

- Isolated propeller module for slipstream establishment
- SRV design module in propeller-wing induced velocity field
- Wing analysis module in propeller-SRV induced velocity field

3.2.1. PROPELLER SLIPSTREAM SETUP

The design of SRVs or wing behind a tractor propeller requires a quantified description of the flowfield at installation position as design input. As pointed out by Li et al.[6], the axial velocity V_a and tangential velocity V_t are critical input for the SRV design. Thereby an accurate prediction is necessarily carried out. In this study the slipstream is established based on the RANS simulation of isolated propeller due to its high accuracy, the results of which will be discussed in this section. For details of the CFD setup readers can refer to work by Li et al. [6, 9]. The mesh consists of structured mesh surrounding the propeller and an unstructured mesh filling the rest domain. The Shear Stress Transport (SST) turbulence model was used together with the automatic wall function. The results were validated by experimental data in terms of both the propeller performance coefficients and the velocity distribution behind the propeller.

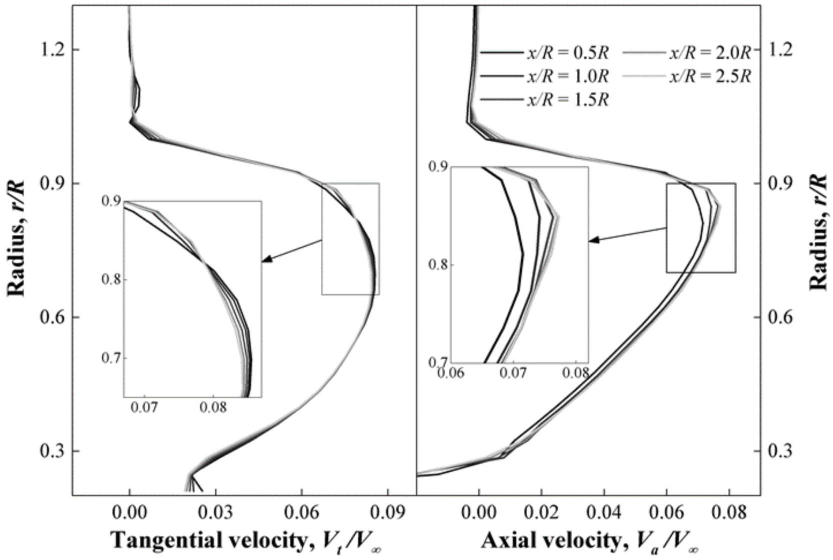

Figure 3.5: Velocity distributions in propeller slipstream obtained from RANS simulation at $C_T = 0.22$ and $J = 2.4$.[9]

Fig. 3.5 presents the slipstream data obtained from simulation. Five survey planes at different stream-wise positions ranging from $0.5R$ until $2.5R$ were selected to depict stream-wise development of the velocity distributions. It can be seen that V_t distributions is almost un-changed at stream-wise direction, whereas an acceleration of V_a along stream-wise can be observed. This is in consistent with the phenomenon as discussed in Sec. 2.1. The slipstream model containing velocities averaged along circumference is directly incorporated in the low-fidelity SRV and wing analysis model, and the propeller induced velocities are interpolated at wing and SRV collocation points. This "add on" slipstream model has been widely used in many studies [4, 30, 31].

3.2.2. SRV DESIGN MODULE

This section will introduce SRV analysis and design module based on lifting line method. Studies [5, 6] have performed SRV design for an isolated propeller, where velocities is uniform along circumference. As is known from Chapter 2, SRV designed for uniform inflow is no longer feasible for a non-uniform flow field induced by propeller and wing. Thereby the SRV design framework has to be modified for this purpose. The related work has been performed by Li et al. [6], which will be applied in current study as it suits the project well. This section will first focus on the basic formulation of SRV lifting line model, then the modifications for non-uniform inflow will be presented.

SRV LIFTING LINE MODEL

Consider the main goal of the study, analysis tool should fulfill a series of requirements:

- Fast and accurate prediction of SRV performance for optimization purpose.
- Be capable of modeling the wake field and induction effects of SRVs such that the interaction effects between SRVs and other lifting surfaces, for example wing, can be accessed.

In this respect, the Prandtl lifting line theory can be applied. This simplified analysis method neglects the thickness effects and the chordwise performance characters, which is acceptable in a preliminary design stage.

The SRV lifting line model is based on OPENPROP [10], which is originally developed for design and analysis of propellers. Then Li et al.[6] adapted it for SRV design as it gives good prediction of blade forces and converges quickly to optimal blade parameters such as blade number and loading distribution. In this tool, the vane can be modeled by discretized horseshoe vortex, such that a radial circulation distribution and a wake model of vortex sheet can be obtained, which makes it attractive for optimization of vane loadings and modeling of SRV interaction effects with other lifting surfaces. Fig. 3.6 illustrates the basic formulation and assumptions of the lifting line model:

- The vanes are simplified into N lifting lines featuring equal angular spacing and identical loading.
- The wake model of the vanes consists of helical vortices with constant radius and pitch. Each of the trailing vortex is aligned with the total velocity at the shed position such that helix pitch angle $\beta_v(r)$ is related to the local inflow angle $\beta_i(r)$.

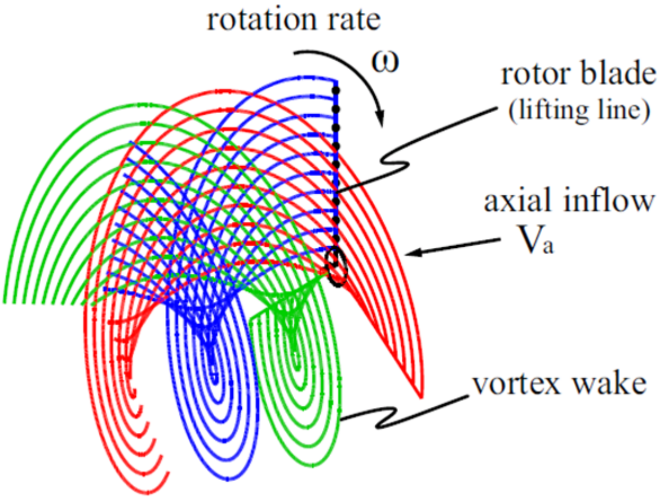

Figure 3.6: Conventional lifting line model[10]

The lumped vortex theory states that a symmetrical and zero thickness airfoil can be represented from far field perspective by a single vortex positioned at its center of pressure, namely its quarter chord point. By specifying the non-penetration boundary condition at the 3/4 chord collocation point, this model represents faithfully the thin airfoil and automatically respects the Kutta Condition. [11]

In order to obtain the radial circulation distribution $\Gamma(r)$ along each blade, the blade is discretized into elements represented by horseshoe vortex with constant Γ. Fig. 3.7 illustrates the velocities and forces (per unit radius) on a blade section: axial and tangential inflow velocities, V_a and V_t; induced velocities from wake and the rest bound vortex, v_a^* and v_t^*. The total velocity has magnitude $V^* = \sqrt{(V_a + v_a^*)^2 + (V_t + v_t^*)^2}$ and pitch angle is defined by:

$$tan\beta_i = \frac{V_a + v_a^*}{V_t + v_t^*} \tag{3.2}$$

Also shown on Fig. 3.7 are the angle of attack α, blade pitch angle $\theta = \alpha + \beta_i$ and circulation Γ_i. The SRV induced velocity v_a^* and v_t^* and Γ_i are correlated in equations:

$$u_a^*(m) = \sum_{i=1}^{M} u_a^*(m,i)\Gamma_i \tag{3.3}$$

$$u_t^*(m) = \sum_{i=1}^{M} u_t^*(m,i)\Gamma_i \tag{3.4}$$

where $u_a^*(m,n)$ and $u_t^*(m,n)$ are the influence coefficients computed from Biot-Savart Law. They are related to the geometry of lifting line model, thereby are constants for a fixed wake model. The aerodynamic forces can be calculated by applying Kutta–Joukowski theorem at bound vortex:

$$F_i = \rho V \times \Gamma_i \tag{3.5}$$

where the velocity V consists of freestream velocity V_∞, propeller induced velocity $V_{prop,i}$ and induced velocity from SRV vortex system except for the current bound vortex $V_{SRV,i}$, expressed as:

$$V = V_\infty + V_{prop,i} + V_{SRV,i} \tag{3.6}$$

The aerodynamic forces produced by stator vanes is decomposed into thrust F_t and normal force F_n. As already discussed in section that all the forces has to be considered since it will contribute to the system performance. In order to obtain a thrust and drag balance the viscous drag should also be considered. This can be calculated by use of equation:

$$F_v = \frac{1}{2}\rho V^2 C_d c \tag{3.7}$$

where C_D is the drag coefficient obtained from Xfoil [32] and c is the local airfoil chord. The thrust F_t and normal force F_n on the vanes are calculated from equations:

$$F_t = N\sum_{i=1}^{M}(F_i cos\beta_i - F_v sin\beta_i)\Delta_r \tag{3.8}$$

$$F_n = N\sum_{i=1}^{M}(F_i sin\beta_i + F_v cos\beta_i)\Delta_r \tag{3.9}$$

Reformulate the Eq. 3.8 into a discretized form, further combined with Eq. 3.5, 3.7 and 3.2 yields the expression for thrust F_t:

$$F_t = \rho N \sum_{n=1}^{N}\sum_{m=1}^{M}((V_{t_{m,n}} + v_{t_{m,n}})\Gamma_{m,n} - \frac{1}{2}V_{m,n}^{*}C_{d_{m,n}}c_{m,n}(V_{a_{m,n}} + v_{a_{m,n}}))\Delta r_{m,n} \tag{3.10}$$

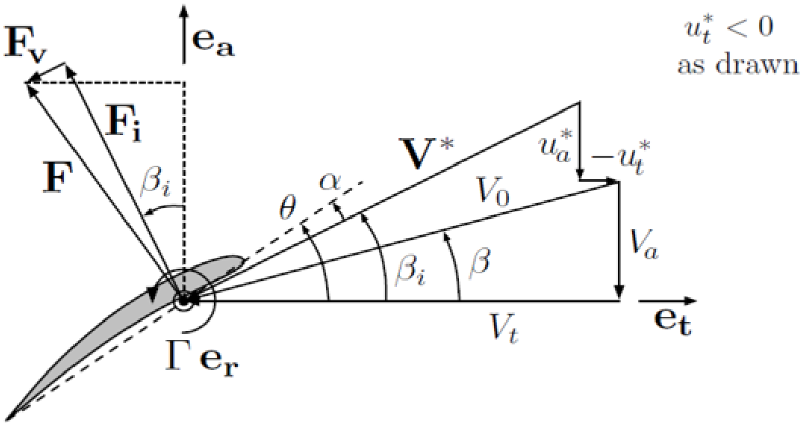

Figure 3.7: SRV velocity diagram at radius r [10]

SRV DESIGN FOR MAXIMUM THRUST COEFFICIENT

The SRV design is to find the optimum circulation distribution Γ for a given inflow (V_a, V_t, ω) and blade outline (c, C_D), such that efficiency is maximized for a prescribed thrust. For the SRV case, design problem is simplified into determination of the optimum radial circulation distribution which maximizes vane thrust without constraints. The problems can be solved by setting partial derivative of F_t with respect to the circulation distribution Γ as zero:

$$\frac{\partial F_t}{\partial \Gamma_{m,n}} = 0 \tag{3.11}$$

Based on previous research [6], the C_D and c distributions have negligible effect on the circulation distribution, then the problem is simplified as:

$$\frac{\partial F_t}{\partial \Gamma_{m,n}} = (V_{t_{m,n}} + v_{t_{m,n}})\Delta r_{m,n} + \sum_j \sum_i \frac{\partial v_{t_{i,j}}}{\partial \Gamma_m} \Gamma_{i,j} \Delta r_{i,j} = 0 \tag{3.12}$$

The partial derivatives of induced tangential with respect to the circulation $\frac{\partial v_{t_{i,j}}}{\partial \Gamma_m}$ are actually the influence coefficients as reported in Eq. 3.3 and 3.4, respectively. This formed a non-linear equation systems which can be solved by Newton's method. After determining the circulation distribution, the airfoil shape design module will be applied to minimize the viscous drag of SRV while maintaining the desired circulation distribution, for the detail reader can refer to study by Li et al.[9].

ADAPTED SRV DESIGN MODULE FOR PROP-WING INDUCED VELOCITY

As already reported in Sec. 2.3.2, the axis-symmetric inflow of SRVs from isolated propeller is altered by the wing induced flow field such that the velocity field is non-uniformly distributed along circumference. This requires a series of modifications to the SRV analysis and design module:

- The azimuthal positions ϕ of vanes and number of vanes N should be optimized in order to maximize thrust production.
- A design space exploration of the vane azimuthal positions ϕ needs to be performed in order to make full use of the swirl energy, a global optimization algorithm is needed for this purpose.
- The non-uniform inflow will lead to variable inflow angle of attack and unique optimum load distribution for vanes at different azimuthal positions. This requires the optimization of circulation distribution be performed individually and simultaneously for each vane.

The modifications have been implemented as follows:

- The unified lifting line model has been modified that each vane features non-equal circumferential spacing. The modification can be observed by comparing Fig. 3.8 and 3.9.
- The calculation process for optimum circulation distribution have been applied for each vane.
- The design space exploration of vane positions can be performed by use of a global optimization algorithm, which will be introduced in Sec. 3.4.2.

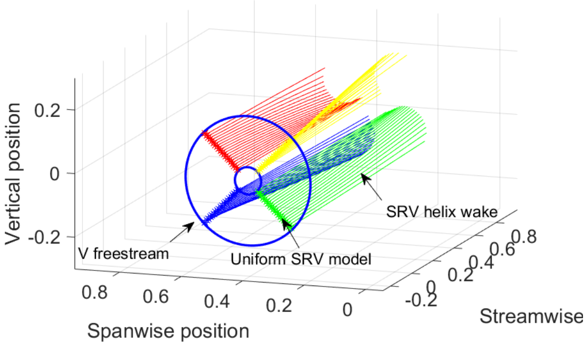

Figure 3.8: Uniform distributed Lifting Line Model

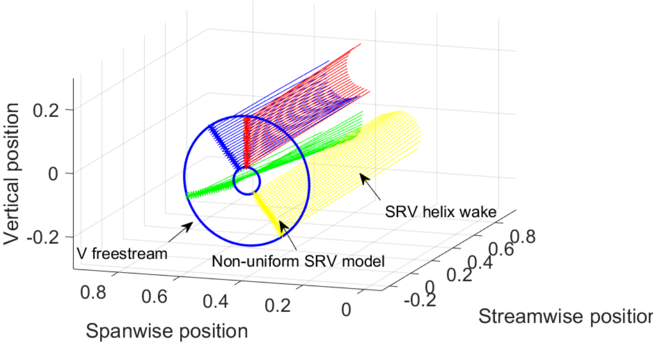

Figure 3.9: Non-uniform distributed Lifting Line Model

The SRVs will be designed in propeller and wing induced velocity field, where the propeller slipstream velocity has been established prior to the SRV design, whereas wing induced velocity $V_{wing,i}$ is obtained from wing analysis module. The velocities at a specific SRV collocation point is modified as :

$$V = V_{\infty} + V_{prop,i} + V_{SRV,i} + V_{wing,i} \tag{3.13}$$

As a consequence, the pitch angle needs to be re-calculated based on the modified total velocity. This means $V_{wing,i}$ needs to be decomposed as $V_{a,wing,i}$ and $V_{t,wing,i}$ further added to the corresponding velocity term in Eq.3.2. Consequently the resultant aerodynamic forces that generated on each airfoil section should be modified as:

$$F_i = \rho(V_{\infty} + V_{prop,i} + V_{SRV,i} + V_{wing,i}) \times \Gamma_i \tag{3.14}$$

Thus the corresponding thrust F_t and normal forces F_n also needs to be modified based on Eq. 2.1 and 3.9, respectively. The next step is to construct the wing analysis module for these purposes and further couple it with SRV analysis tool.

3.2.3. WING ANALYSIS MODULE

In order to have an easy coupling with SRV analysis model and fast computation, potential flow based wing analysis tool is preferable. Consider the design tasks to be performed, two main requirements is raised for this model:

- Give acceptable prediction of wing performance under propeller and SRVs effects

- Provide accurate prediction of wing induced velocity at its vicinity

In order to achieve an accurate prediction of the propeller wing flow field, the restrictions of simplified approach like Vortex Lattice Method(VLM) become apparent: the absence of modeling the thickness effect of both the wing and nacelles [4]. In order to overcome this problem, one solution is to cover the actual surface of the wing with distributed singularities, which is referred to as the panel method [11]. Numerical implementations of panel methods for research and design purposes are presented in open literature [31, 33] and many studies [34, 35] have successfully incorporate propeller effects in the panel methods based wing analysis model.

In this study, the implementation of panel code is based on the open source 3D panel program developed by Daniel Filković [36]. The program was developed for calculating aerodynamic forces and moments acting on an aircraft in flight and it has been validated with commercial package FLUENT. Application of this code for current study is motivated by the convenience of easy coupling with SRV analysis module as it has been implemented in Matlab scripts. Considering the absence of certain functionalities, a series of tasks will be carried out:

- Implement the wing geometry in the panel code and set up the analysis routine
- Validation of the wing panel code by use of CFD results
- Incorporation of propeller and SRV effects in the wing analysis routine

For this reason, the basic formulation of this code is necessarily investigated with the purpose of finding out which part should be modified for propeller-SRV effects. In this section, the basic implementation of panel method is first introduced at 3.2.3, followed by the validation of the implemented panel code with Euler analysis at 3.2.4, the incorporation of propeller and SRV effects will be performed at 3.2.5.

BASIC FORMULATION

The problem to be solved is the Laplace equation defined as:

$$\nabla^2 \phi = 0 \tag{3.15}$$

Using Green's identity, we can construct the solution of Eq. 3.15 as follows: the solid boundary is discretized into a finite number of panels of finite area, as depicted in Fig. 3.10, on which a distribution of sources and doublets is placed.

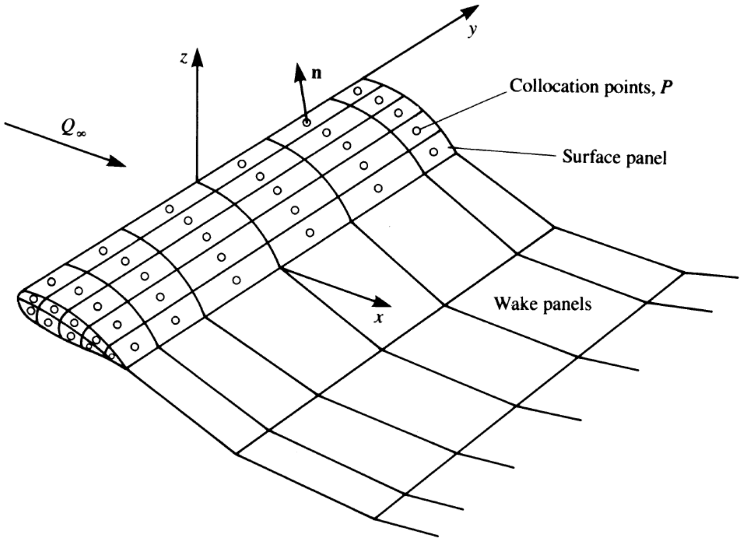

Figure 3.10: Approximation of the body surface by panel elements[11]

If the strength of sources and doublets is defined as σ and μ, the perturbation potential $\phi = \phi_{tot} - \phi_\infty$ will be formulated as:

$$\phi = \frac{1}{4\pi}\int_{S_B+S_W} \mu n \cdot \nabla(\frac{1}{r})dS - \frac{1}{4\pi}\int_{S_B} \sigma(\frac{1}{r})dS \tag{3.16}$$

where $\vec{n}$ is the vector normal to the panel, as denoted in Fig. 3.10, and ϕ_∞ is the free-stream potential.

BOUNDARY CONDITION

Eq. 3.16 can be solved by specifying a given set of boundary conditions. These boundary conditions should lead to a unique solution that exists and is physically relevant [4]. The boundary condition of zero normal velocity component on the surface S_B is expressed in Dirichlet problem which prescribes zero perturbation potential inside the body:

$$\frac{1}{4\pi}\int_{S_B} \mu n \cdot \nabla(\frac{1}{r})dS - \frac{1}{4\pi}\int_{S_B} \sigma(\frac{1}{r})dS = 0 \tag{3.17}$$

This lead to two unknowns to be solved, namely σ and μ , with only one equation. In order to have a uniquely defined solution, right combination of sources σ and doublets μ must be selected. Set up the source strength as:

$$\sigma = n \cdot V_\infty \tag{3.18}$$

This results in the only unknown of doublets strength μ. For non-lifting case, this combination of sources will take over most of normal flow on body surfaces, making strengths of dipoles less in value. This combination represents a certain numerical advantage [11].

For describing the flow over thick bodies without lift the source distribution was sufficient, but for the lifting cases the amount of circulation was not uniquely defined [11]. In order to solve this problem, a physical condition denoted as Kutta condition must be applied, which states that the flow should leave the lifting body's trailing edge smoothly. In practical, a wake model should be introduced and the value of wake potential jump μ_w is determined such that vorticity along the trailing edge is zero. Defining the doublets at upper and lower trailing edge as μ_u and μ_l, respectively, the wake doublet is obtained as:

$$\mu_w = \mu_u - \mu_l \tag{3.19}$$

Besides the wake strength, the shape and location of the wake also determines the solution. Physically wake doesn't exert any force on the fluid, which means no static pressure variation can occur through a wake. In practical it requires that the wake vortex sheet features parallelism between wake surface and local flow streamlines. In this study a fixed wake approach is applied which assumes the wake panels is aligned with freestream velocity. This approach is beneficial in terms of a fast computation and providing accurate prediction of wing performance at small angle of attack. However, in fact the wake experiences a roll up at wing tip and is distorted within propeller slipstream region, which can lead to deviated wing performance. These effects are neglected in the panel analysis and will be further corrected by high fidelity simulation result.

Once the surface singularities is determined, the velocity potential induced by wing ϕ can be computed by $V_{wing,i} = \nabla\phi$. The body surface pressure can be obtained through Bernoulli equation, and the pressure coefficient can be computed by:

$$C_p = 1 - \frac{(V_\infty + V_{wing,i})^2}{(V_\infty)^2} \tag{3.20}$$

Then the aerodynamic force on the panel can be computed as:

$$\Delta F_i = -C_{p,i} q \Delta S_i \cdot \vec{n}_i \tag{3.21}$$

$$F_N = \sum_{i=1}^{n} \Delta F_i \cdot \vec{N} \tag{3.22}$$

$$L = F_N cos(\alpha) \tag{3.23}$$

$$C_l = \frac{L}{qS_w} \tag{3.24}$$

where q is dynamic pressure calculated by $q = \frac{1}{2}\rho V_\infty^2$, S_i is the local panel area and $\vec{n}_i$ is the local normal vector of each panel, $\vec{N}$ denotes the normal vector of the wing reference surface and α is the wing angle of attack.

The above mentioned approach is actually the Near Field method for aerodynamic force calculation since it is based on the pressure integration over the surfaces. This method is proved to give accurate prediction of wing lift, but fails to give acceptable results of the induced drag term. It is pointed out in study [37] that pressure integration has been proven a poor method of determining induced drag, exhibiting planform-dependent errors. This means the capture of leading-edge stagnation point is crucial for obtaining an accurate induced drag, which is unrealistic for wing at different angle of attack. A more robust method is to use the far field approach like Trefftz Plane Analysis.

Trefftz Plane Analysis

Trefftz Plane Analysis (TPA) is based a series of theorems: Munk's Theorems, Biot-Savart Law and the Kutta-Joukowski Theorem. Use were made of Munk's first theorem to lump the chordwise distribution of vorticity into a single load and to translate all loads into the Trefftz Plane [38]. The basic equation for calculating the wing induced drag can be derived by applying the Kutta-Joukowski Theorem in the drag direction. By use of Munk's Theorems, the calculations can be performed in the Trefftz Plane rather than the real plane. The equation for induced drag calculation is:

$$D_i = \frac{1}{2V_\infty}\oint V \cdot N n d l \tag{3.25}$$

The circulation integral is taken around the perimeter at the Trefftz Plane that projected by the lifting system. n is a unit vector normal to the load perimeter. V_i is the induced velocity in Trefftz Plane calculated from the vortex model of the lifting surface by use of Biot-Savart Law. Once obtaining V_i, the induced drag can be determined. The implementation of TPA in current study is based on the work developed by Blackwell [38]. This method uses a vortex lattice representation of the aircraft lifting surfaces coupled with the classic theorems for induced drag calculation. The implementation together with the adaptation for propeller and SRVs effects will be introduced later in Sec. 3.2.5.

3.2.4. Validation Of Wing Analysis Module

A convergence study has been performed to make sure panel results is converged. Fig. 3.11 presents the refined mesh of the wing model, which was used for validation of the implemented panel code.

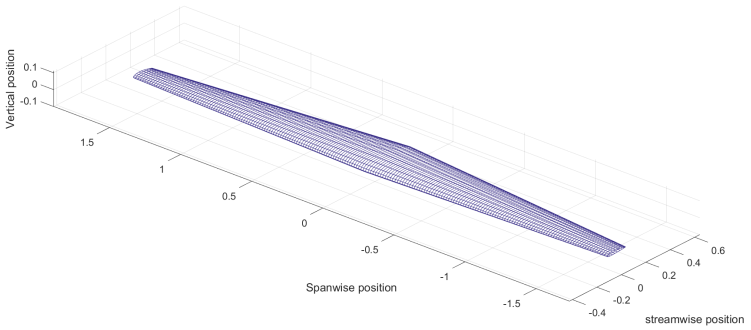

Figure 3.11: Wing panel mesh

In order to fully validate the panel, a series of panel and Euler simulations are performed on the wing model with only freestream velocity at two different angle of attacks. The comparison of C_L and C_P are delivered at the figures below, where the left column contains the result at $\alpha = 1.55°$, while the right column contains the results obtained at $\alpha = 4.45°$. It can be seen that the C_L distributions are almost identical for both cases at any condition. C_P distribution is compared at three spanwise positions of 20%, 50% and 80%. Only slightly difference is observed at leading edge part where panel tends to overestimate the suction pick. Anyway, these two methods match well over most of the surface.

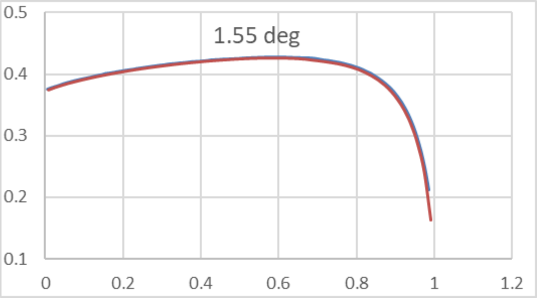

Figure 3.12: Comparison of C_L at AoA=1.55

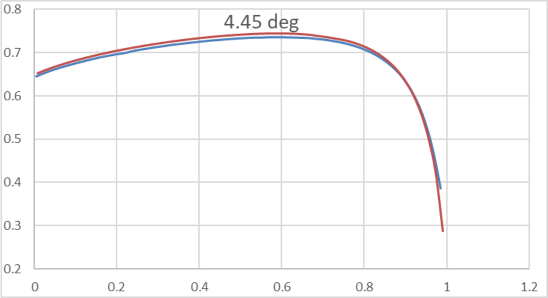

Figure 3.13: Comparison of C_L at AoA=4.45

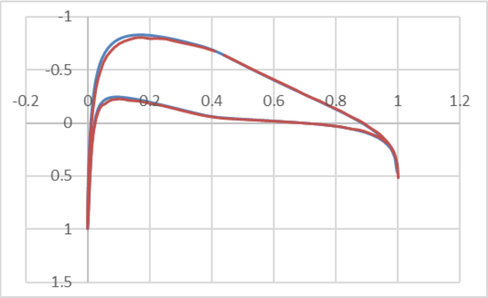

Figure 3.14: Comparison of C_p at 20% wingspan at AoA=1.55

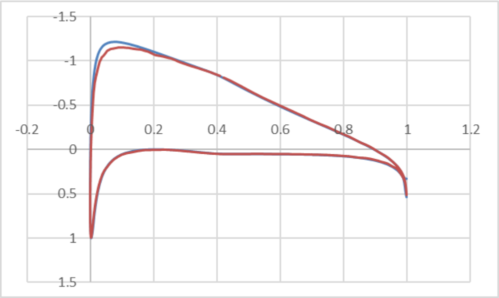

Figure 3.15: Comparison of C_p at 20% wingspan at AoA=4.45

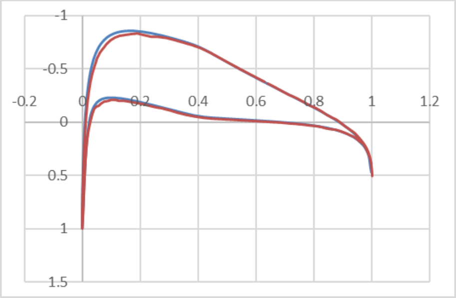

Figure 3.16: Comparison of C_p at 50% wingspan at AoA=1.55

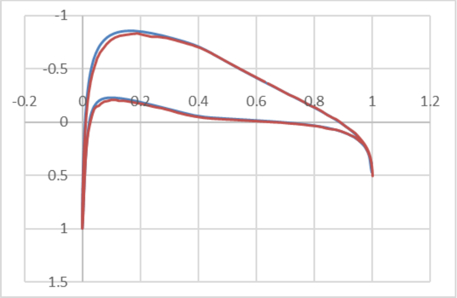

Figure 3.17: Comparison of C_p at 50% wingspan at AoA=4.45

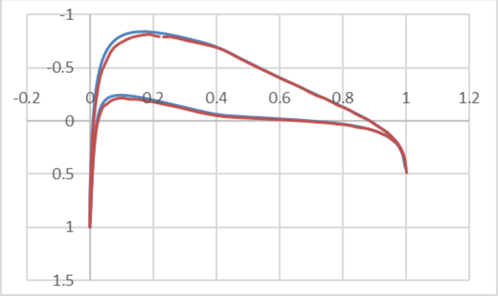

Figure 3.18: Comparison of C_p at 80% wingspan at AoA=1.55

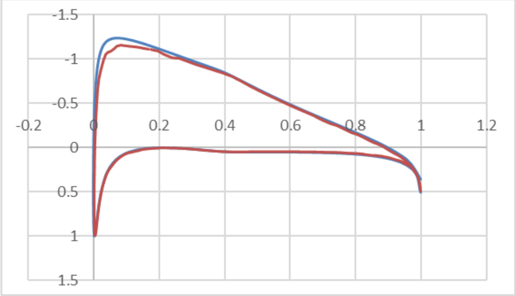

Figure 3.19: Comparison of C_p at 80% wingspan at AoA=4.45

Validation of Trefftz Plane Analysis Module

The next step is to validate Trefftz Plane Analysis(TPA) module, for this purpose the total induced drag C_{Di} and induced drag distribution C_{di} of a clean wing is considered, which means no propeller effects is present. Since no experiment or CFD data is available for induced drag, the simulation result will be compared with a theoretical result. From 3D wing theory it is known that a wing with minimum induced drag features an elliptic loading distribution and the efficiency factor, defined as:

$$e = \frac{C_L^2}{\pi A C_{Di}} \tag{3.26}$$

should become 1. Consider the inputs to the TPA module includes wing planform geometry and spanwise loading distribution $\Gamma(y)$, and if we assume a wing geometry with an elliptic wing loading $\Gamma(y)$ and give it as input, the analysis module should output an induced drag C_{Di} which equals to the theoretical minimum induced drag C_{Di}. As for the induced drag distribution C_{di} at this condition, an analytical approach will be presented: According to literature [11], an elliptic circulation distribution can be specified as:

$$\Gamma(y) = \Gamma_{\max}[1 - (\frac{y}{b/2})^2]^{1/2} \tag{3.27}$$

And the total C_L and C_{Di} can be derived as:

$$C_L = \frac{\pi}{2}\frac{b}{S}\frac{\Gamma_{\max}}{V_\infty} \tag{3.28}$$

$$C_{D_i} = \frac{1}{\pi}\frac{S}{b^2}C_L^2 \tag{3.29}$$

The downwash is constant along the span, which equals:

$$w_i = -\frac{\Gamma_{\max}}{2b} \tag{3.30}$$

The induced angle of attack is:

$$\alpha_i = \frac{\Gamma_{\max}}{2bV_\infty} \tag{3.31}$$

Then the induced drag distribution can be evaluated as:

$$D_i = \rho V_\infty \alpha_i \Gamma(y) = \rho\frac{\Gamma_{\max}^2}{2b}[1 - (\frac{y}{b/2})^2]^{1/2} \tag{3.32}$$

The induced drag coefficient distribution is thereby reached:

$$C_{d_i}(y) = \frac{\Gamma_{\max}^2}{V_\infty^2 bc(y)}[1 - (\frac{y}{b/2})^2]^{1/2} = \frac{4C_L^2 S^2}{\pi^2 b^3 c(y)}[1 - (\frac{y}{b/2})^2]^{1/2} \tag{3.33}$$

Hereby the theoretical $C_d i$ distribution for minimum induced drag is obtained. It's noted from Eq. 3.33 that the $C_{di}(y)$ is dependent on local chord distribution $c(y)$. If we assume the chord distribution $c(y)$ has an elliptic form, which is defined as:

$$c(y) = c_{root}[1 - (\frac{y}{b/2})^2]^{1/2} \tag{3.34}$$

then the $C_{di}(y)$ will become a constant value:

$$C_{d_i}(y) = \frac{\Gamma_{\max}^2}{V_\infty^2 bc_{root}} = \frac{4C_L^2 S^2}{\pi^2 b^3 c_{root}} \tag{3.35}$$

For validation purpose, the APROPOS model used by Veldhuis [4] is taken as an example, and the propeller-off case at $C_L = 0.4$ is specified. This layout of model is depicted in Fig. 3.20. To test the accuracy of this method, total C_{Di} is plotted with respect to refined spanwise mesh size, as can be seen in Fig. 3.21:

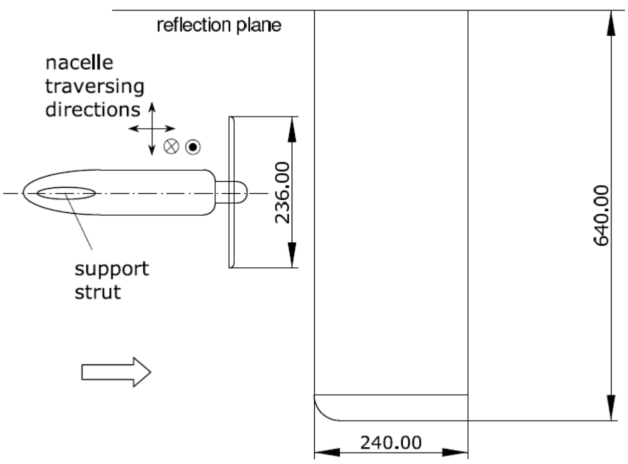

Figure 3.20: Dimensions of the APROPOS model (in mm).[4]

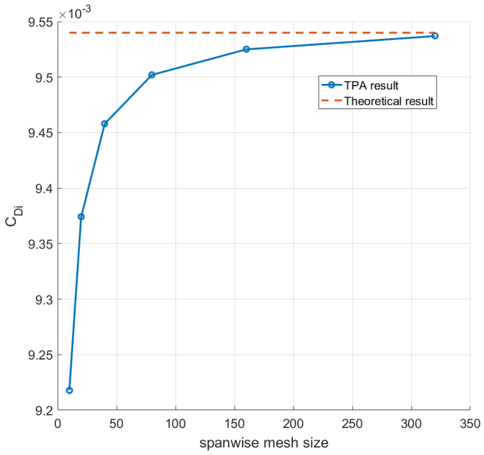

Figure 3.21: Convergence of wing spanwise mesh for induced drag calculation

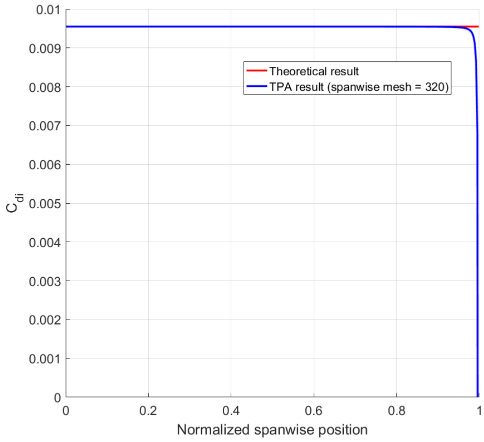

Figure 3.22: Comparison of C_{di} distribution for elliptic chord distribution

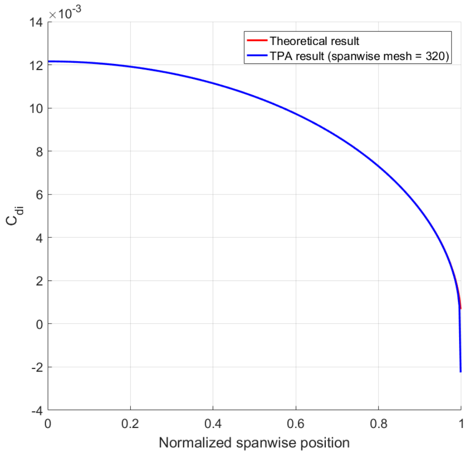

Figure 3.23: Comparison of C_{di} distribution for constant chord distribution

A convergence trend is observed for total C_{Di} when the spanwise mesh is refined, and the converged result is close to the theoretical $C_{Di} = 0.00954$. As for the validation of C_{di} distribution, the results calculated based on an elliptic chord distribution and also a constant chord distribution are compared, the results are depicted in as depicted in Fig. 3.22 and 3.23, respectively. It can be seen that both results match well at most of the span except for the wingtip region at Fig. 3.22 where a sudden drop occurs. This might caused by the numerical singularity resulted from an infinite small chord length at wingtip. The problem no longer exists when a constant $c(y)$ is assumed, and due to the constant chord distribution, an elliptic C_{di} is obtained for both methods, as depicted in Fig. 3.23. As a conclusion, the implemented Trefftz Plane Analysis is fully validated with a clean wing case, whereas the adaptation for propeller and SRV effects will be introduced in next section.

VALIDATION OF WING INDUCED VELOCITY

As already discussed at the beginning og this section that one major requirement for wing analysis module is to provide accurate wing induced velocity at it's vicinity. For this purpose, the wing induced velocity should be validated. In current study this is achieved by comparison with a Euler simulation performed by Li et al.[9].

The velocity comparison is made at a series of sample points arranged in both vertical and spanwise direction at a plane halfway in between propeller and wing, as is depicted in Fig. 3.24

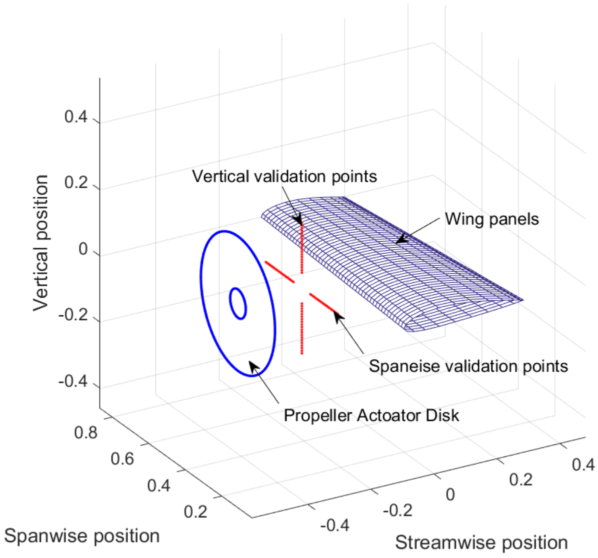

Figure 3.24: Configurations for wing induced velocity validation

As already discussed in Sec. 3.2.1 that the axial velocity V_a and tangential velocity V_t mainly determine SRV's performance, thereby the validation are performed on these two terms. This is achieved by comparing velocity obtained from panel with Euler simulation, where panel results contains the wing induced velocity and the propeller induced velocity from the "add on" slipstream and RANS simulation performed on the same setup. The results are presented in Fig. 3.25, where first row reports the comparison of velocity distribution at vertical validation points while the second row presents the corresponding results at spanwise positions. In each row, the left figure presents the comparison of V_a, whereas the right figure depicts the comparison of V_t. It can be observed that all the velocity components match pretty well at all sample points, with only slightly difference caused by the errors of wing loading distribution.

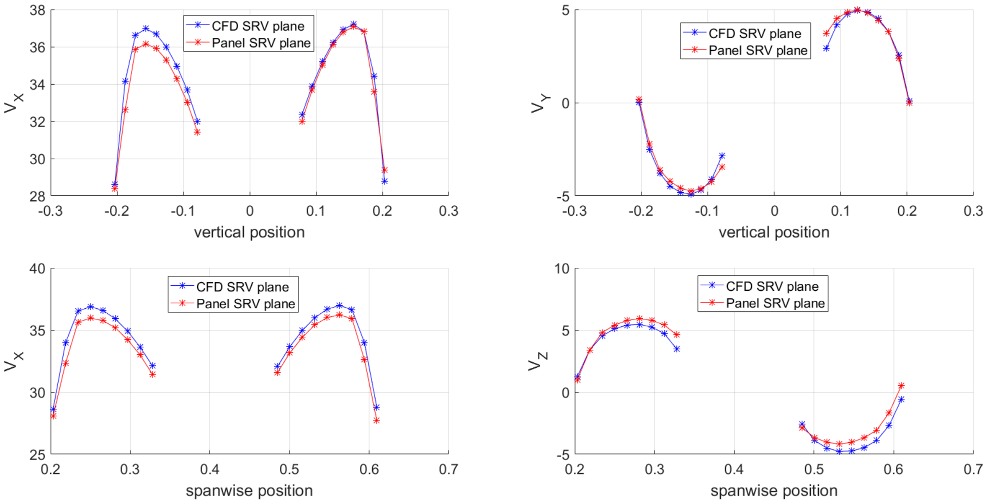

Figure 3.25: Validation of wing induced velocity at SRV plane

3.2.5. ADAPTATION OF WING ANALYSIS MODULE FOR PROPELLER AND SRV INDUCED VELOCITY

This section will focus on adaptation of wing analysis module for propeller and SRV effects. For now the wing and SRV model has been separately constructed, first attempt to couple these two models is to put them together in the flow domain, as is depicted in Fig. 3.26. For better illustration, a 4-blade SRV arrangement is shown where each vane features flexible azimuthal positions. The problem at issue is to predict wing performance with installed propeller and SRVs, which means the C_L and C_{Di} should be correctly calculated with added velocities induced by propeller and SRVs.

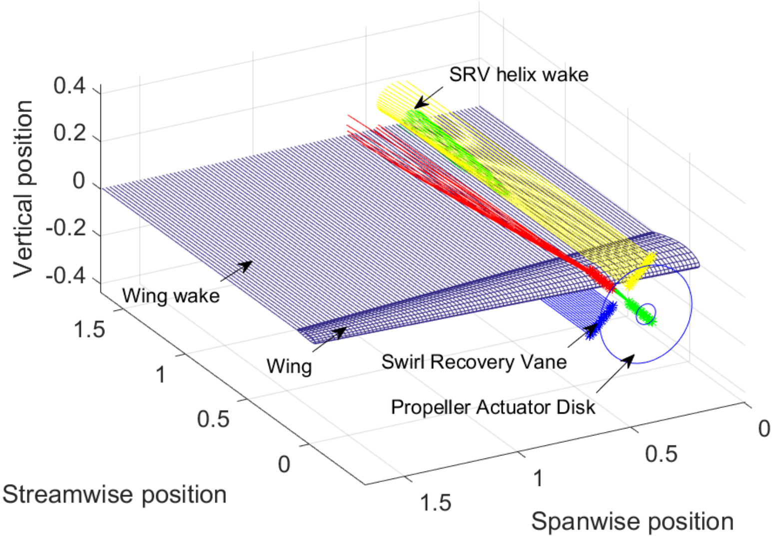

Figure 3.26: Incorporated Propeller-SRV-wing analysis model

As pointed out by Veldhuis [4], the propeller slipstream effect can be included by adapting the boundary condition of wing analysis taking the slipstream velocity into account. In practical, it is achieved by incorporating the presumed slipstream model into the panel code. The velocities $V_{prop,i}$ in slipstream are extrapolated to the panel collocation points.

The SRV effects on wing can be modeled by including SRV induced velocity $V_{SRV,i}$ on the wing surface panels. The $V_{SRV,i}$ can be calculated by evaluating the SRV vortex system by use of Biot-Savart Law.

The velocity on the panels now includes the propeller and SRV induced velocities:

$$V_i = V_\infty + V_{prop,i} + V_{SRV,i} \tag{3.36}$$

The source strength is then modified to:

$$\sigma = n \cdot (V_\infty + V_{prop,i} + V_{SRV,i}) \tag{3.37}$$

In order to have a unique solution of both σ and μ, the following equation system is formed:

$$a \cdot \mu + b \cdot \sigma = 0 \tag{3.38}$$

where a denotes influence coefficients matrix of doublet and b is the matrix for source. Since the right side of Eq. 3.38 are known values, they can be multiplied into right hand side vector C_{RHS}:

$$a \cdot \mu = -C_{RHS} \tag{3.39}$$

it follows:

$$\mu = a^{-1} \cdot C_{RHS} \tag{3.40}$$

It is realized that the modified boundary condition leads to a change of both μ and σ. Thereby the perturbation potential induced by wing ϕ is also changed. This will finally lead to changes of wing induced velocity which can be calculated by $V_{wing,i} = \nabla\phi$. As a consequence, the pressure coefficient is modified as:

$$C_p = 1 - \frac{(V_\infty + V_{wing,i} + V_{prop,i} + V_{SRV,i})^2}{(V_\infty + V_{prop,i} + V_{SRV,i})^2} \tag{3.41}$$

And the aerodynamic force on the panel is computed as:

$$\Delta F_i = -C_{p,i} q \Delta S_i \cdot \vec{n}_i \tag{3.42}$$

where dynamic pressure q is modified as:

$$q = \frac{1}{2}\rho(V_{\infty,i} + V_{prop,i} + V_{SRV,i})^2 \tag{3.43}$$

The L and C_l can be computed with Eq. 3.23 and 3.24, respectively.

Adaptation of Induced Drag Calculation for Propeller-SRV Induced Velocity

As for the calculation of wing induced drag due to SRV and propeller effects, a more complicated adaptation is performed on the classic Trefftz Plane Analysis. To provide a better understanding, the adaptation will be introduced based on the propeller-SRV-wing configuration depicted in Fig. 3.26. The problem is to obtain a systematic induced drag, including the individual drag term from propeller, SRV and wing. The various sources for the systematic induced drag is reported in Table 3.2 below. Given that in the current low-fidelity analysis the propeller performance is constant, thereby only the induced drag on SRV and wing will be considered. The forces on SRVs is calculated in the lifting line (LL)model where the wing and propeller induced velocity basically lead to a negative induced drag, namely a thrust term. Thereby only the wing induced drag needs to be considered by current TPA module.

	$V_{prop,i}$	$V_{SRV,i}$	$V_{wing,i}$	Analysis tool
Propeller Induced drag	-	-	-	Euler
SRV Induced drag(Thrust)	√	√	√	LL
Wing Induced drag	√	√	√	TPA

Table 3.2: The sources of induced drag for a propeller-SRV-wing combination

As stated in Table 3.2, the sources of wing induced drag includes:

- Drag due to wing induced velocity on wing;
- Drag due to propeller induced velocity on wing;
- Drag due to SRV induced velocity on wing;

By definition, the induced drag is the force on the wing due to the tilting of inflow caused by the lifting surfaces. TPA manages to calculate this term at a plane located at far downstream of wing instead of on wing boundary. As can be seen in Fig. 3.27, the wing vortex model is projected at the Trefftz Plane, a series of load perimeter is formed by the trailing vortex pair having a circulation of equal magnitude but of opposite rotation. For each load perimeter, an associated control point is located midway, on which the induced velocity by the lifting surfaces can be calculated. With installed SRVs, the trailing vortex pair of SRV is added to the vortex model. As an example of SRV induced velocity calculation, the $V_{SRV,i}$ at one wing control point can be calculated by summing up the velocities induced by all the SRV vortex pairs.

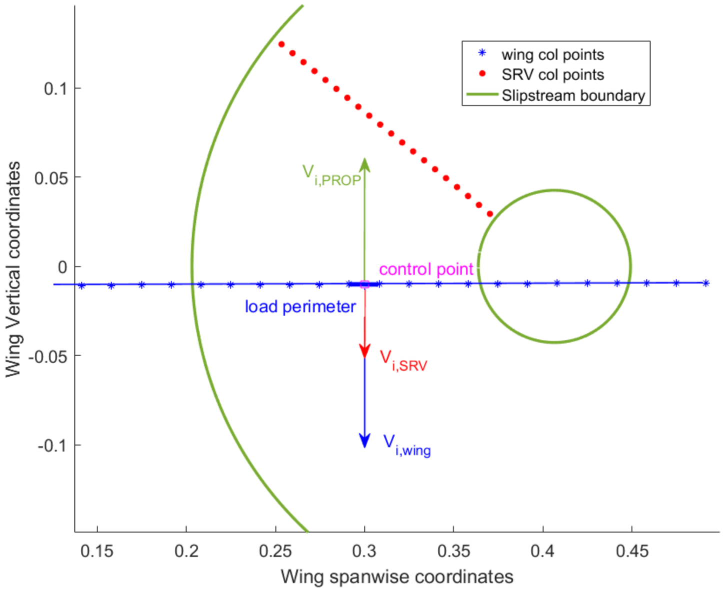

Figure 3.27: Projected vortex system and induced velocities in the Trefftz Plane.

For better understanding, the basic equation for induced drag calculation is re-formulated as:

$$D_i = \int \rho V_i \cdot n \times \Gamma_i dl = \sum_{i=1}^{m} \rho V_i \cdot n \times \Gamma_i s_i \tag{3.44}$$

where n is a unit vector that is normal to the load perimeter, Γ_i is the circulation of local lifting element, s_i is normalized semi-width of vortex pair ($s = 2dl/b$) and V_i represents the induced velocity at a control point $P(\infty, y_i, z_i)$. With the introduction of propeller and SRV, the induced velocity is modified as:

$$V_i = V_{wing,i} + V_{prop,i} + V_{SRV,i} \tag{3.45}$$

This means the total induced velocity consists of velocity induced by wing itself $V_{i,wing}$, velocity induced by propeller $V_{i,PROP}$ and that induced by SRV $V_{i,SRV}$.

The induced drag coefficient is defined as:

$$C_{Di} = \frac{D_i}{q \cdot C_{AV}} \tag{3.46}$$

Combination of Eq. 3.44, 3.45 and 3.46 yields the expression for total induced drag coefficient:

$$C_{Di} = 2\sum_{i=1}^{m} (\frac{\Gamma_i s_i}{V_\infty C_{AV}} \cdot (\frac{V_{wing,i} + V_{prop,i} + V_{SRV,i}) \cdot n}{V_\infty}) \tag{3.47}$$

Three terms can be distinguished from the right hand side of Eq. 3.47: Induced drag due to wing induced downwash:

$$C_{Di,wing} = 2\sum_{i=1}^{m} (\frac{\Gamma_i s_i}{V_\infty C_{AV}} \cdot \frac{V_{wing,i} \cdot n}{V_\infty}) \tag{3.48}$$

Induced drag due to propeller induced swirl:

$$C_{Di,prop} = 2\sum_{i=1}^{m}(\frac{\Gamma_i s_i}{V_\infty C_{AV}} \cdot \frac{V_{prop,i} \cdot n}{V_\infty}) \tag{3.49}$$

Induced drag coefficient due to SRV induced swirl:

$$C_{Di,SRV} = 2\sum_{i=1}^{m}(\frac{\Gamma_i s_i}{V_\infty C_{AV}} \cdot \frac{V_{SRV,i} \cdot n}{V_\infty}) \tag{3.50}$$

The $V_{prop,i}$ is interpolated from the slipstream velocity data, while $V_{wing,i}$ and $V_{SRV,i}$ are computed from wing and SRV lifting elements by use of Biot-Savart Law, respectively. Based on the work by Blackwell[38], the equations are given describing the induced velocity at a wing control point $P(x_i, y_i, z_i)$ due to one SRV tailing vortex pair located at $P(x_j, y_j, z_j)$:

$$V_{SRV,i} = v_i + w_i \tag{3.51}$$

$$v_i = -\frac{\Gamma_j}{2\pi}(\frac{z'}{R_1} - \frac{z'}{R_2}) \tag{3.52}$$

$$w_i = \frac{\Gamma_j}{2\pi}(\frac{y'-s'}{R_1} - \frac{y'+s'}{R_2}) \tag{3.53}$$

where

$$R_1 = (z')^2 + (y'-s')^2 \tag{3.54}$$

$$R_2 = (z')^2 + (y'+s')^2 \tag{3.55}$$

$$y' = (y_i - y_j)cos(\theta_j) + (z_i - z_j)sin(\theta_j) \tag{3.56}$$

$$z' = -(y_i - y_j)sin(\theta_j) + (z_i - z_j)cos(\theta_j) \tag{3.57}$$

3.3. HIGH-FIDELITY ANALYSIS MODULE

In the low-fidelity analysis as described above, a prescribed slipstream was used neglecting the upstream effects of SRV and wing on the propeller loading and the deformation of slipstream. As is already discussed, the negligence of such effects may lead to errors in performance prediction of propeller and wing. Current study applies surrogate-based multi-fidelity optimization algorithm where results from low fidelity model is corrected by high fidelity analysis on a propeller-SRV-wing configuration. In CFD based simulation, the interacted flow field can be fully predicted, which avoids the errors introduced by the slipstream modeling in potential based method. Considering the flow is inviscid in potential flow theory, an inviscid Euler solver is applied as the high-fidelity method to have a closer comparison and correction of the potential results.

3.3.1. GOVERNING EQUATIONS

The equations describing time-dependent, adiabatic, compressible flow of an inviscid, non-heat-conducting fluid is described by the Euler equations [39]. This is built on the conservation of mass, momentum and energy for an inviscid flow. Hence it can correctly simulate flow fields with entropy and vorticity production due to total pressure, swirl and total temperature increase due to propeller power effects [4]. In integral conservation form these conservation equations using vector notation, take the following form. Conservation of mass:

$$\frac{\partial}{\partial_t}\iiint_V \rho dV + \iint_{\partial_V} \rho\vec{u}\cdot\vec{n} dS = 0 \tag{3.58}$$

Conservation of momentum:

$$\frac{\partial}{\partial_t}\iiint_V \rho\vec{u} dV + \iint_{\partial_V} \rho\vec{u}(\vec{u}\cdot\vec{n}) dS = -\int_{\partial_V} p\vec{n} dS \tag{3.59}$$

Conservation of energy:

$$\frac{\partial}{\partial_t}\iiint_V \rho E dV + \iint_{\partial_V} \rho E(\vec{u}\cdot\vec{n})dS = -\iint_{\partial_V} p\vec{u}\cdot\vec{n}dS \tag{3.60}$$

Here V is the control volume with its surface S and with $\vec{n}$ the local normal vector on S. The total energy E, for a calorically perfect gas is defined by:

$$E = \frac{p}{(\gamma-1)\rho} + \frac{1}{2}\vec{U}^2 \tag{3.61}$$

in which the velocity vector $\vec{U}$:

$$\vec{U} = (u, v, w)^T \tag{3.62}$$

Here u, v and w are the velocity components in respectively x, y and z directions. ρ is the density and p is the static pressure. This forms a closed system of equations that can be solved.

3.3.2. ACTUATOR DISK MODEL

Since the emphasis is not on the design of the propeller but on the time-averaged effects of the slipstream on the SRV and wing, the problem is simplified by approximating the propeller blades as an actuator disk, which has been applied by Veldhuis [4]. To have an accurate radial distribution of the axial and angular momentum in the slipstream, the thrust and torque obtained from the RANS simulation of the isolated propeller are given as an input in the Euler simulation. For the related work, readers can refer to the study performed by Li et al.[9].

3.3.3. WING CIRCULATION CALCULATION IN EULER ANALYSIS

The wing circulation distribution can be derived from Euler simulation, which is the main output of Euler analysis that will further be needed by surrogate model setup. The definition of circulation is given by Eq. 3.63.

$$\Gamma = -\oint_C V\cdot ds \tag{3.63}$$

The lifting section can be at any spanwise position of wing, and the velocity field can be derived from the Euler results. If the integral is taken at a series of spanwise positions along wing span, the circulation distribution of the wing can be obtained.

3.4. SURROGATE-BASED MULTI-FIDELITY OPTIMIZATION MODULE

The use of high fidelity methods coupled with optimization techniques seems to be feasible for wing and SRV design, however, consider that design optimization normally require a large number of simulations, direct optimization of wing and SRV based on this high-fidelity method is impractical. Computationally feasible design based on CFD simulations can be realized by surrogate-based optimization (SBO) technique [40, 41]. A surrogate model can be built using approximation functions such as polynomial regression [40]and kriging [42]. However, this method typically require large amount of training data to build an accurate surrogate model. In current study, the surrogate model will be built by use of a physics-based low-fidelity model. Current study constructs surrogate model by correcting simulation results from low-fidelity model with that from high-fidelity model. By use of SBO technique, the optimization burden is shifted to the low-cost surrogate model, whereas the high-fidelity model is referenced occasionally for verification purposes and to obtain data necessary to update the surrogates [9]. Typically this method only requires a single high-fidelity model evaluation per algorithm iteration, which makes the optimization process more efficient [12].

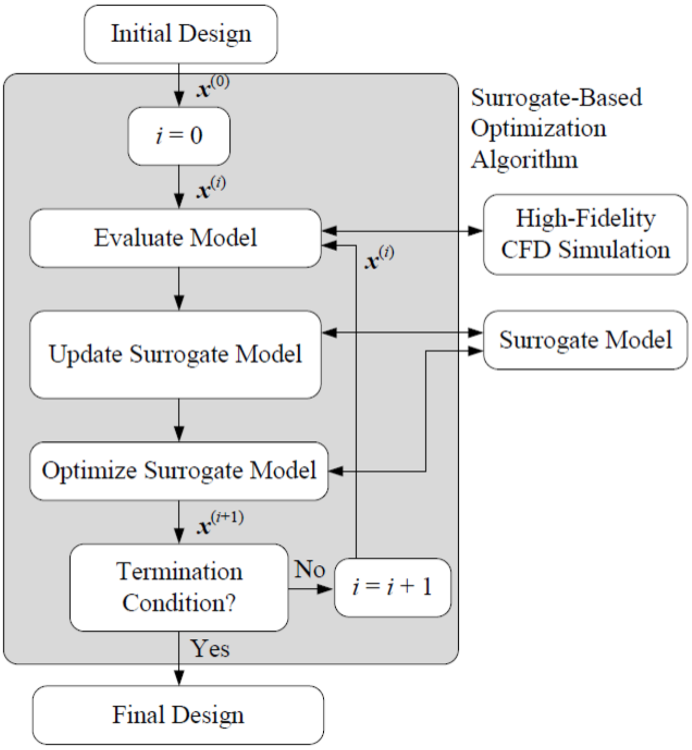

Figure 3.28: A flowchart of the surrogate-based optimization algorithm[12]

The correction method to be applied in this study is the shape-preserving response prediction (SPRP) technique [12, 43, 44]. The implementation of SPRP procedure will be introduced at the next step.

3.4.1. SURROGATE MODELING USING SHAPE-PRESERVING RESPONSE PREDICTION(SPRP)

This study adopts a shape-preserving response correction (SPRP) methodology as introduced in [45, 46]. This method is easy to implement and does not require derivative informations of high-fidelity model [43]. First issue is to select parameters for constructing the surrogate model. Normally the correction is applied to figures of interests in the optimization, i.e. the objectives and constraints. However, in the case of wing optimization, the figures of interests such as C_L(constraint)and C_{Di}(objective) are scalars for a given condition and design vectors, which results in non-uniqueness of any alignment procedure. Hereby, the model alignment is performed using intermediate simulation results, the circulation distribution Γ and lift coefficient distribution C_l. The advantage is that their dimensionality can be made large enough by selecting sufficient number of control points along wing span. As the wing C_{Di} and C_L are uniquely determined by Γ distributions, alignment of the corresponding distributions for the low- and high-fidelity models will result in an (unique) alignment of the figures of interest [12]. The SPRP model is formulated here by correcting wing Γ, while the formulation for wing lift distribution C_l follows the same way. We denote the circulation distributions from the panel and Euler method as Γ_P and Γ_E, respectively. The surrogate model is constructed assuming that the changes of Γ_E due to the adjustments of design variables can be predicted by changes of Γ_P. In order to simplify the problem, this study only considers the vertical variation of Γ are considered in the correction process assuming the spanwise deviation is negligible. This will be explained as follows: The design variable at issue is the local twist distribution at control points, the change of which is actually adjustments of local angle of attack at the control points, which mainly lead to a local variation of Γ_P that exhibited as a vertical shift in the Fig. 3.29. Moreover, as can be seen that difference between Γ_E and Γ_P is approximately a vertical shift as well and the characteristic points of local minimum/maximum and the inflection point are located at the same spanwise position. In this respect, the translation vectors are created to connect control points that are actually Y vectors. Due to the assumption that changes of Γ_P can be predicted by that of Γ_E, these two values can be directly linked by these translation factors, as is depicted in Fig. 3.29.

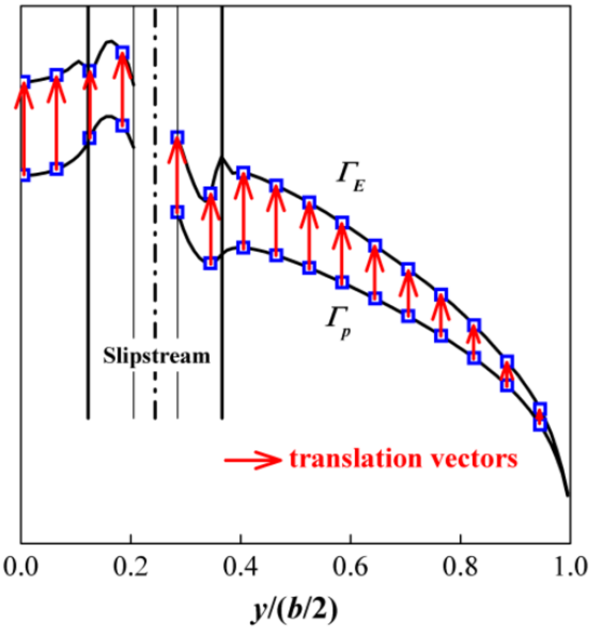

Figure 3.29: Correction of wing circulation distribution by shape-preserving response prediction methodology.[9]

The translation vectors is kept as constants during each iteration of the optimization algorithm and the surrogate objectives Γ_S are formed by the summation of Γ_P and the translation vectors. The "quality" of surrogate model can be estimated by comparing Γ_S with Γ_E for a new geometry results from optimization. And an iterative process is applied to update the surrogate model until a stopping criteria is fulfilled. The optimization framework will be constructed for solving specific optimization problem, which will be introduced later.

3.4.2. DIRECT ALGORITHM FOR GLOBAL OPTIMIZATION

The DIRECT optimization algorithm was first introduced by Jones et al.[47] as a modification to Lipschitz Optimization. It was proposed to solve global optimization problems with bound constraints and a scalar objective. It can be very useful when the objective function is a "black box" function or simulation [13]. In this respect, it is suitable for optimization of SRV azimuthal positions at issue as the response surface is unknown. Successful application of Direct in aerodynamic optimization can be found at [48–50]. The strengths of DIRECT lies in the balanced effort it gives to local and global searches, and the few parameters it requires to run [13]. Here some theories behind DIRECT algorithm will be introduced. For a more completed description, the reader is recommended to [47].

DIRECT is a sampling algorithm and does not need the gradient information of the objective function. It works by continuously subdivide domain into "boxes" and sample the center points for evaluation, then utilizes the obtained information to decide which direction to search. The main idea of DIRECT is to find all the potentially optimal "boxes" in the search space and then partition them [49]. First the definition of potentially optimal "boxes" will be provided and then the partition procedure will be introduced.

POTENTIALLY OPTIMAL HYPER-RECTANGLES

. Suppose the unit hypercube has been partitioned into hyper-rectangles. Let m_i denotes the center point of the ith hyper-rectangle and d_i the distance from the center point to the vertices. Let f_{min} be the current lowest function value and e be a positive constant. A hyper-rectangle j is said to be potentially optimal if there exists some rate-to-change constant $K > 0$ such that:

$$\begin{aligned} f(m_j) - Kd_j &\le f(m_i) - Kd_i \quad for \quad i = 1,2...,m \\ f(m_j) - Kd_j &\le f_{min} - e\, f_{min} \end{aligned} \tag{3.64}$$

PROCEDURE FOR DIVIDING RECTANGLES

First, the domain of design space is transformed into unit hyper-cube, then it is further subdivided into three hyper rectangles of equal size. The point at center of each rectangle is sampled and evaluated by the objective function. Then the algorithm subdivides dimension with the smallest function values into thirds, such that new hyper-cubes are formulated. In subsequent rounds of subdivision, a selection process is performed to identify potentially optimum hyper-rectangles, and only the selected rectangles can be subdivided. The selection is basically based on the function values $f(c_i)$ and size of rectangles. In this respect the algorithm features balanced effort for local and global searches. The termination occurs when maximum iterations or function evaluations is achieved.

An example of Direct loop is presented in Fig. 3.30 each row represents a single iteration during optimization. The transition from column 1 to 2 represents the selection process of the potentially optimal hyper-rectangles, and the identified rectangles are colored as yellow. Last column shows how the rectangles are subdivided.

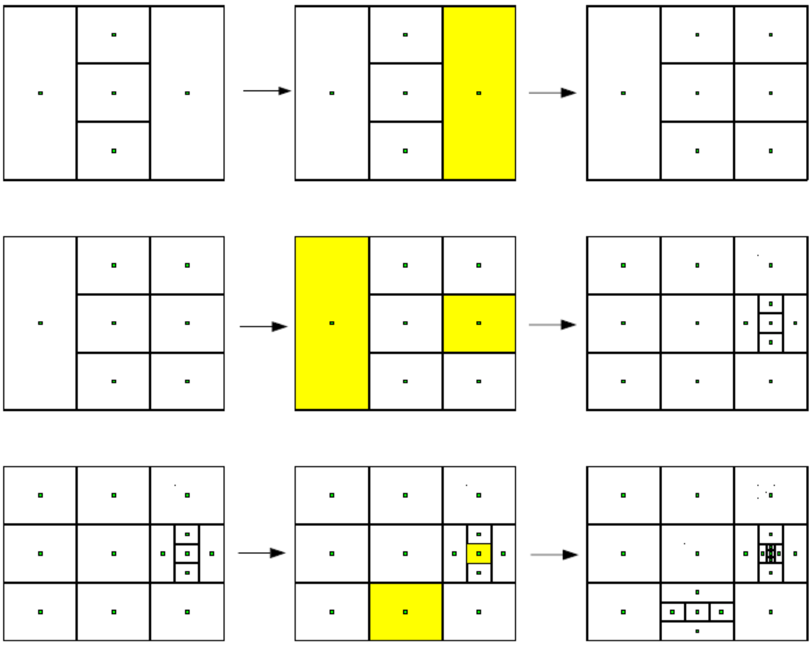

Figure 3.30: A series of iterations of Direct optimization[13]

IMPLEMENTATION

This study applies a implemented MATLAB version of DIRECT optimizer for easy coupling with the potential flow solver. The code is developed by Finkel. The User Guide of this function is referred as [13], and resource code can be referred to [51].

The structure of analysis and design framework that constructed in this chapter is presented in Fig. 3.31 below.

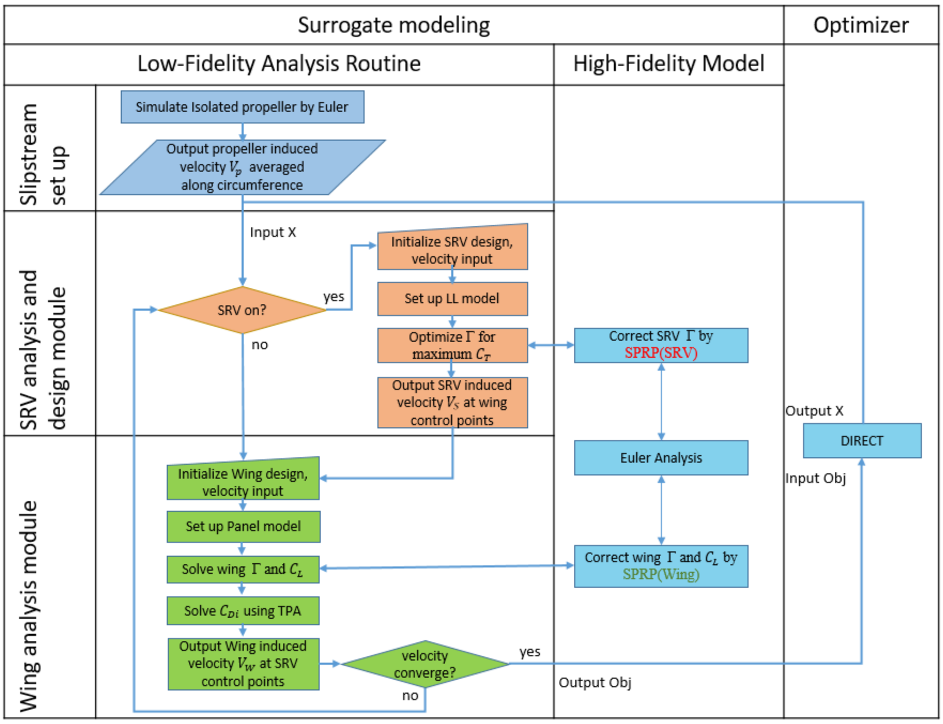

Figure 3.31: Structure of analysis and design framework

Chapter 3 mainly deal with the separate modules that utilized for construction of a surrogate-based multi-fidelity optimization framework. Chapter 4 will present the application of such strategy for a wing design case, while Chapter 5 will apply it on a series of SRV design cases.

4

OPTIMIZATION OF WING TWIST FOR MINIMUM INDUCED DRAG

Motivated by the system performance gain in terms of wing induced drag decrease from propeller-wing interaction, and considering the wing design itself can be optimized to maximize this performance gain, a study of wing optimization for minimum induced drag is carried out. First, the optimization problem will be defined at Sec. 4.1, then the construction of SBO framework will be presented in Sec. 4.2. The optimization results will be discussed in Sec. 4.3.

4.1. PROBLEM STATEMENT

The optimization problem is to minimize the wing induced drag C_{Di} while maintaining lift coefficient of $C_L = 0.5$. The SRV is not considered in this case, thus by performing such an optimization, the maximum thrust-drag performance in terms of only wing induced drag reduction can be achieved.

$$\begin{aligned} min \quad & C_{Di}(X) \\ subject\ to \quad & C_L = constant \\ where \quad & X = (x_1, x_2, ..., x_8) \end{aligned} \tag{4.1}$$

The optimization is performed based on a series of simplifications and assumptions:

- The propeller slipstream and performance is fixed during optimization, which assumes the adjustment of design variable has negligible effects on propeller.
- The viscous effects is not considered during optimization.
- The airfoil camber and chord length is kept constant during optimization while only the twist will be optimized.

The emphasis of current thesis is not on propeller design, but on the comparison of performance gain from propeller-wing and a propeller-SRV-wing configuration, thus the propeller geometry should be fixed in order to obtain a comparable result. As for neglecting the viscous effects during optimization, typically the total drag of wing, including both induced drag and viscous drag, should be minimized. As pointed out by Veldhuis in study [4] that viscous drag has limited effects on the optimized wing twist given fixed chord, whereas it does has considerable effects when the chord is varied. Thereby, the viscous drag is not considered in current case. The selection of design variables will be explained at next step.

4.1.1. DESIGN VARIABLES AND BOUNDS

The mechanism of how an integrated propeller-wing configuration can lead to reduction in wing induced drag has been discussed and the main conclusion is that a non-elliptic lift distribution will be found for minimum induced drag. To obtain such an optimal lift distribution, the adaptation of twist or camber distribution is usually applied. In this study, the twist distribution is optimized while keeping the local chord and airfoil shape as unchanged. In order to increase the optimization efficiency, the total number of variables should be kept as low as possible. The strategy is to describe wing twist by use of parametric curve function defined by a few control points. The curve function should be able to capture the local curve variations in the slipstream, and the control points should be carefully selected for this purpose. Finally the B-spline curve function is selected. B-spline allows the local control over the curve surface because each vertex affects the shape of a curve only over a range of parameter values where its associated basis function is nonzero. In this respect it is beneficial for predicting the local twist change during optimization. It is tested that 8 control points located at 8 spanwise locations, as shown in Fig. 4.1, is able to capture a pre-defined sine-shape wing twist that is normally featured by optimum wing twist distribution. The control points are correlated to the characteristic of slipstream and wing, for example, the wing root and tip and the slipstream boundaries. The upper and lower bounds of twist angle were set to 0 [°] and 8 [°], respectively, this is to make sure the range fully cover the extreme local twist angles during optimization.

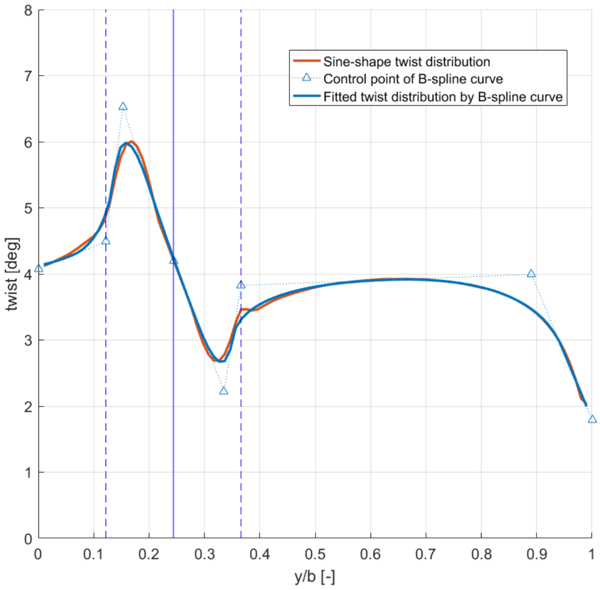

Figure 4.1: B-spline control points selection based on curve fitting

4.1.2. BASELINE DESIGN AND MESH INFORMATION

The baseline design is a wing-mounted tractor propeller configuration which has been provided in Fig. 3.1.1. It is assumed the position of propeller is fixed with respect to wing quarter chord line, and the wing angle of attack is tilted during optimization process to achieve the lift constraint. Furthermore, an inboard-up rotation is assumed and propeller is mounted at a negative (tilt down) angle with reference to the wing, this is suggested Veldhuis [4] as it will lead to reduction of overall wing induced drag. A grid convergence study was performed on the total C_L. The final choice for the wing panel mesh is presented in Fig. 4.2 and the properties is delivered in Table 4.1.

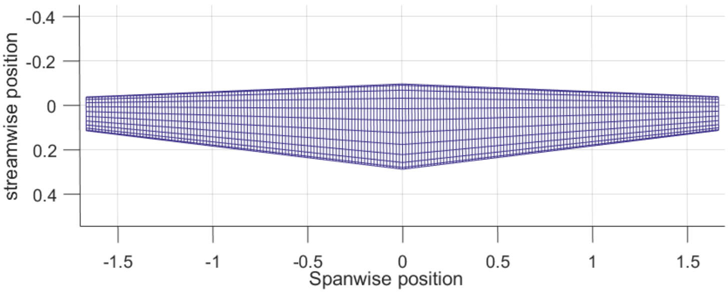

Figure 4.2: Wing mesh information

Direction	Number of panels	Spacing type
Span-wise	200	uniform
Chord-wise	23	cosine

Table 4.1: Wing mesh properties

4.2. Optimization Framework

In this section the surrogate-based multi-fidelity optimization framework will be constructed for solving the defined problem. The framework exploiting the SPRP-based surrogate model is presented in Fig. 4.3 below. It is actually a double-loop optimization procedure. The inner loop is driven by DIRECT to find optimum response of current surrogate model, while the outer loop is performed to update the surrogate model by use of the Low/High-Fidelity results of the inner loop optimum.

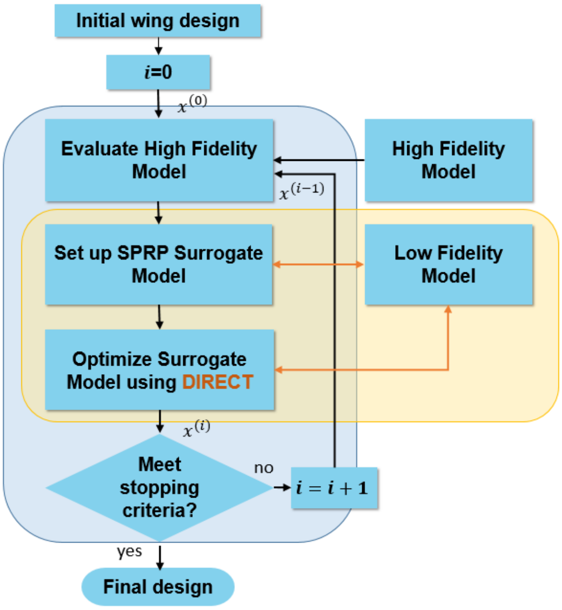

Figure 4.3: Surrogate-based multi-fidelity optimization framework for wing design

If we assume $x^{(i)}$ denotes a current design, then the initial design will be denoted as $x^{(0)}$ accordingly. The results from surrogate model, Low Fidelity Model and How Fidelity Model are denoted as Γ_S, Γ_P and Γ_E, respectively. For each iteration i, the surrogate model is re-built based on the optimum design from previous iteration by equation $\Gamma_S(x^{(i)}) = \Gamma_E(x^{(i)}) + f(x^{(i-1)})$, where $f(x(i-1))$ is the transition vectors calculated from $f(x^{(i-1)}) = \Gamma_E(x^{(i-1)}) - \Gamma_P(x^{(i-1)})$.

The stopping criteria for inner loop is that DIRECT algorithm is converged, which is to achieve a presumed maximum number of function evaluations. The outer loop will terminate when current update does not bring further improvement of the surrogate model response.

4.3. OPTIMIZATION RESULT

This section will present the optimization results. First the convergence history of SBO algorithm is presented, followed by an investigation of the design space exploration of the converged surrogate model by the DIRECT algorithm. At last, the optimized wing will be compared with the baseline wing in terms of wing twist distribution, wing Γ, C_l and C_{di}.

4.3.1. CONVERGENCE HISTORY

The stopping criteria for inner loop is specified as maximum function evaluations of 100 times 8 (the number of design variable), and for outer loop convergence, it is specified as $||C_{Di}(x^{(i+1)}) - C_{Di}(x^{(i)})|| < 0.2$ drag counts, corresponding to 1% of total C_{Di}. The convergence history of both inter and outer loops are presented in Fig. 4.4 and 4.5, where left figure provides convergence of the function objectives and right figure compares the optimum wing design of each surrogate model. As can be seen that three inner loops have been performed, which means three surrogate models were constructed, and the optimum C_{Di} for the last two surrogate models are almost identical. And it's observed from right figure that the last two optimum designs feature almost identical twist distribution, which confirms the convergence of surrogate model.

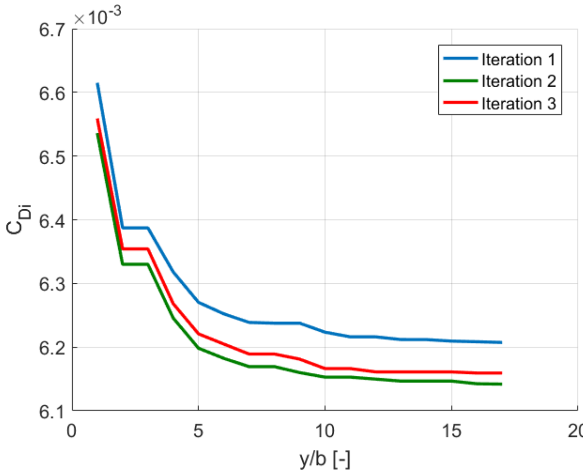

Figure 4.4: Convergence history of each iteration performed by DIRECT

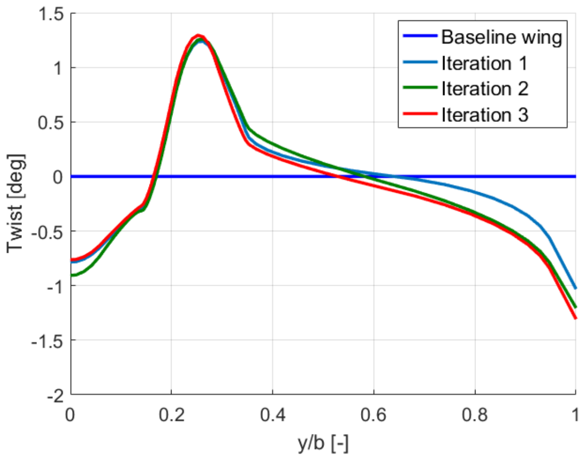

Figure 4.5: Comparison of optimum twist distribution for each iteration.

The quality of surrogate model can also be estimated by comparing the direct output, the C_l and Γ distribution, from the surrogate model with the corresponding results from High Fidelity model. The results are presented in Fig. 4.6, and 4.7. It can be seen that the results from surrogate model match well with Euler simulation for the optimum wing, which further confirms the convergence of optimization procedure.

In order to further understand the optimization procedure, the results of design space exploration performed by DIRECT algorithm is investigated. By balancing between global and local searches, the DIRECT algorithm successfully converge to global optimum, provided that the objective function is continuous. [51] The function values of evaluated sample points forms the response surface, which also gives the information of how optimization algorithm find the optimum. In this optimization process, the "true" response surfaces is approximated by surrogate models, and the error bar are reduced to an acceptable level by the updating process. For this reason the response surface from the latest surrogate model will be presented, where the responses are wing induced drag C_{Di} that obtained at the sampling points defined by local twist $X = [x_1, x_2 ... x_8]$ at the control points. For visualization of the response surface, the 9-dimensional design space (8 design vari-

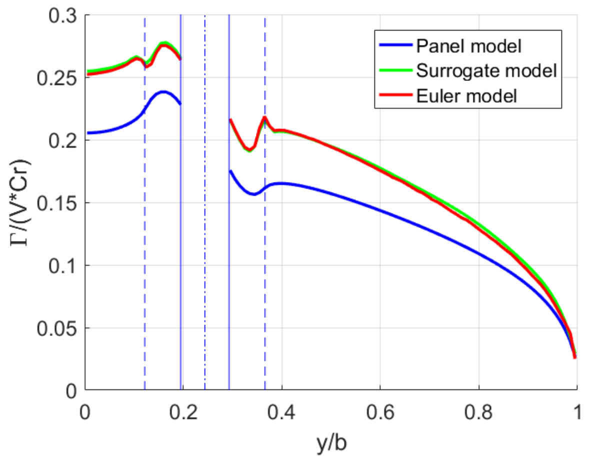

Figure 4.6: Comparison of Γ from panel analysis, surrogate model and Euler analysis

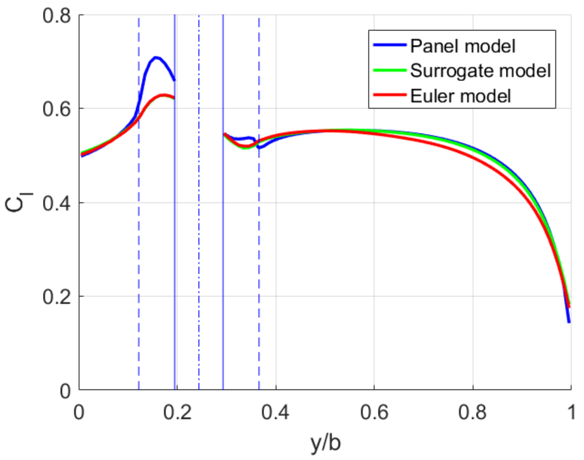

Figure 4.7: Comparison of C_l from panel analysis, surrogate model and Euler analysis

ables and 1 response) is simplified as multiple 3-d spaces, each consists of 2 design variables $X = [x_i, x_{i+1}]$ and one response C_{Di}. However, this might lead to overlapping responses at one specific sample points due to the fact that response value is non-uniquely dependent on the selected design variables. As a solution, only the minimum response value is collected and presented at one sample points. The resulted contour is depicted in Fig. 4.8. It can be seen the design space is fully explored and the twist variation appears to exhibit a single minimum.

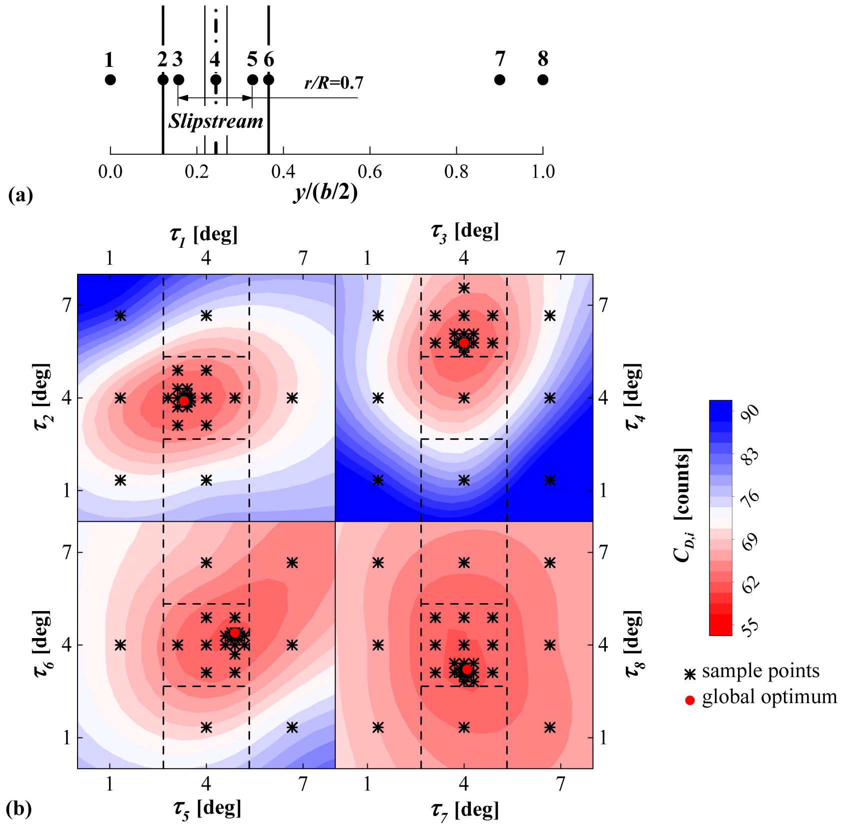

Figure 4.8: (a) spanwise locations of control points for B-spline curve construction; (b) design space exploration of wing twist optimization.[9]

4.3.2. DISCUSSION

The result of optimization is presented in Table 4.2. By comparing of the initial design and the optimum design from final loop, the total C_{Di} reduced by 3.92 drag counts, corresponding to 5.93% of total induced drag of the baseline wing and 1.4% of propeller thrust. In order to further understand the performance gain by optimization, comparison is made between the Γ, C_l and C_{di} between baseline wing and optimized wing.

Table 4.2: Comparison of wing performance between baseline wing and optimized wing

	C_L	C_{Di}	$\Delta(C_{Di})$	$\Delta(C_{Di})[\%]$
Baseline design	0.5	0.006607	-	-
Optimum design	0.5	0.006215	-3.92	-5.93%

First the wing twist distribution is compared in Fig. 4.9, as can be found that when compared with baseline wing, the optimized twist distribution features higher value at mid-part of wing and lower value at root and tip. Considering that higher twist means an increase of geometrical angle of attack, which will lead to an increase of lift. This indicates that the loading is allocated more to the mid-part of wing, such that less loading is carried by wing root and tip. This is supported by the C_l and Γ distribution as presented at Fig. 4.10 and 4.11, respectively. A few observations can be made from the results:

- A non-elliptic wing lift distribution is obtained for minimum induced drag for propeller on case, which has been proved by many studies.
- The changes in lift and circulation distribution follows the change in twist distribution. Twist decrease at inboard region leads to reduced local lift and circulation, while twist increase at slipstream region leads to an increase of lift and circulation at the same zone. Moreover, it's noted that the increase of circulation and lift after optimization is not limited within slipstream region, which also happens to the outboard region that close to slipstream.
- For the optimum wing, the outboard region that close to wing tip features less lift gradient as well as less lift compared to the baseline wing. Due to the fact that strength of trailing vortex is proportional to the lift gradient at the shed position, this change will lead to a tip vortex of less strength, which will further reduce wing induced drag.

It can be expected that, with the re-allocated loading distribution, performance gain is obtained of a lower induced drag for the same amount of lift. In order to get an idea of how the induced drag is decreased with such a lift distribution, the C_{di} distribution has to be investigated .

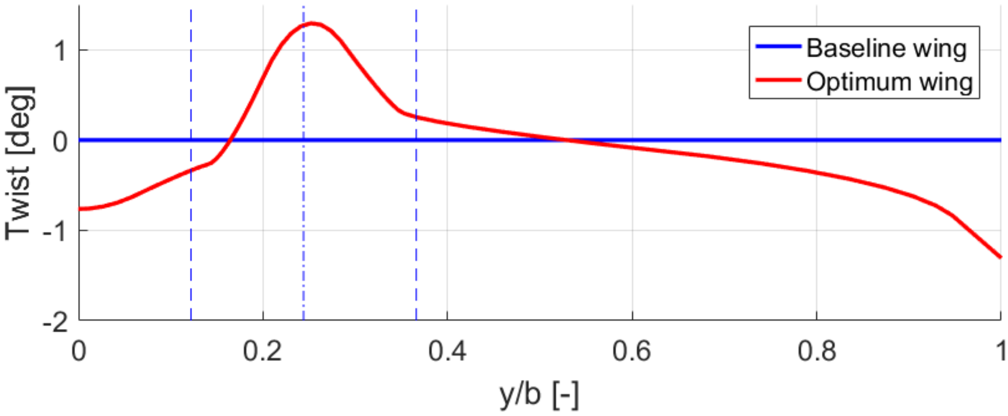

Figure 4.9: Comparison of twist distribution of baseline wing and optimum wing

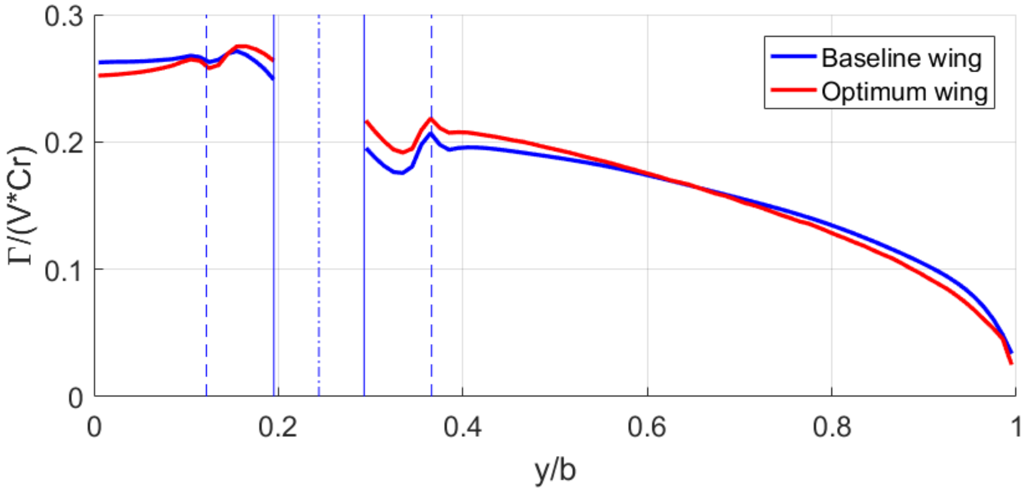

Figure 4.10: Comparison of circulation distribution of baseline wing and optimum wing

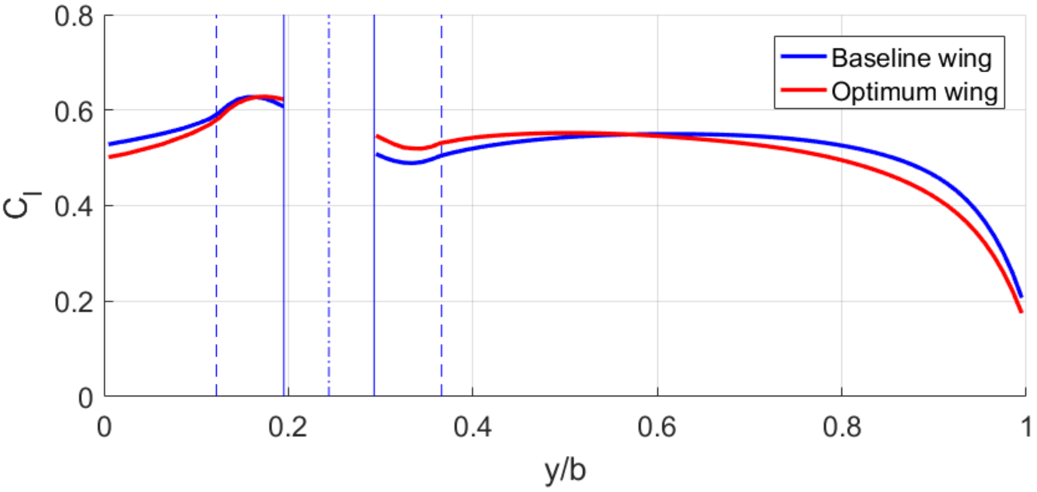

Figure 4.11: Comparison of lift distribution of baseline wing and optimum wing

As already discussed in Sec. 3.2.5, the total C_{Di} can be decomposed as induced drag due to wing self induced downwash($C_{Di,wing}$) and induced drag due to propeller swirl ($C_{Di,prop}$). These two terms can be calculated by use of equation 3.48 and 3.49, respectively. The de-composed induced drag distributions are illustrated here for better understanding. As can be seen in Fig. 4.12 that these terms features different pattern, which is due to the difference in wing and propeller induced velocity at the Trefftz Plane. This can be explained as follows: Based on the equations for C_{di} calculation, it is dependent on local wing Γ_i distribution and the local induced velocity that normal to the load perimeter at Trefftz Plane. The later term is denoted as $V_{wing,i} \cdot n$ and $V_{prop,i} \cdot n$ for these two terms, respectively. In TPA, the wing induced velocity can be approximated by $V_{wing,i} = \sum_{i=1}^{m} f(\Delta\Gamma_i, r)$, where $\Delta\Gamma_i$ is the local circulation change. This means the $C_{di,\Gamma}$ distribution is resulted from both magnitude and gradient of Γ distribution. As for propeller induced velocity at Trefftz Plane, it is plotted with along wing span at the control points of load perimeter, as is depicted in Fig. 4.13. It can be seen the normal velocity distribution features same pattern as propeller swirl profile, which is because for an horizontally distributed load perimeter, the normal direction of which is identical to direction of tangential velocity in slipstream. The inboard up rotating propeller induces an upwash at UBS, leading to a negative induced drag. And the DBS experiences a positive induced drag due to propeller induced downwash. Since the propeller induced velocity is only presented within slipstream, such that the rest part of wing experience a zero propeller induced drag. Due to the fact that UBS features a higher circulation compared with DBS, as a result the amount of induced drag decrease at UBS is larger than the increase at DBS, an overall effects is a reduction of total induced drag.

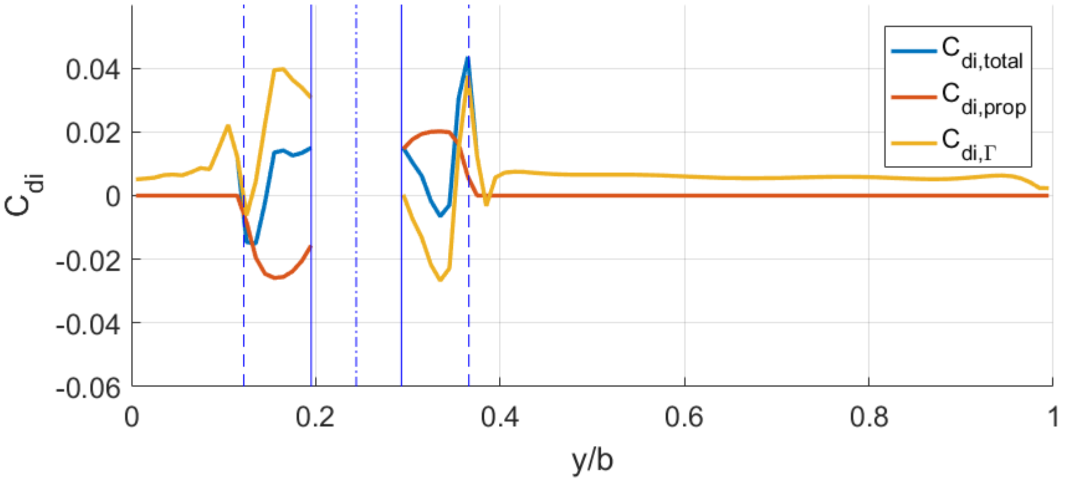

Figure 4.12: C_{di} distribution of optimized wing

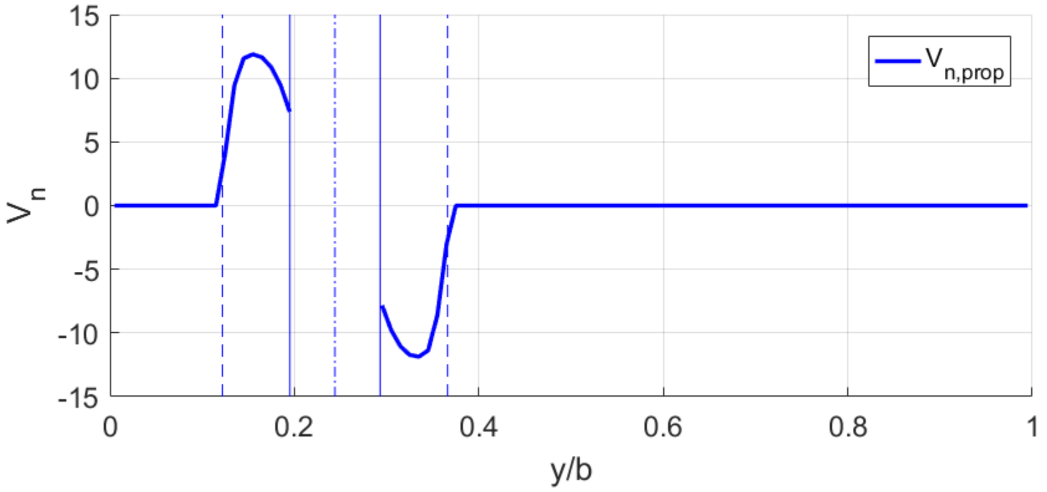

Figure 4.13: $V_{n,prop}$ distribution along load perimeter at Trefftz plane

In order to distinguish the induced drag reduction resulted from twist optimization, the individual C_{di} terms are compared between the baseline wing and optimized wing. First the wing loading induced drag $C_{di,\Gamma}$ is compared at Fig. 4.14, it can be seen that each term follows the corresponding wing Γ distribution depicted in Fig. 4.10. The propeller swirl induced drag $C_{di,prop}$ are compared at Fig. 4.15, it's observed that with optimized twist the magnitude of swirl induced drag is slightly amplified within the slipstream region. This is caused by the enhancement of Γ within slipstream. The comparison of total induced drag $C_{di,total}$ is presented at Fig. 4.16, which is sum of $C_{di,\Gamma}$ and $C_{di,prop}$. It seems that benefit is mainly gained at inboard and outboard region where the local induced drag is reduced. However, no qualitative conclusion can be drawn for the total induced drag change in slipstream region based on observation. A quantitative analysis of local lift and induced drag change has to be performed.

Hereby comparison is made of the change of integrated Di and L/Di for three sub-divided regions between the optimized wing and baseline wing. The results are presented in Table 4.3. The performance benefit is gained in both inboard/outboard region for lower Di, and the amount of Di decrease is higher than the Di increase at the slipstream region. This is because the slipstream region always features a higher L/Di compared with the rest regions, in this respect the optimization tends to allocate the lift to slipstream region such that the overall Di is reduced for the same amount of lift. As a result, the overall L/Di of the entire wing is increased.

		Inboard	Slipstream	Outboard	Total
Baseline wing	Di [drag counts]	15	12	39	66
	L/Di [-]	44.06	92.35	83.17	75.68
Optimized wing	Di [drag counts]	11	14	37	62
	L/Di [-]	58.61	85.65	85.38	80.45

Table 4.3: Comparison of integrated Di and L/Di at subdivided regions between baseline wing and optimized wing

As already explained, a wing trailing a propeller can be regarded as a stator vane, with only difference that the performance benefit is a reduction of wing induced drag. In this respect the quantity of induced drag reduction can be related to the amount of swirl being recovered. For this purpose flow field surveys were performed at two planes, in front of and behind the wing, and the in-plane swirl vectors are compared between the baseline wing and optimized, as depicted in Fig. 4.17, and 4.18, respectively. It can be seen that, for both cases, a swirl reduction is observed at UBS whereas a swirl enhancement is captured at DBS. This is mainly caused by the wing induced downwash effects, which will counteract the up-going flow at the UBS and enhance the down-going flow at the DBS. However, no significant difference can be observed for the amount of swirl been recovered in these two cases.

It seems that a wing trailing a tractor propeller will lead to a local enhanced swirl at DBS, which can't be reduced by wing twist optimization. It can be explained that the lift constraint leads to a non-negative local lift at any spanwise position, which will always induce a downwash at the downstream of wing, and this downwash will always enhance the swirl at DBS. This means the swirl recovery by wing is quite limited at this region, as a result the amount of wing induced drag reduction is also limited. It is expected that the residual swirl is a loss of energy which could be potential used for extra performance gain. The SRVs is to be introduced for this purpose, where extra thrust could be gained by use of the residual swirl. The related work will be introduced in next chapter.

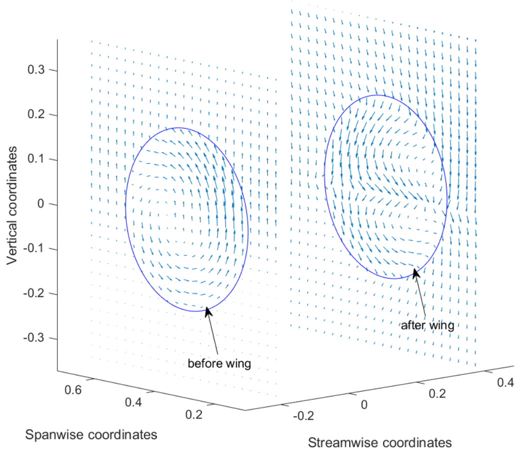

Figure 4.17: Comparison of in-plane velocity
at two survey planes that before and after the baseline wing

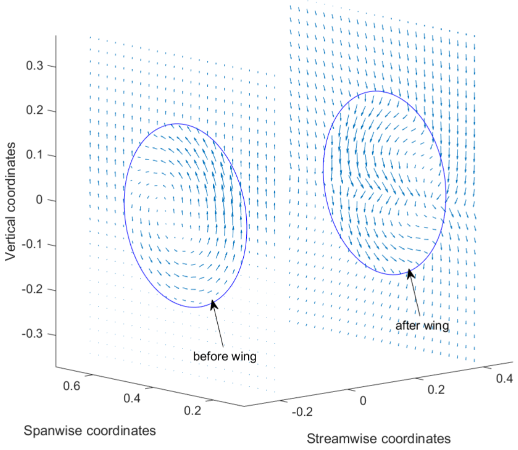

Figure 4.18: Comparison of in-plane velocity
at two survey planes that before and after the optimized wing

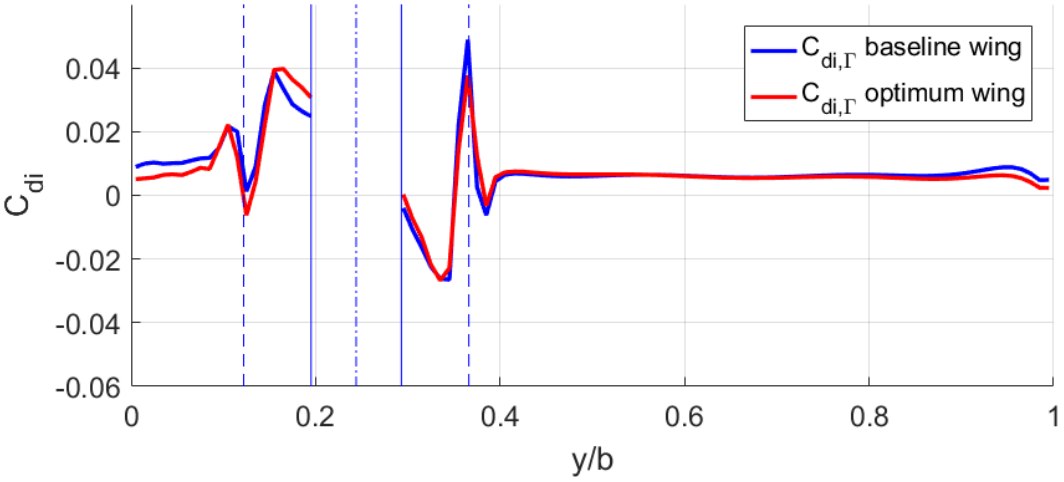

Figure 4.14: Comparison of $C_{di,\Gamma}$ between baseline wing and optimized wing

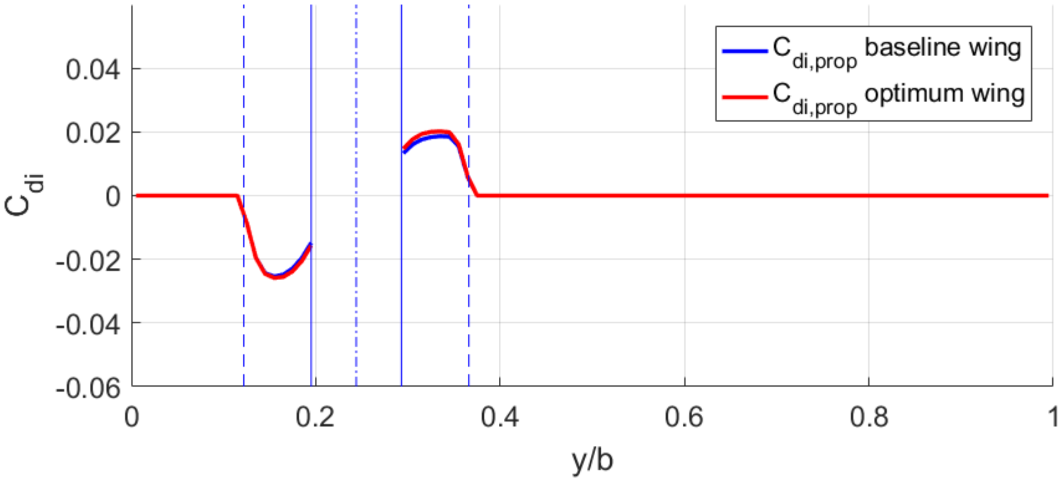

Figure 4.15: Comparison of $C_{di,prop}$ between baseline wing and optimized wing

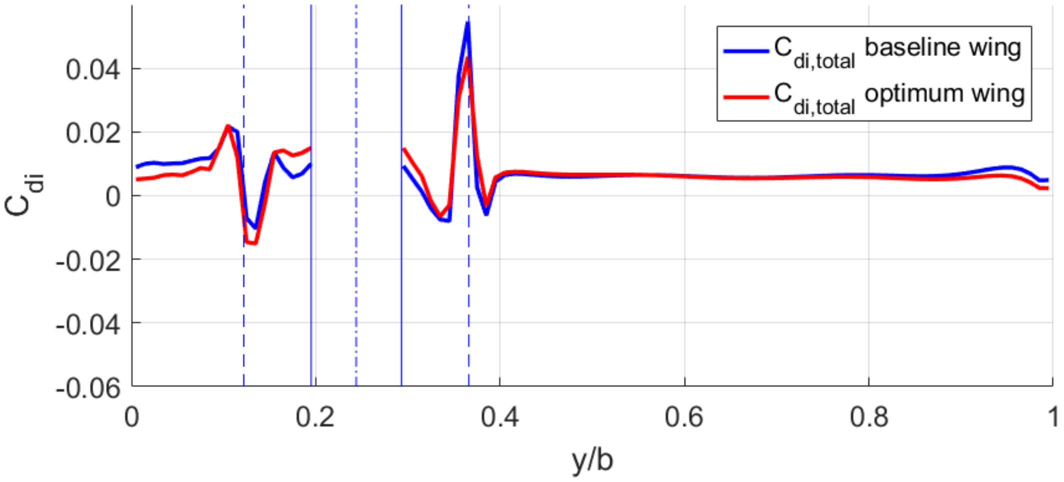

Figure 4.16: Comparison of $C_{di,total}$ between baseline wing and optimized wing

5

SRV DESIGN FOR WING-MOUNTED TRACTOR PROPELLER

According to Chapter 4, the swirl residual at wing vicinity gives the opportunity of introducing SRVs in a wing-mounted tractor propeller configuration, and it can be expected that extra benefit can be potentially gained by use of the swirl residual. Motivated by this discovery, this chapter will focus on design of SRVs for a wing mounted tractor propeller configuration. First a study on the effects of SRV positions on system performance will be performed at Sec. 5.1. Then the optimization problem will be defined at Sec. 5.2, followed by the construction of the surrogate optimization framework presented at Sec. 5.3. The results will be presented and discussed at Sec. 5.4.

5.1. EFFECTS OF SRV STREAMWISE AND AZIMUTHAL POSITION ON SYSTEM THRUST&DRAG BALANCE

SRV produces thrust by recovering swirl in the slipstream, thereby the amount of thrust it produces is related to the local incidence angle at each vane. In order maximize the thrust it produces, the SRV should be installed at the region where swirl is largest. According to the flow field survey in Fig. 4.18, it is known DBS after wing trailing edge features highest swirl, whereas the UBS before wing leading edge also features quite amount of swirl. In this respect, the SRV can be installed in either positions. It's realized that the relative position of SRV and wing affect the performance of each components. Thereby, before carrying out the optimization, a qualitative analysis of these effects will be discussed in this section.

In order to simplify the problem, a one-blade vane is installed parallel to wing at different positions. Both components are simplified as a single point vortex located at the corresponding quarter-chord line. Recapture the objective of current study, the discussion mainly focus on thrust-drag performance of the system.

When SRV is installed at UBS of wing upstream position, as can be seen in Fig. 5.1, it mainly experience a superimposed wing and propeller induced upwash, which will lead to inward pointed circulation at SRV bound vortex. This will lead to an augmented thrust term. SRV will in turn induces a downwash at its downstream position which is opposite to propeller induced upwash, in this respect the propeller induced swirl is recovered by the SRV. However, with the introduced downwash, an induced wing is generated on wing, this can be seen as a disadvantage effects that caused by the SRV. When SRV is moved to DBS of wing upstream, the propeller will induced a downwash in this case. Difference mainly occur at SRV where wing induced upwash will counteract propeller induced downwash. Due to the fact that wing usually induce a significant upwash, this would lead to reduced or totally removed swirl at SRV inflow, as can be observed in Fig. 4.17. Thereby, the thrust generated on SRV is significantly reduced which means the SRV lose its function. In this respect it's less interesting for installing vanes in this region.

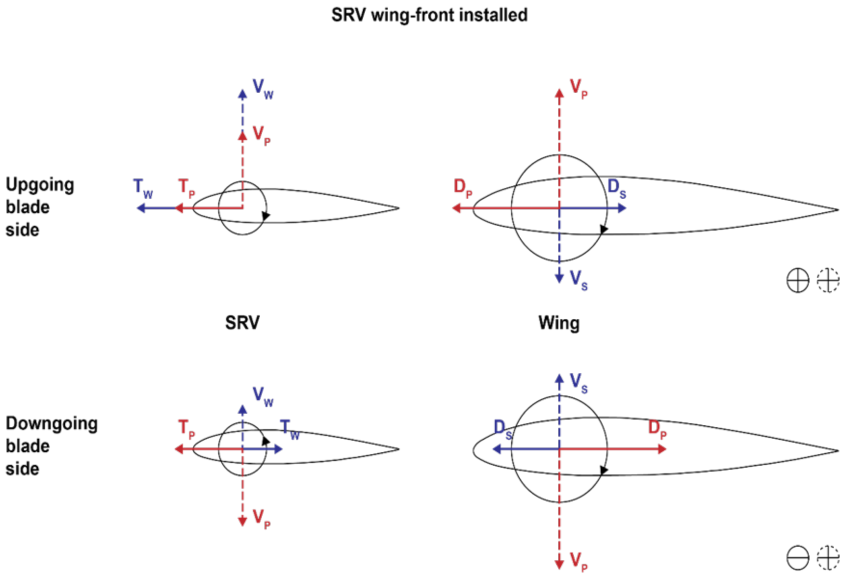

Figure 5.1: Force and Velocity diagram in a wing-front installed SRV configuration

When SRV is moved to downstream, since the vane only carries a small loading compared to wing, and considering no trailing vortex is presented at its upwash position, thus the upstream effects of vane on the wing is neglected. This is also based on the conclusions from previous study that the upstream effects of SRV on the performance of an upstream component is negligible. Thereby, it can be expected that the performance gain is mainly due to SRV produced thrust. It can be observed from Fig. 5.2 that the swirl is enhanced at DBS due to the augmented wing and propeller induced downwash, this will lead to an outward pointed circulation. As a result, a significant thrust term will be generated on SRV. As for the UBS trailing the wing, it's also less interesting for SRV design due to the fact that the swirl in slipstream is totally removed by wing downwash.

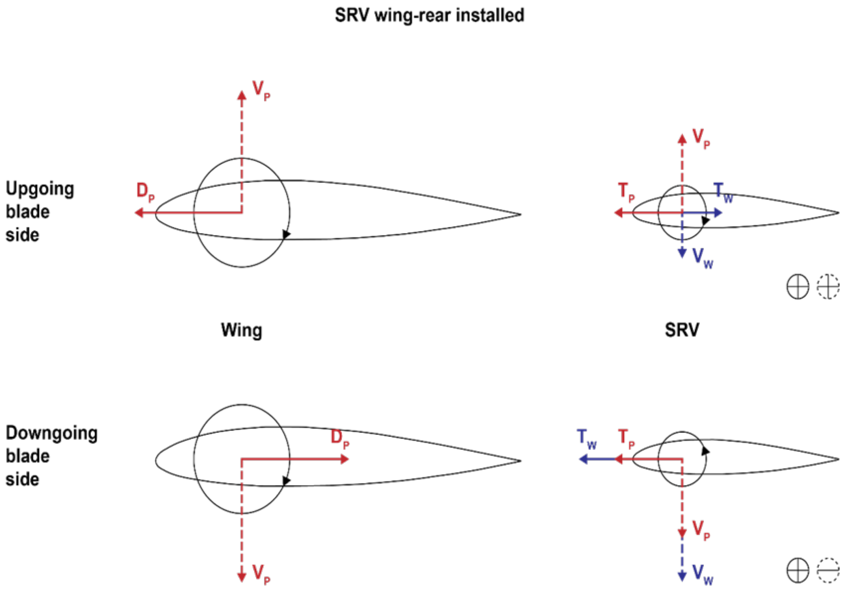

Figure 5.2: Force and Velocity diagram in a wing-rear installed SRV configuration

As a conclusion, the UBS at wing upstream and DBS at wing downstream is preferable for SRV design since a potential performance improvement in terms of SRV thrust production can be obtained. At next section, the optimization problem will be defined for carrying out the SRV design.

5.2. PROBLEM STATEMENT

To obtain a comparable quantitative results with respect to the analysis presented in Sec. 5.1, and further investigate the effects of axial and azimuthal positions of SRV on system performance, a serial of cases will be performed for SRV design:

- case 1: SRV design at UBS of wing upstream position
- case 2: SRV design at DBS of wing upstream position
- case 3: SRV design at UBS of wing downstream position
- case 4: SRV design at DBS of wing downstream position
- case 5: SRV design at a serial of streamwise positions at DBS of wing downstream position

The streamwise position of survey planes for SRV are depicted in Fig. 5.3.

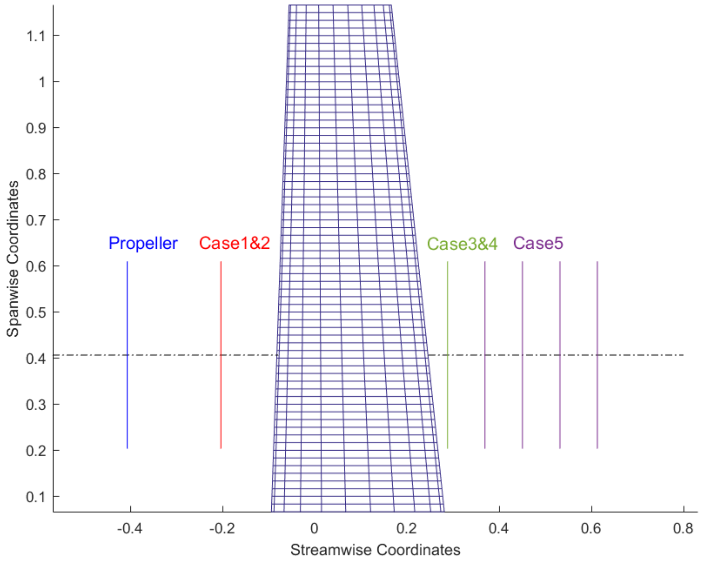

Figure 5.3: Streamwise positions of survey planes for SRV design in flow domain

A number of assumptions is necessarily presented for carrying out the optimization cases: The radius of SRV is assumed as the same with propeller radius to maximize its capability of recovering swirl. No quarter-chord sweep is applied for reducing the length of design vectors. The number of vanes is kept constant as 1 for all designs, which is to keep the configuration as simple as possible to better understand the physical effects.

In case 1 and 2, the streamwise position of vane is kept constant at half way in between propeller plane and wing quarter chord line. The position is selected to make sure the slipstream is fully developed such that the effects of static pressure gradient in the propeller slipstream on SRV thrust is negligible. It is also to avoid that SRV coincides with downstream wing, otherwise it may lead to unexpected wing performance deviation. It's noted that the streamwise position could also be selected as design variable since the wing upwash effects on SRV is reversely proportional to their relative distance, but not too much space is left for SRV in between propeller and wing. In case 3 and 4, however, due to the fact that no extra components are presented in this region, such that streamwise position can be varied here with enough flexibility. In this respect, case 5 will be performed where a serial of sub-cases will be performed at DBS of wing downstream for investigating the effects of streamwise position of SRV on the system performance.

5.2.1. Design Variables and Bounds

Based on the assumption that only a one-blade vane will be designed at each case, the design variable is selected as the azimuthal position ϕ of the one-blade vane for each case. The bound is defined with respect to specific design cases, as is denoted in Table 5.1 below. The design variable and bound are illustrated in Fig. 5.4.

Survey region	Design Case	Design variable	Lower bound	Upper bound
UBS	1&3	ϕ	π	2π
DBS	2&4&5	ϕ	0	π

Table 5.1: Design variable and bounds definition

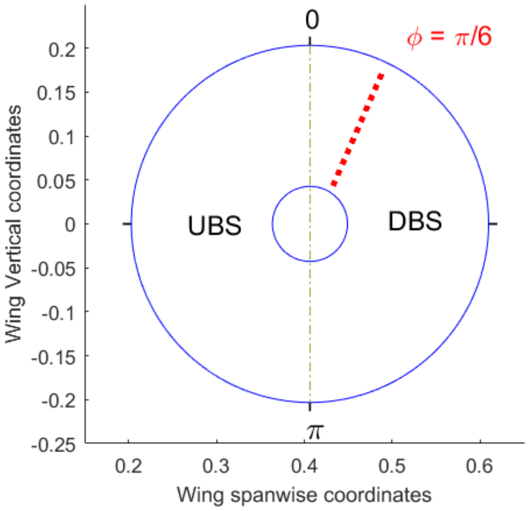

Figure 5.4: Design variable and bound definition

5.2.2. Design Objective and Constraint

Recapture the final objective is to maximize the system performance in terms of overall trust-drag behavior under the constraint of a constant overall lift. To reach this objective, the formulation of design objectives should account for all the relevant thrust and drag contributions. Besides, all the lift contributions should also be considered in the definition of lift constraints. It's noted that, the optimization should only considers the relevant forces that are sensitive to design variables. As for the rest forces, it is not neglected but assumed as un-changed, which means negligence of its sensitivity to design parameters [14].

According to previous studies [3, 7, 52], the presence of a trailing lifting body has negligible effects on a propeller's thrust in design operating conditions. This indicates that in a propeller-lifting body configuration measurable effects can be seen on the latter rather than on the propeller. In this respect, current optimization assumes a constant propeller performance and only considers the relevant forces that produced by SRV and wing during optimization.

For the estimation of wing performance, it mainly refer to a lift and drag term. From previous discussion it is known the induced drag change is non-negligible due to the propeller and SRV induced velocity. As for the viscous drag term, it is not neglected but assumed as un-changed, which means negligence of its sensitivity to design parameters. Such that for wing performance estimation, only the induced drag change will be considered during optimization. For the estimation of SRV performance, it can be seen as a lifting surface which is much smaller compared to size of wing. Thereby, in addition to extra thrust generated on vane, it also produces a lift term. And the following study will prove this term has non-negligible effects on the system lift. As a conclusion, the thrust and lift produced by vane should be considered during optimization. Finally the design objective can be formulated as:

$$\begin{aligned} min \quad & -C_{T,SRV}(\phi)+C_{Di,wing}(\phi) \\ subject\ to \quad & C_{L,wing}+C_{L,SRV}=0.5 \end{aligned} \tag{5.1}$$

To obtain a comparable result, the SRV T and L of is normalized by wing reference area S_w and dynamic pressure q, just as wing performance parameter. In this respect the SRV thrust coefficient $C_{T,SRV}$ and lift coefficient is defined by Eq. 5.2 and 5.3, respectively.

$$C_{T,SRV}=\frac{T_{SRV}}{qS_w} \tag{5.2}$$

$$C_{L,SRV}=\frac{L_{SRV}}{qS_w} \tag{5.3}$$

5.3. OPTIMIZATION FRAMEWORK

This section will introduce the surrogate-based multi-fidelity optimization framework for SRV design. As is presented in Fig. 5.5, the framework is similar to the wing optimization framework in Fig. 4.3 as introduced in Sec. 4.2, with only difference that another SPRP surrogate model is added for SRV Γ correction. As for the reason for correcting SRV Γ, it's noted that SRV mainly interact with downstream wing by tilting the velocity distribution in slipstream, and based on potential flow theory, it mainly relate to the strength and pattern of trailing vorticies. As a consequence, the surrogate model is applied for correction of the circulation distribution. In this respect, both the wing and SRV surrogate models should be updated during optimization. The low fidelity model is referred to the LL-Panel model as constructed in Chapter 3, while the high fidelity model is the Euler analysis of a Propeller-SRV-Wing configuration.

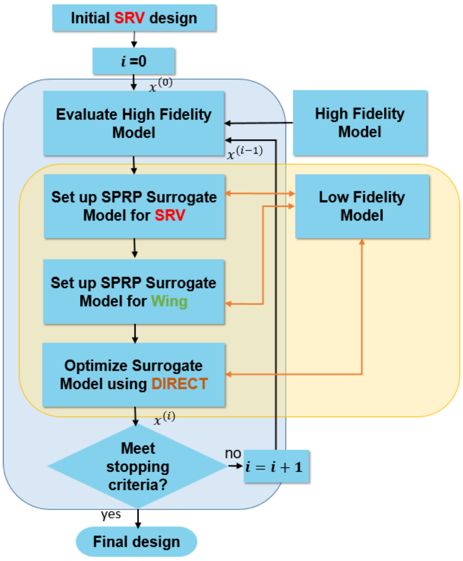

Figure 5.5: Surrogate-based multi-fidelity optimization framework for SRV design

5.4. OPTIMIZATION RESULT

5.4.1. CASE 1&2: SRV DESIGN AT A WING UPSTREAM PLANE

This section provides the optimization results of Case 1. The resultq of Case 2 is not provided since the performance gain is small. First the design space exploration of SRV and wing performance with respect to vane azimuthal position will be discussed, while the parameters describing overall and individual performance of SRV and wing will be separately presented. Then the performance of optimum SRV under isolated and installed condition will be compared to show the wing effects on SRV performance, and the wing performance with and without installation of SRV will be presented to demonstrate how SRV affect wing performance.

DESIGN SPACE EXPLORATION

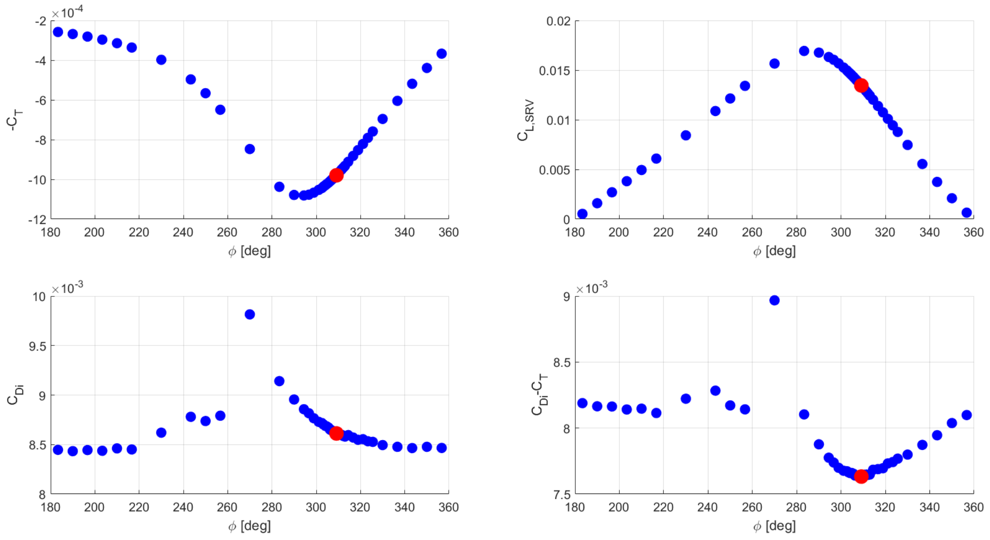

Figure 5.6: SRV and wing performance with respect to different SRV azimuthal positions

It can be seen from Fig. 5.6 that the design space of SRV azimuthal position is thoroughly explored by DIRECT, where first row presents the performance change of SRV, and the second row contains results of wing induced drag and the overall performance $C_{Di} - C_T$ variation. From the first row it's observed the stator generates higher loading when moving towards wing plane, and the highest thrust is obtained at $\Phi = 290°$. However, the optimization finally converge to another position of $\Phi = 309°$, where a slightly lower thrust is obtained. This is caused by wing induced drag variation, since a significant drag improvement is presented when stator approaches high thrust location, such that a compromise is reached with a relative high thrust of SRV and a lower wing induced drag. Moreover, the wing induced drag contributes more to the objective as $|\Delta C_{Di}|$ is almost twice of $|\Delta C_T|$. Another observation is that SRV can produce up to 3% of system lift, and due to the lift constraint the wing lift drops by the same amount. Based on approximation that wing C_{Di} is proportional to C_L^2, this can lead to about 6% of wing induced drag reduction. In this respect the lift produced by SRV is non-neglected.

OVERALL PERFORMANCE GAIN BY SRV DESIGN

In order to distinguish the performance gain by SRV design, comparison is made of system performance between optimum design (baseline wing with SRV on) and initial design (baseline wing only) under the same propeller slipstream with the constraint of $C_{L,wing} + C_{L,SRV} = 0.5$. The results is presented in Table 5.2. An unexpected result is found that the overall system drag increased by 15.5%. As can be observed that even though SRV can produce a thrust which is equivalent to 9.8 drag counts, meanwhile it also causes an increase of wing induced drag by 20.3 drag counts, consequently an overall increase of 10.3 drag counts is finally reached. It seems the wing performance is significantly deteriorated due to the upstream installed SRV, since a much higher induced drag is achieved with lower lift. In order to further explain the result, performance of SRV and wing is separately investigated with focus on how the SRV causes wing induced drag increase.

Table 5.2: Comparison of performance of baseline wing and baseline wing with optimum SRV

	Configuration	C_L	C_{Di}	C_T	$-C_T + C_{Di}$	$\Delta(-C_T + C_{Di})$	$\Delta(-C_T + C_{Di})[\%]$
Baseline	Wing	0.5	0.006607	-	0.006607	-	-
Optimum	Wing	0.4863	0.008612	-	0.007633	0.001026	15.52%
	SRV	0.01345	-	0.000980			

OPTIMUM SRV DESIGN

The azimuthal position and circulation distribution of the optimum SRV is presented in Fig. 5.7 and 5.8, respectively. It is also observed a contour is provided, which contains the surface distribution of tangential velocity in the survey plane. As can be seen the vane didn't converge to the region with largest swirl, instead it finally converged to $\Phi = 309°$ where the swirl is relatively high, which is consistent with the observations in the design space exploration as presented in 5.4.1. As for the circulation profile, it first increases until reaching highest value at $0.55R$, then drops to almost 0 at tip. The optimum circulation distribution is calculated by Newton method for maximum thrust, then it is realized by airfoil design module based on Xfoil [32]. It's noted that when optimizing the vane thrust the airfoil design is not necessarily performed since the lifting line model is competent for dealing with interaction effects, however, once the optimum azimuthal position is obtained, the airfoil design should be applied to form a full geometry such that the Euler simulation can be further performed for constructing surrogate model. The surrogate model is converged after a few iterations. Observe Fig. 5.8 that the converged surrogate model very well predict the circulation distribution obtained from an high fidelity result.

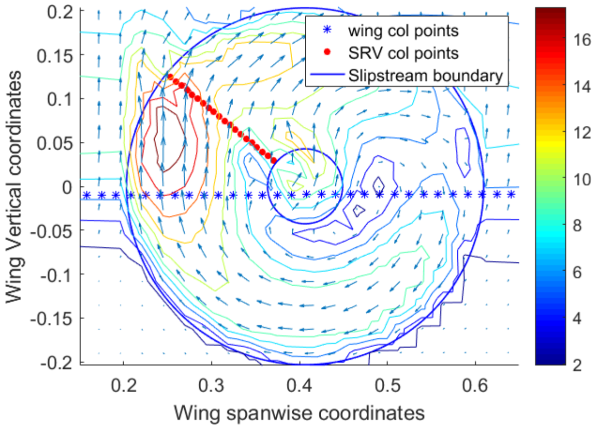

Figure 5.7: Azimuthal position of optimum SRV

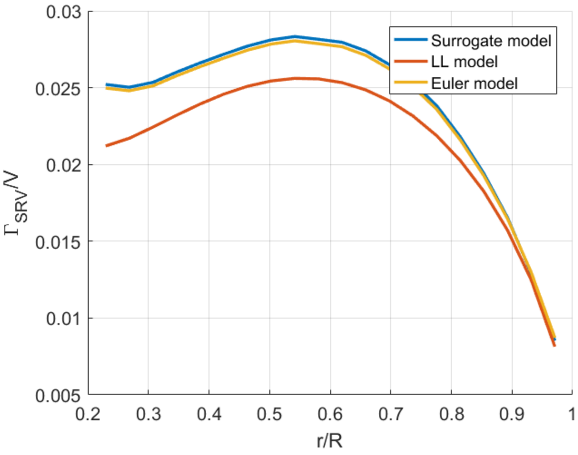

Figure 5.8: Comparison of optimum SRV circulation from LL model, Surrogate model and Euler model.

WING EFFECTS ON SRV PERFORMANCE

In this section, the low-fidelity result is utilized for understanding the wing effects on SRV as discussed in Sec. 2.3.2. For this purpose the optimum SRV is utilized where comparison is made of the results simulated with and without presence of wing under the same propeller slipstream, the corresponding cases are denoted as wing on and wing off respectively. For the problem at issue, it was thought that wing would induce an upwash at its upstream, resulting in enhancement of swirl at the UBS. This is confirmed by the panel results as depicted in Fig. 5.10. Moreover, it's further observed from Fig. 5.9 that the presence of wing also lead to a decrease of axial velocity, which is caused by wing thickness effect, and an overall effect is an increase of swirl angle over the entire blade span. This will cause a significant increase of SRV loading as depicted in Fig. 5.12, SRV produces 68.5% of extra lift and almost doubled. In total a lift that equals to 2.7% of system lift is obtained, and the thrust is equivalent to 14.8% reduction of wing induced drag. The conclusion can be drawn that the vane installed at UBS of wing upstream position experiences a considerable performance improvement due to wing induced velocity, thereby the design of SRV for wing-mounted tractor propeller should take wing induced velocity into account.

Table 5.3: Comparison of SRV performance with and without wing

Geometry	condition	C_L	C_T
SRV	wing off	0.00798	0.00031
	wing on	0.01345	0.00098

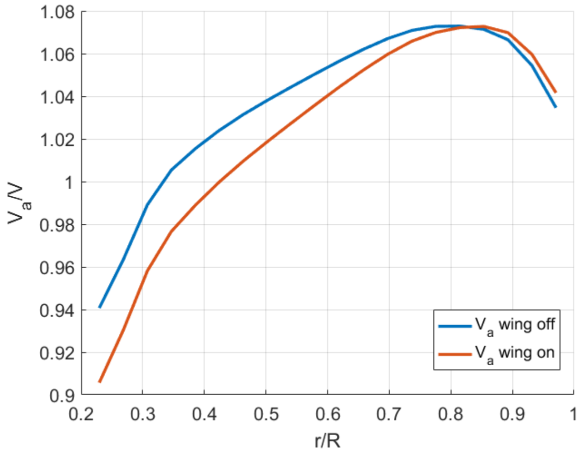

Figure 5.9: Comparison of axial velocity at SRV position with and without wing

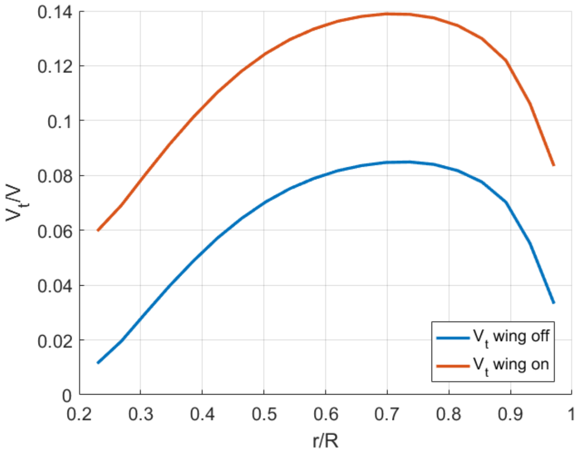

Figure 5.10: Comparison of tangential velocity at SRV position with and without wing

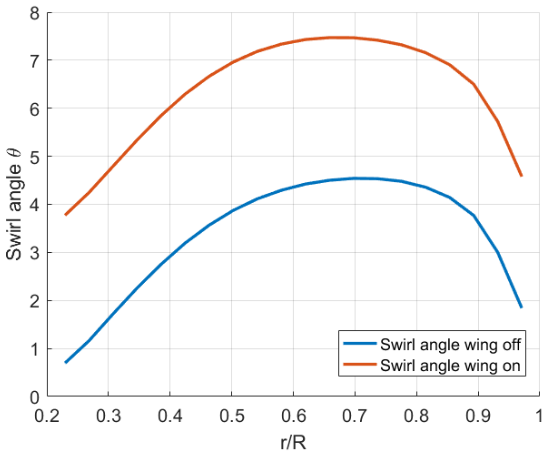

Figure 5.11: Comparison of swirl angle at SRV position with and without wing

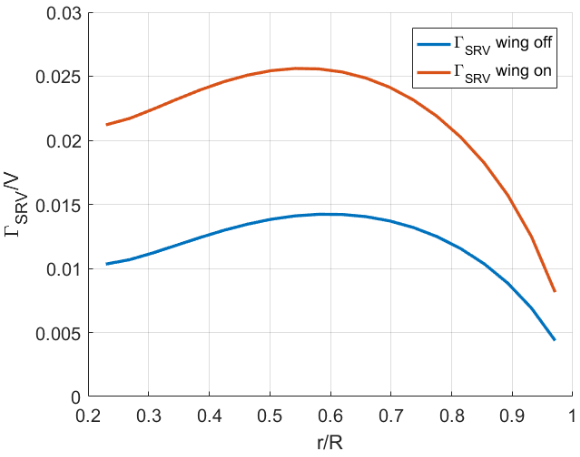

Figure 5.12: Comparison of optimum SRV circulation distribution with and without wing

SRV EFFECTS ON WING PERFORMANCE

Recapture that current discussion mainly focus on how SRV lead to a significant increase of wing induced drag. As already discussed in Sec. 3.2.3, wing induced drag can be decomposed of a few terms, including induced drag due to wing induced velocity $V_{wing,i}$, propeller induced velocity $V_{prop,i}$ and SRV induce velocity $V_{SRV,i}$. In order to distinguish which resources mainly contribute to wing induced drag increase, these terms are separately compared with and without installation of SRV, the results are presented in Table 5.4.

Table 5.4: Comparison of wing performance with and without SRV

Geometry	condition	C_L	$C_{Di,total}$	$C_{Di,wing}$	$C_{Di,prop}$	$C_{Di,SRV}$
Wing	SRV off	0.5	0.006607	0.007249	-0.00064	-
	SRV on	0.4863	0.008612	0.008295	-0.00038	0.00070

Result from the table indicates that with installed SRV the wing C_L reduces from $C_L = 0.5$ to $C_L = 0.4863$. This is caused by lift constraint during optimization where extra lift produced by SRV leads to equivalent amount of wing lift reduction. As is expected the reduction of wing lift should result in a wing induced drag decrease, however, it turned out the induced drag increased by 30.7%. By comparison of de-composed induced drag terms, it's found 1/6 of induced drag increase results from reduction of negative $C_{Di,prop}$, 1/3 of which comes from increase of $C_{Di,SRV}$, whereas 1/2 is caused by increase of $C_{Di,wing}$. It seems the change of wing circulation distribution has a dominant effects on the drag increase. For understanding this effects, the wing Γ and C_l distribution are compared with and without the optimum SRV.

The wing Γ and C_l distribution with and without SRV from Euler simulation is depicted in Fig. 5.13 and 5.14, respectively. The corresponding panel results are also provided for comparison. It's observed the trend of lift change follows circulation deviation, thereby only later term will be investigated. First, the Γ increase at outboard region is caused by increase of geometric angle of attack due to the lift constraint. Recapture that the SRV is located at UBS, as already explained it will causes a swirl reduction in slipstream such that the wing experiences a lower angle of attack and a corresponding smaller wing loading. This trend is observed for results from both Euler and Panel method. However, difference is observed at inboard region where a considerable reduction of wing loading occurs for Euler simulation, whereas such effects is not present for panel results. This phenomenon can't be explained by SRV swirl recovery effects since no propeller swirl exists outside slipstream region, and based on panel results, SRV only induces quite small velocity at this region which only leads to slightly decreased wing loading. It seems there exists some unknown effects which can be modeled in Euler analysis but can't be captured by potential flow method. In this respect, the flow domain of Euler analysis has to be investigated.

It can be explained that the tip vortex roll up from the stator affects the flow domain at both inside and close to slipstream region, as a result the inboard region experiences a significant velocity change. Due to the fact that the LL model used in this study applies a fixed trailing vortex, thereby it couldn't model such effects. This further prove the necessity of using multi-fidelity analysis for prediction of a SRV-wing interaction effects, such that the low-fidelity analysis can be corrected by more accurate high-fidelity results.

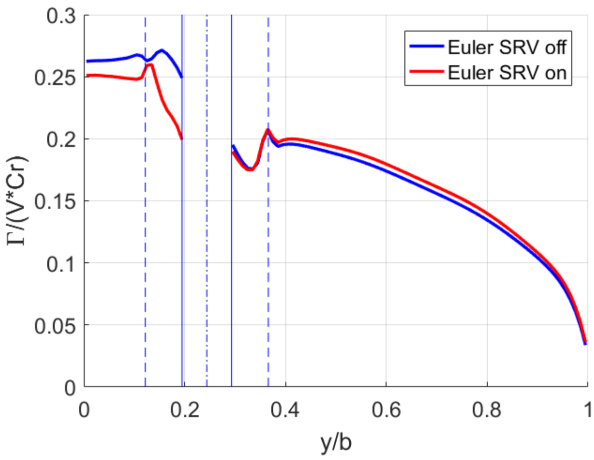

Figure 5.13: Comparison of wing circulation distribution with and without SRV from Euler simulation

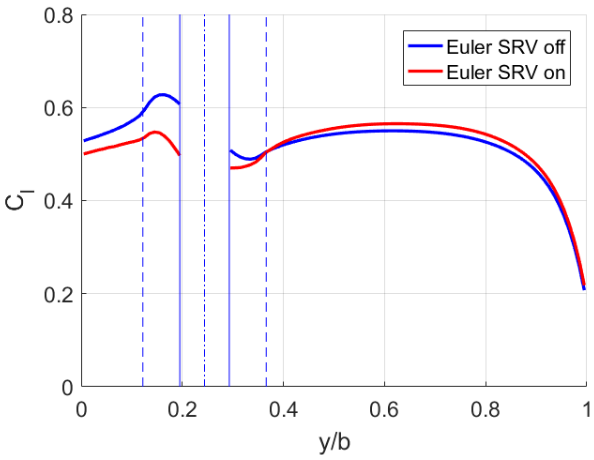

Figure 5.14: Comparison of wing lift distribution with and without SRV from Euler simulation

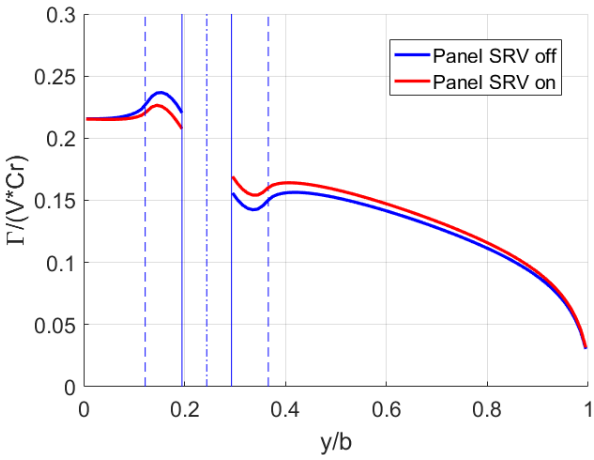

Figure 5.15: Comparison of wing circulation distribution with and without SRV from Panel result

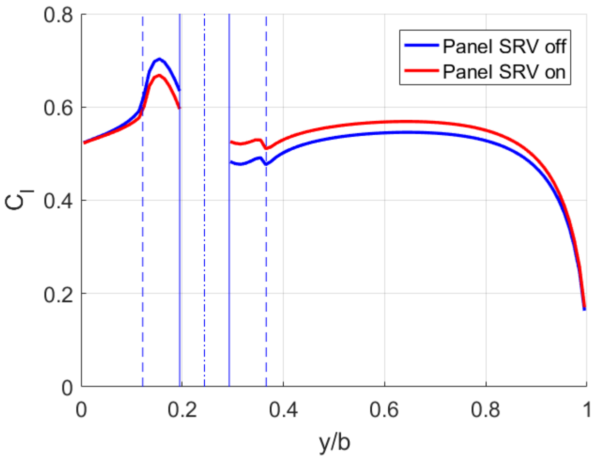

Figure 5.16: Comparison of wing lift distribution with and without SRV from Panel result

Based on the corrected Γ distribution, the change of the decomposed induced drag term caused by installed SRV can be explained. As is discussed in Sec. 3.2.3, the induced drag change is a combined effects of induced velocity and circulation change. Bare this in mind, first look at the change of $C_{di,prop}$ at Fig. 5.18, it can be seen that with reduced Γ at UBS and non-changed $V_{prop,i}$, the resulted $C_{di,prop}$ decreases at UBS. As a consequence the negative drag is reduced. In the same figure, Since $V_{SRV,i}$ is contrary to $V_{prop,i}$ within slipstream, it will lead to an induced drag which is opposite to that of propeller. Thereby, a positive $C_{di,SRV}$ is obtained. As for the change of wing self induced drag $C_{di,wing}$, a significant increase occurs at inboard boundary of slipstream where a circulation pick exists at the same position as depicted in Fig. 5.13. Based on lifting line theory, an increase of local boundary circulation will shed a clockwise trailing vortex, and a gradient decrease will lead to a counter-clockwise trailing vortex. This will induce a augmented downwash at the maximum circulation point, leading to a large induced drag at the plane. This mainly contribute to wing induced drag increase. Another explanation is that the vortex sheet is distorted by SRV especially at the tip vortex region, which could potentially lead to a local high downwash and induced drag pick. This effects can't be modeled by panel method due to the fixed wake assumption, but it could be captured by Euler analysis. This further explains the difference between of circulation distributions from both methods. As a conclusion, the tip vortex roll up of the stator causes a significant wing induced drag increase. In this respect, it's less interesting to install SRV in front of wing, and further investigation will focus on a wing downstream mounted

SRV.

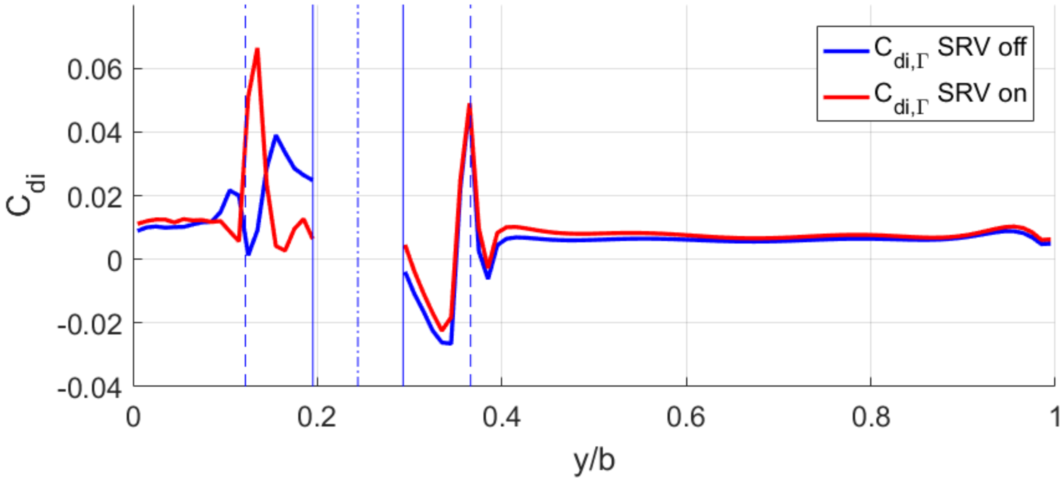

Figure 5.17: Comparison of $C_{di,\Gamma}$ of baseline wing and optimized wing

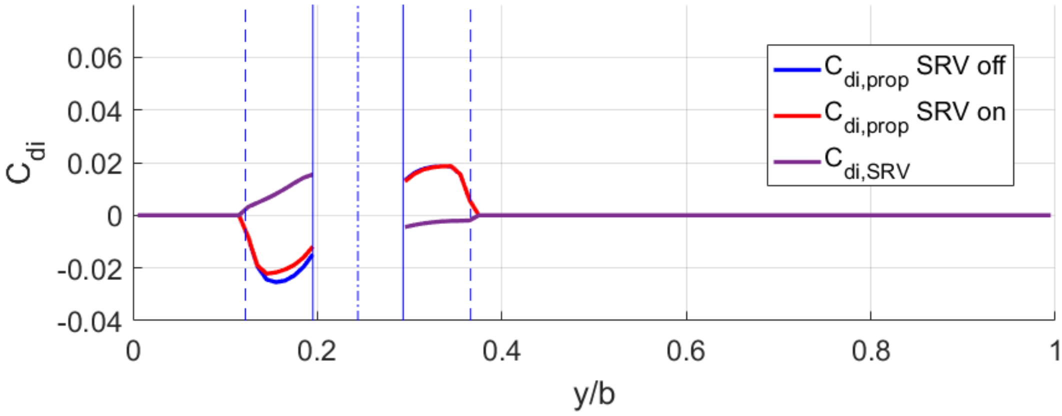

Figure 5.18: Comparison of $C_{di,prop}$ and $C_{di,SRV}$ of baseline wing and optimized wing

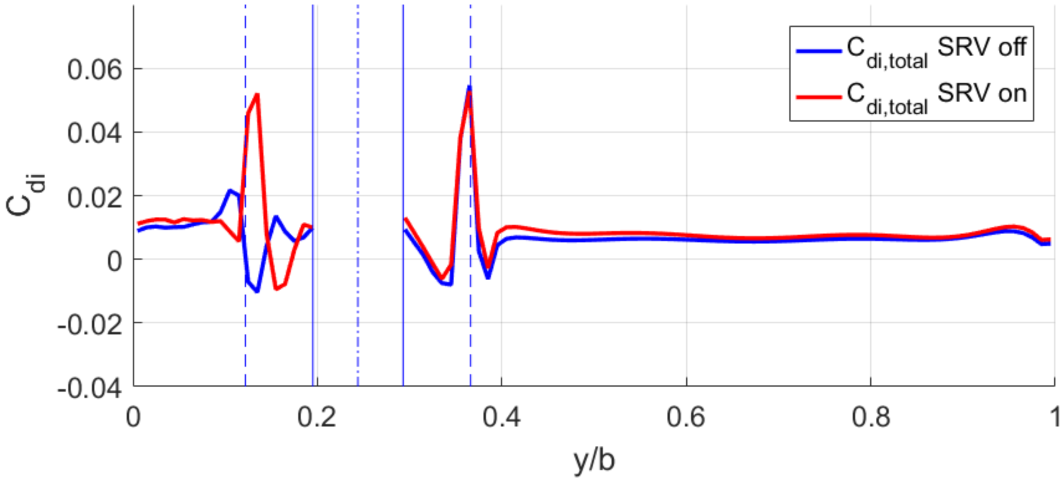

Figure 5.19: Comparison of $C_{di,total}$ of baseline wing and optimized wing

5.4.2. CASE 3&4: SRV DESIGN AT A WING DOWNSTREAM PLANE

When SRV is installed at wing downstream position, the negative effects of wing induced drag increase caused by tip vortex roll up of an upstream-installed vane could be avoided. However, due to the lift constraint, a DBS installed SRV would generate a negative lift, which requires a higher lift be generated on wing, such that a wing induced drag increase would potentially occur. The SRV will be design at both sides to fully survey the plane. The results are presented in Fig. 5.20 below.

DESIGN SPACE EXPLORATION

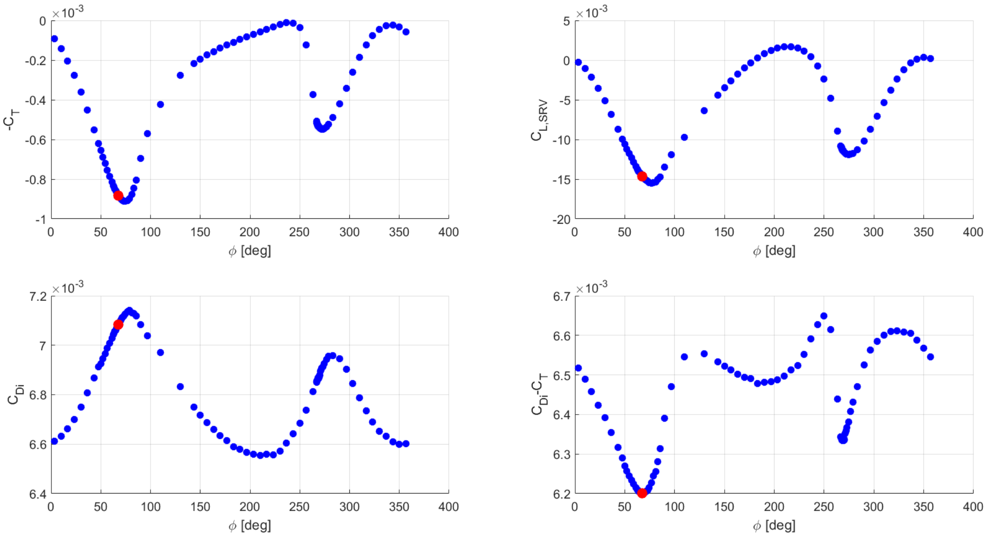

Figure 5.20: SRV and wing performance with respect to different SRV azimuthal positions

When looking at the down-going blade side, which is from 0 to π, a unique maximum vane loading location is found at around 75° where a maximum swirl is presented. The vane produced lift features the same trend as thrust variation, and it's always a negative value since it experiences a large downwash that induced by propeller and wing. As a result of negative lift produced by vane, the wing lift is reduced to obtain a constant overall lift of the system, thereby the wing induced drag is also augmented. To minimize $C_{Di} - C_T$, a compromise is reached between the increase of both vane thrust and wing induced drag. It's also noted that during optimization the vane thrust deviation $|\Delta C_T|$ is about 1.6 times of wing induced drag deviation $|\Delta C_{Di}|$, which means the SRV produced thrust dominants the optimization process, and performance benefit is finally gained that SRV produced thrust is larger than the wing induced drag increase. As for the optimization results of vane at UBS, the trend for performance deviation of both components is similar to the results of DBS. This indicates that wing induced downwash is larger than propeller induced swirl such that totally a downwash is presented in this region. The resulted thrust deviation almost equals to wing induced drag change throughout the design space. As a result, no significant performance gain is obtained since SRV produced thrust is always counteracted by wing induced drag increase. In this respect, it's less interesting to introduce vane design in this region. At the next step, the results of optimum SRV design at 75° (Case 4) will be presented and discussed.

OVERALL PERFORMANCE GAIN BY SRV DESIGN

In order to see the system performance gain by introduction of optimum SRV, comparison is made of wing performance with and without SRV, the result is presented in Table 5.5. It's observed that wing lift increased by 2.94%, which is equal to the magnitude of negative lift produced by SRV. As a result of lift increase, the wing induced drag increased by 7.23%. The wing L/Di is almost constant at around 75.65, in this respect the installed vane doesn't deteriorate wing performance. It produces a negative C_L of -0.0146 and the thrust is equivalent to 8.8 drag counts. An equivalent lift to thrust ratio L/T can be defined for SRV, which is calculated to be 16.6, and this value is significantly lower than wing. It's noted that, as is different from wing, a lower value of vane lift to thrust ratio is good for system. This is because for the same amount of lift production, the higher thrust the higher drag reduction. Thereby the lift is allocated as mush as possible to the vane to obtain a higher thrust, thereby a lower system induced drag. As an overall effects, the system induced drag decreased by 6.08%, which is almost equal to induced drag reduction by wing twist optimization. It should be noted that only a one-blade SRV is introduced and the performance benefits is already as good as wing optimization, it's expected that with the increase of vane number, the performance gain can be potentially higher.

Table 5.5: Comparison of performance of initial design (baseline wing only) and optimum design (baseline wing with optimum SRV)

	Configuration	C_L	C_{Di}	C_T	$-C_T + C_{Di}$	$\Delta(-C_T + C_{Di})$	$\Delta(-C_T + C_{Di})[\%]$
Baseline	Wing	0.5	0.006607	-	0.006607	-	-
Optimum	Wing	0.5147	0.007085	-	0.006205	-0.000402	-6.08%
	SRV	-0.01467	-	0.00088			

OPTIMUM SRV DESIGN

It can be recognized that the vane finally converged to the position where a highest swirl is presented, which supports the conclusion that optimum vane features the highest loading in design space as already discussed in 5.4.2. The optimum vane loading is similar to the result of Case 1 5.8 since the SRV C_T is almost equal at both cases. The comparison of inflow velocity and swirl angle will be presented for supporting this results.

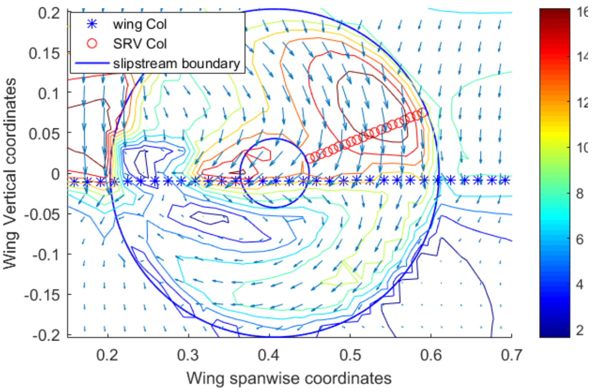

Figure 5.21: Optimum SRV azimuthal position

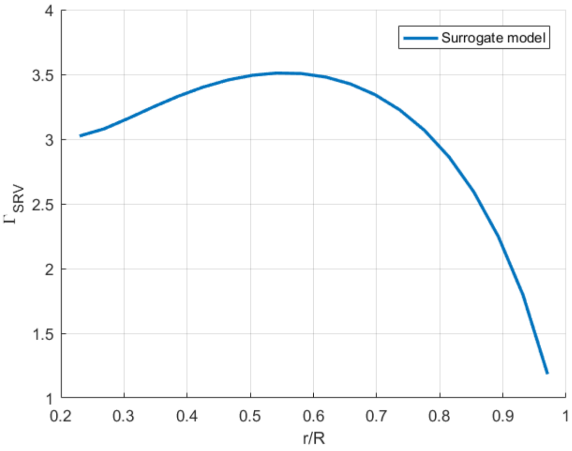

Figure 5.22: Optimum SRV circulation obtained from Surrogate model

WING EFFECTS ON SRV PERFORMANCE

In this subsection the wing effects on SRV performance is discussed. As is similar to the investigation at 5.4.1, the low-fidelity result is utilized for this purpose, where potential flow analysis is performed on the optimum SRV with and without wing installed, and the results are compared in Table 5.6. As can be seen from the table, the isolated SRV already features a negative lift and positive thrust due to propeller induced downwash. With the installation of wing, the magnitude of negative lift increased by 83% and the thrust experiences a more considerable increase of 2.3 times. This can be explained by the velocity and swirl angel profile at the vane position. Observe Fig. 5.23, the axial velocity only slightly changed when the wing is installed, which is because the thickness effects is small due to the thin airfoil section at trailing edge. For tangential velocity as presented in Fig. 5.24, it is considerably enhanced due to wing induced downwash. The overall effect is a considerable increase of swirl angle along the entire blade span, thereby the optimum circulation distribution is also reinforced.

Table 5.6: Comparison of SRV performance with and without wing

Geometry	condition	C_L	C_T
SRV	wing off	-0.00801	0.00027
	wing on	-0.01467	0.00088

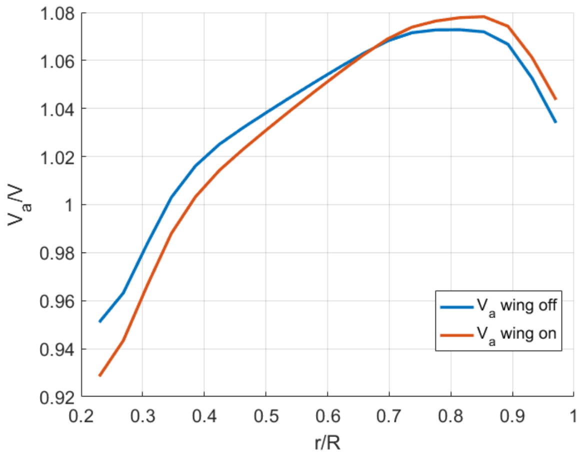

Figure 5.23: Comparison of axial velocity at SRV position with and without wing

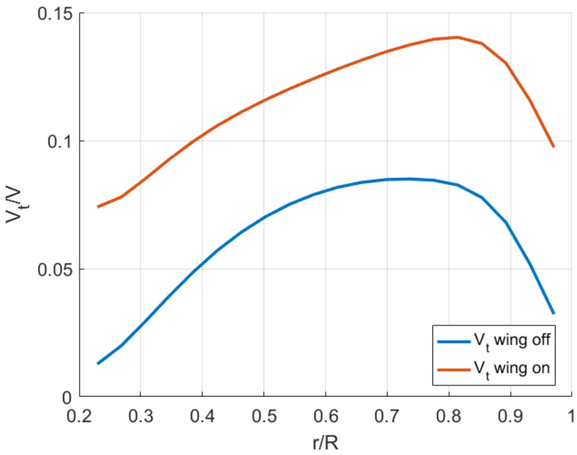

Figure 5.24: Comparison of swirl velocity at SRV position with and without wing

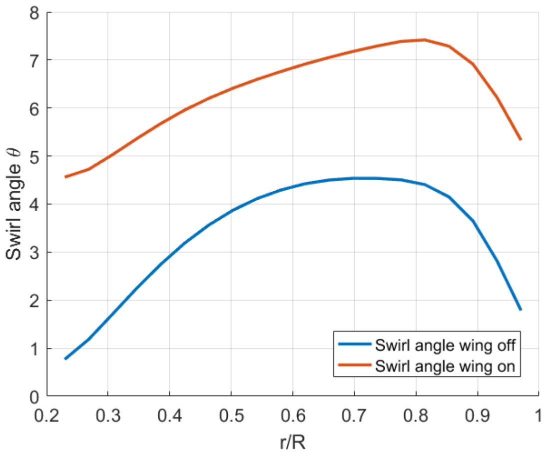

Figure 5.25: Comparison of swirl angle at SRV position with and without wing

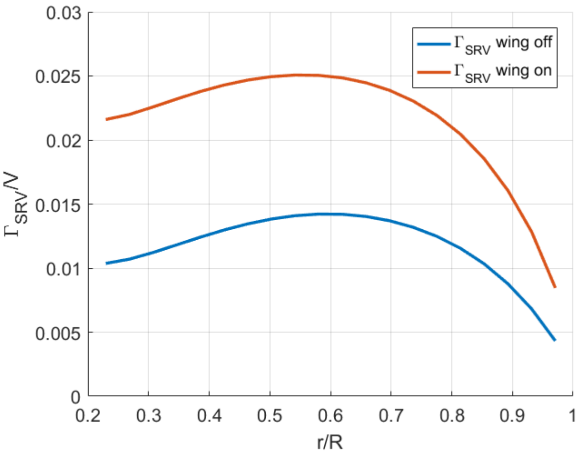

Figure 5.26: Comparison of optimum SRV circulation distribution with and without wing

SRV effects on Wing performance

This section the SRV effects on the performance of a wing at upstream position is investigated. As is already discussed, the SRV can be seen as a small lifting surface such that it has a negligible effects at a upstream component. This is supported in current low-fidelity analysis. It can be seen from Fig. 5.27 and 5.28 that, with installed SRV, both the Γ and C_l features an almost same pattern with only a slightly upward shift, which is due to the increased angle of attack resulted from the lift constraint. And from the comparison of wing induced drag distribution denoted in Fig. 5.29, it's observed the increase of wing induced drag is mainly at inboard and outboard region, whereas the slipstream regions experiences almost no changes. This indicates the SRV only has limited effects on the wing performance at outside slipstream part due to the lift constraint.

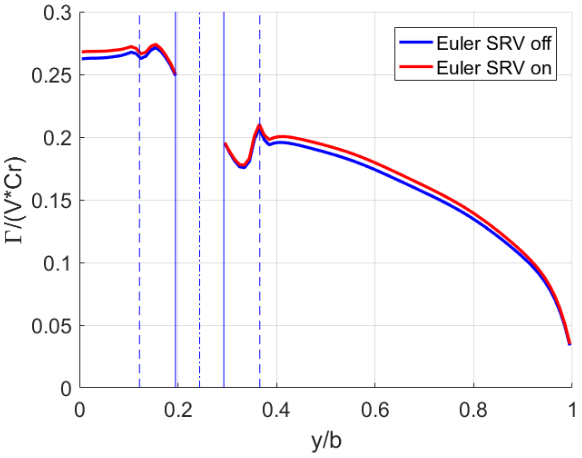

Figure 5.27: Comparison of wing circulation distribution with and without SRV from Euler simulation

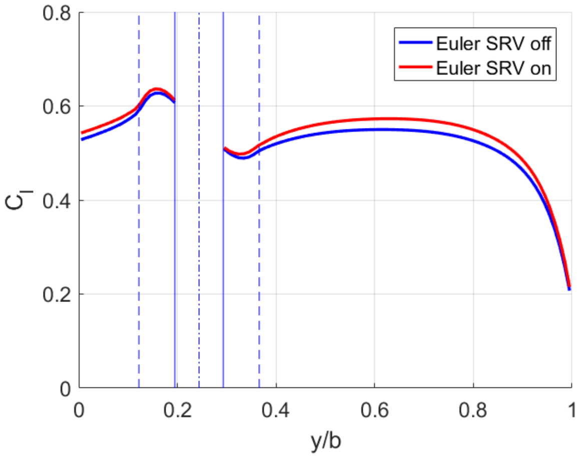

Figure 5.28: Comparison of wing lift distribution with and without SRV from Euler simulation

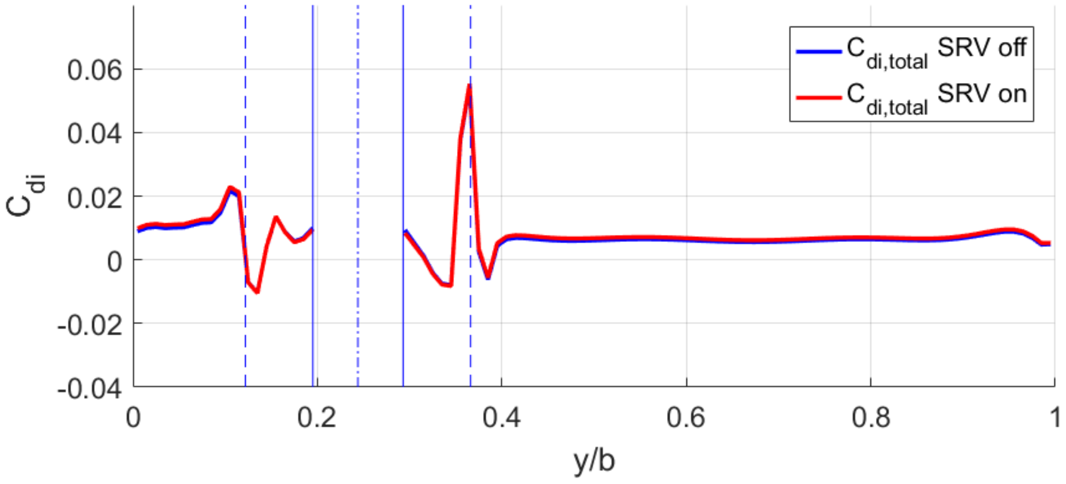

Figure 5.29: Comparison of wing induced drag distribution with and without SRV

5.4.3. CASE 5: SRV DESIGN AT A SERIES OF WING DOWNSTREAM PLANES

Conclusions can be drawn from the optimization results that the deviation of SRV and wing performance is highly related to their relative positions, and the DBS of tailing the wing is most preferable for SRV design. In order to fully explore the flow domain behind the wing, a serial of design cases are performed along different downstream positions at DBS behind the wing. At each position, a one-blade SRV is performed to find the optimum azimuthal positions. The objective is to find the optimum streamwise position for SRV design at this region. Finally the design providing maximum system performance will be further analyzed and discussed. Considering the computation burden, five streamwise positions were selected, the starting plane is located at downstream distance of $0.75 * c_r$ to wing quarter chord line. This position is selected as the extreme position that is feasible for SRV design, since a more upstream plane will coincide with the wing geometry. The rest planes are located along downstream with equal interval of $0.4 * R$. The last plane is located at $3 * R$, since results indicates no significant performance benefit can be obtained with a more downstream installed vane.

The results are provided in figures below.

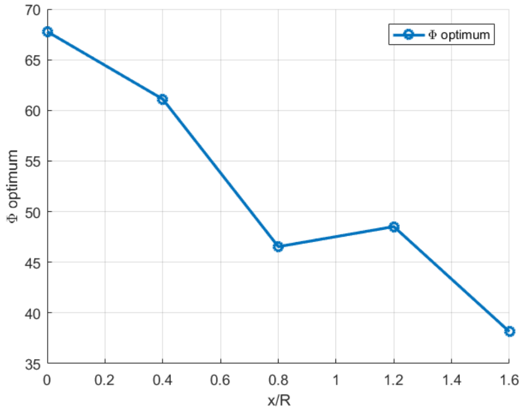

Figure 5.30: Optimum SRV azimuthal position with respect to streamwise position

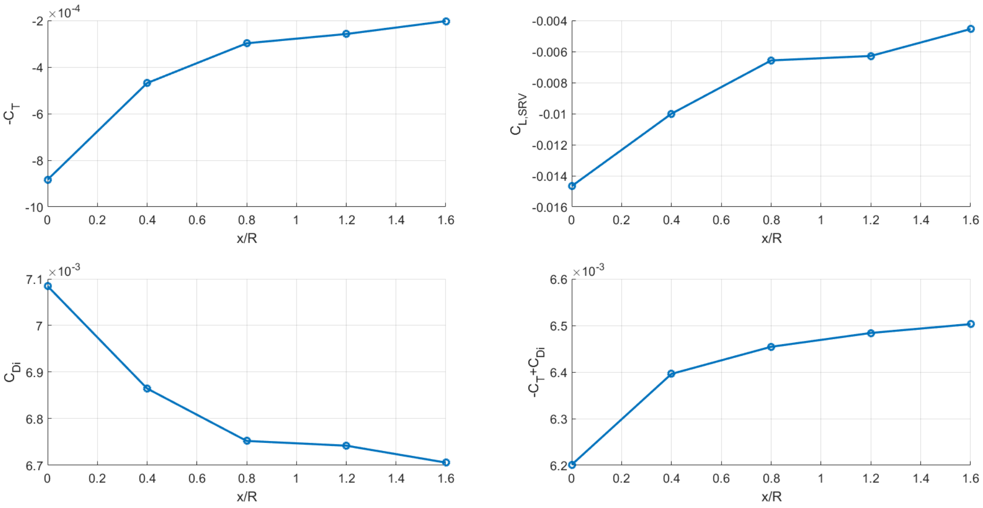

Figure 5.31: SRV and wing performance

It can be seen from Fig. 5.30 that the azimuthal position of optimum SRV decreases with increased downstream distance from starting plane, indicating that it will tilt more vertically when moving far from wing. This might due to the shift of the maximum swirl region. The SRV $C_{T,SRV}$ and $C_{L,SRV}$ also reduces, and the change is first rapid and then become more gradual. This does make sense as the loading of SRV is determined by the inflow velocity, due to wing induced velocity, a relatively high velocity gradient exists at wing vicinity, which becomes less significant when it moves far downstream. With the increase of SRV produced lift, the wing lift is reduced, as a result the wing induced drag is also decreased. When looking at the objective of $-C_T + C_{Di}$, a minimum value is found at he starting plane. This indicates that the SRV should be installed as close to wing trailing edge as possible to obtain an optimum system performance in terms of induced drag reduction.

6

CONCLUSIONS AND RECOMMENDATIONS

This chapter presents the conclusions drawn from all the content. This thesis is about design of SRV for a wing-mounted tractor propeller configuration. The objective is to investigate an optimum SRV design that provides a maximized system propulsive performance for a wing-mounted tractor propeller configuration. The optimum SRV design case is further compared with a wing design case for the same propeller slipstream to know which case has higher performance benefits. This study is realized by performing a serial of panel and Euler analysis, and a surrogate based multi-fidelity optimization routine is utilized to find the optimum design. This thesis work is based on previous work performed by Li et al. [6, 9], includes:

- A lifting-line based SRV design and analysis module for uniform inflow along circumference.
- Adaptation of SRV analysis and design module for non-uniform inflow along circumference.

Current work mainly involves the development of a series of analysis tools and also two optimization tasks. The conclusions are discussed correspondingly.

6.1. CONCLUSIONS ON THE ANALYSIS TOOL DEVELOPMENT

The analysis tools that developed in this study involves:

- Development of potential-based wing analysis module, including adaptation of wing lift and induced drag calculation for propeller and SRV induced velocity.
- Validation of wing analysis module by use of Euler simulation, including the validation of circulation distribution, lift distribution and wing induced velocity at SRV position.
- Modification of SRV analysi and design module for non-axisymmetric inflow condition.
- Development of Surrogate-based multi-fidelity optimization framework for wing and SRV design. The shape-preserving response prediction(SPRP) technique is utilized for correlating of low-fidelity results with a high-fidelity solution.

The corresponding conclusions for the analysis tool implementation mainly involves two discussion, including the validation study for the tool and the reasoning for using a SPRP based surrogate modeling technique.

- The results of implemented potential method matches well with the Euler simulation on a clean wing case, whereas a non-negligible difference is observed in terms of wing circulation and lift distribution for a propeller on case. Instead of using an iterative process to match both results, a shape-preserving-response-prediction(SPRP) process is applied for correction of circulation distribution from both methods. Results indicated that the SPRP surrogate managed to predict the Euler results of wing Γ and C_l on a propeller-wing configuration as well as a propeller-SRV-wing configuration.

- The wing induced velocity at SRV position obtained from potential methods matches well with that from Euler simulation on a propeller-wing configuration, which further prove the feasibility of coupling SRV LL model with wing Panel model for design and optimization purposes.

6.2. CONCLUSIONS ON THE OPTIMIZATION TASKS

Two optimization tasks are mainly performed to reach the research objective:

- Perform wing optimization for minimum induced drag in a wing-mounted tractor propeller arrangement.
- Perform SRV design for maximized integrated thrust-drag performance of a wing-mounted tractor propeller configuration.

The conclusion drawn from the optimization results are discussed here:

- As for results of wing twist optimization, by comparing of the initial design and the optimum design from final loop, the reduction of C_{Di} from the optimization is found to be 3.92 counts, corresponding to 5.93% of total induced drag of the baseline wing and 1.4% of propeller thrust. The optimized twist distribution features higher value at mid-part of wing and lower value at root and tip. Based on a quantitative analysis, the slipstream always feature a higher L/Di compared with the rest regions, in this respect the optimization tends to allocate the lift to region features higher L/Di such that the overall Di will be lower for the same amount of lift.

- As for SRV design in between propeller and wing, the wing performance is significantly deteriorated due to the upstream installed SRV, since a much higher induced drag is achieved with lower lift. In detail, even though SRV can produce a thrust which is equivalent to 9.8 drag reduction, at the same time it also causes a significant increase of wing induced drag by 20.3 drag counts, consequently an overall drag increase of 10.3 count is finally reached, equivalent to 15.5% of wing induced drag. From the decomposed induced drag calculation, a significant increase of wing circulation induced drag is observed. And Euler simulation shows the wing circulation distribution is distorted not only within slipstream but also at wing inboard region which is resulted from the vane tip vortex roll up, and this further leads to increase of wing circulation induced drag as observed. This further prove the necessity of using multi-fidelity analysis for analyzing such an interaction effects. To avoid this performance disadvantage, the SRV was designed at downstream of wing.

- As for SRV design at wing downstream, the optimum azimuthal position is observed at down-going blade side and the installed vane doesn't deteriorate wing performance at this time. However, due to the lift constraint and the negative lift produced by vane, the lift of wing also increases such that it also causes a wing induced drag increase. The optimum SRV produces a negative C_L of -0.0146 and the C_T is equivalent to 8.8 drag counts. An equivalent lift to thrust ratio(L/T) can be defined for SRV, which is calculated to be 16.6, and this value is significantly lower than wing 75.8. It's noted that, as is different from wing, a lower value of vane lift to thrust ratio is good for system. This is because for the same amount of lift production, the higher thrust means higher drag reduction. Thereby, the lift of the system is allocated as much as possible to the vane to obtain a lowest system induced drag. As an overall effects, the system induced drag decreased by 6.08%, which is almost equal to induced drag reduction by wing twist optimization(5.93%). It should be noted that only a one-blade SRV is introduced and the performance benefits is already as good as wing optimization, it's expected that with the increase of vane number, the performance gain can be potentially higher.

6.3. RECOMMENDATIONS

- As for the development of low-fidelity analysis tool, the implemented Trefftz Plane Analysis(TPA) method for wing induced drag calculation is only validated by use of a clean wing case, while the validation of adaptated TPA for propeller and SRV effects is not possible due to the lack of numerical and experimental data. This study choose to calculate the induced drag distribution by use of line integral, while further study can utilize surface integral form of induced drag calculation. The validation of adapted TPA for propeller and SRV effects should be performed.

- As for the optimization cases in this study, only a one-blade SRV is designed for each case. Further study can investigate the effects of blade number count on the system performances

- This study was performed in the potential flow field while neglecting the viscous effects in the system. It can be expected that by considering the viscous effects, for example the flow separation and boundary layer interaction, the SRV and wing performance could be potentially deviated and the conclusion drawn in this study may be changed.

A

Code Architecture

This chapter mainly introduce the architecture of the code that developed in current study. This code is implemented in Matlab scripts. As can be seen in Fig.A.1, $Direct_SRVdesign()$ is the main function, where all the inputs and settings can be manually modified by users. The $slipstream()$ function incorporates the slipstream model that contains the velocities(excel file) obtained from RANS simulation. The $WingCL0()$ function initializes the baseline wing design based on the input, and the SPRP surrogate is generated (and also updated later on) here by correlating the panel result with the Euler simulation. Then the optimization can be run by calling $Direct()$ function. The $SRVWingresult()$ is the objective function, where $SRV_analysis()$ and $WingInducedDrag()$ functions are called to perform the low-fidelity analysis routine. $SRV_analysis()$ is responsible for performing SRV design and analysis under propeller and wing induced velocity field, thus the $Wing_analysis()$ is also called here to iteratively reach the convergence of induced velocity. Finally, the $WingInducedDrag()$ function is called to perform Trefftz Plane Analysis for wing induced drag calculation under propeller and SRV effects. It should be noted that this framework only contains one loop of surrogate optimization. The updating of surrogate model is achieved by manually change the excel file contains the Euler simulation results.

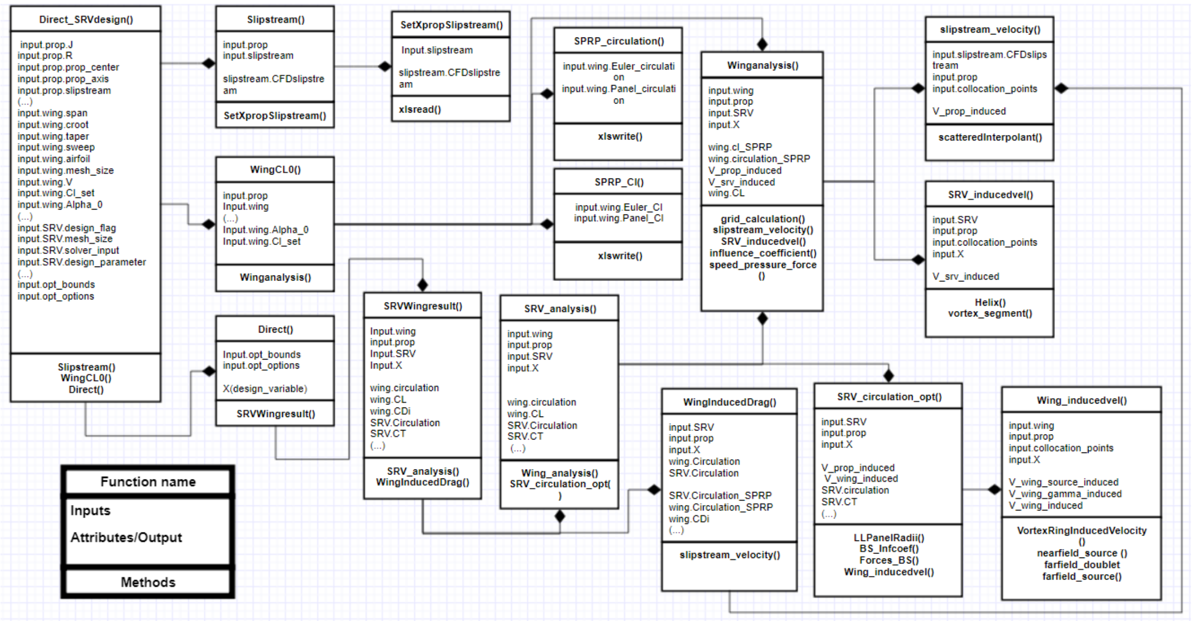

Figure A.1: Architecture of the code for SRV and wing design

BIBLIOGRAPHY

[1] R. D. Hager and D. Vrabel, *Advanced Turboprop Project*, Tech. Rep. (National Aeronautics and Space Administration, 1988).

[2] B. M. D. and D. V. P., *The advanced turboprop project: Radical innovation in a conservative environment,* (2014).

[3] T. Sinnige, J. J. A. van Kuijk, K. P. Lynch, and L. V. Daniele Ragni, Georg Eitelberg, *The effects of swirl recovery vanes on single-rotation propeller aerodynamics and aeroacoustics,* 21st AIAA/CEAS Aeroacoustics Conference (2015).

[4] V. L. L. M., *Propeller wing aerodynamic interference,* PHD thesis (2005).

[5] T. C. A. Stokkermans, *Design and analysis of swirl recovery vanes for an isolated and a wing mounted tractor propeller,* Master thesis (2015).

[6] Q. Li, K. Öztürk, T. Sinnige, D. Ragni, G. Eitelberg, L. Veldhuis, and Y. Wang, *Design and experimental validation of swirl recovery vanes for propeller propulsion systems,* AIAA (2017).

[7] D. WITKOWSKI, R. JOHNSTON, and J. SULLIVAN, *Propeller/wing interaction,* 27th Aerospace Sciences Meeting (1989), 10.2514/6.1989-535.

[8] M. F. Niţă, *Aircraft design studies based on the atr 72,* Master Thesis (2008).

[9] G. E. Qingxi Li, Xinyuan Liu and L. Veldhuis, *Numerical investigation of configuration with optimum swirl recovery for propeller propulsion systems,* AIAA (2018).

[10] B. P. Epps and R. W. Kimball, *Unified rotor lifting line theory,* Journal of Ship Research (2013).

[11] J. KATZ and A. PLOTKIN, *Low-Speed Aerodynamics.*

[12] S. Koziel and L. Leifsson, *Airfoil shape optimization using variable- fidelity modeling and shape-preserving response prediction,* (2011).

[13] D. E. Finkel, *Direct optimization algorithm user guide,* (2003).

[14] C. Alba, *A surrogate-based multi-disciplinary design optimization framework exploiting wing- propeller interaction,* Master thesis (2017).

[15] S. W. C., K. G., W. A. L., G. J., and B. E., *Technology and benefits of aircraft counter rotation propellers,* NASA-TM-82983 (1981).

[16] E. W. M. Roosenboom, *Experimental and numerical investigation of a counter rotating open rotor flow field,* 29th AIAA Applied Aerodynamics Conference (2011).

[17] G. J. and R. G., *Wind tunnel performance results of swirl recovery vanes as tested with an advanced high speed propeller,* 28th Joint Propulsion Conference and Exhibit (1992).

[18] M. C. J., *Euler analysis of a swirl recovery vane design for use with an advanced single-rotation propfan,* 24th Joint Propulsion Conference and Exhibit (1988).

[19] Y. O., *Numerical calculation of propfan/swirl recovery vane flow field,* 28th Joint Propulsion Conference Exhibit (1992).

[20] W. Y., L. Q., E. G., V. L. L. M., and K. M., *Design and numerical investigation of swirl recovery vanes for the fokker 29 propeller,* Chinese Journal of Aeronautics **27**, 1128 (2014).

[21] K. I., *Propeller-wing integration for minimum induced loss,* Journal of Aircraft **23**, 561 (1986).

[22] H. Epema, *Wing optimisation for tractor propeller configurations,* Master thesis (2017).

[23] L. Veldhuis, T. Stokkermans, T. Sinnige, and G. Eitelberg, *Analysis of swirl recovery vanes for increased propulsive efficiency in tractor propeller aircraft,* ICAS (2016).

[24] J. Cho and J. Cho, *Quasi-steady aerodynamic analysis of propeller-wing interaction,* International Journal For Numerical Methods In Fluids (1999).

[25] Q. R.Wald, *The aerodynamics of propellers,* Progress in Aerospace Sciences 42, 85 (2006).

[26] L. Q. and W. Y. E. G., *An investigation of tip vortices unsteady interaction for fokker 29 propeller with swirl recovery vane,* Chinese Journal of Aeronautics , 1000 (2015).

[27] *N250 propeller Shoptest*, Tech. Rep. (Nationaal Lucht en Ruimtevaartlaboratorium, 1993).

[28] *U.s. standard atmosphere,* (2003).

[29] M. D. Patterson and B. J. German, *Wing aerodynamic analysis incorporating one-way interaction with distributed propellers, 14th AIAA Aviation Technology, Integration, and Operations Conference,* , 2852 (2014).

[30] F. Kohlsmied, *Analysis of propeller-wing interference by means of a second order panel method,* Master thesis (1996).

[31] B. Smith, *The flow over a wing/nacelle combination in the presence of a propeller slipstream,* First Canadian symposium on Aerodynamics (1989).

[32] M. Drela, *An analysis and design system for low reynolds number airfoils,* Low Reynolds number aerodynamics (1989).

[33] H. Hoeijmakers, *Panel methods for aerodynamic analysis and design,* (1991).

[34] G. v. Es, *Evaluation of the pdaero panel method with correct wing thickness to model the flow of propeller-wing-nacelle combinations,* Fokker Report A-273 (1994).

[35] W. Beek, C.M. van; Piers and B. Oskam, *Aerodynamic analysis of slipstream/wing/nacelle interference for preliminary design of aircraft configurations,* AGARD CP-498 (1991).

[36] D. F. Dipl., *Apame - aircraft 3d panel method,* (2008).

[37] S. C. Smith, *A Computational and Experimental Study of Nonlinear Aspects of Induced Drag*, Tech. Rep. (Ames Research Center, 1996).

[38] J. James A. Blackwell, *Numerical method to calculate the induced drag or optimum loading for arbitrary non-planar aircraft,* NASA Technical Reports (1976).

[39] M. S. M. D.L. Whitfield, Mississippi State Univ. and P. N. A. Jameson, Princeton Univ., *Three-dimensional euler equation simulation of propeller-wing interaction in transonic flow,* AIAA 21st Aerospace Sciences Meeting (1983).

[40] J. Holland, *Adaptation in natural and artificial systems.* University of Michigan Press (1975).

[41] E. R. S. Y. Kennedy, J., *Swarm intelligence.* (2001).

[42] M. Dorigo, *Optimization, learning and natural algorithms,* Phd Thesis (1992).

[43] L. Leifsson and S. Koziel, *Multi-fidelity design optimization of transonic airfoils using physics-based surrogate modeling and shape-preserving response prediction,* (2010).

[44] Z. J. X. X. He, Y.Y., *Comparison of different chaotic maps in particle swarm optimization algorithm for long term cascaded hydroelectric system scheduling,* Chaos, Solitons and Fractals 42(5) (2009).

[45] S. Koziel, *Efficient optimization of microwave circuits using shape-preserving response prediction,* IEEE TRANSACTIONS ON MICROWAVE THEORY AND TECHNIQUES (2009).

[46] S. Koziel, *Shape-preserving response prediction for microwave design optimization,* IEEE TRANSACTIONS ON MICROWAVE THEORY AND TECHNIQUES (2010).

[47] C. D. I. R. D. R. JONES and B. E. STUCKMAN, *Lipschitzian optimization without the lipschitz constant,* (1993).

[48] C. B. B. G. W. M. S.E. Cox, R.T. Hafka and L. Watson, *Global optimization of a highh speed civil transport configuration,* 3rd World Congress of Structural and Multidisciplinary Optimization (1999).

[49] H. Zhu and D. B. Bogy, *Direct algorithm and its application to slider air-bearing surface optimization,* IEEE TRANSACTIONS ON MAGNETICS (2002).

[50] L. T. Watson and J. He, *The deterministic global optimization algorithm direct,* HPCS/BIS Tutorial (2008).

[51] D. E. Finkel, *Direct - a global optimization algorithm,* (2004).

[52] I. Samuelsson, *Low speed wind tunnel investigation of propeller slipstream aerodynamic effects on different nacelle-wing combinations, ICAS, Congress, 16 th, Jerusalem, Israel,* , 1749 (1988).